MARIA S. MERIAN-BERICHTE

LITHOS-iLAB – Structure and Evolution of the Oceanic Lithosphere

Cruise No. MSM69

14.11.2017 – 22.12.2017
Mindelo/Praia (Cape Verdes) – Mindelo (Cape Verdes)

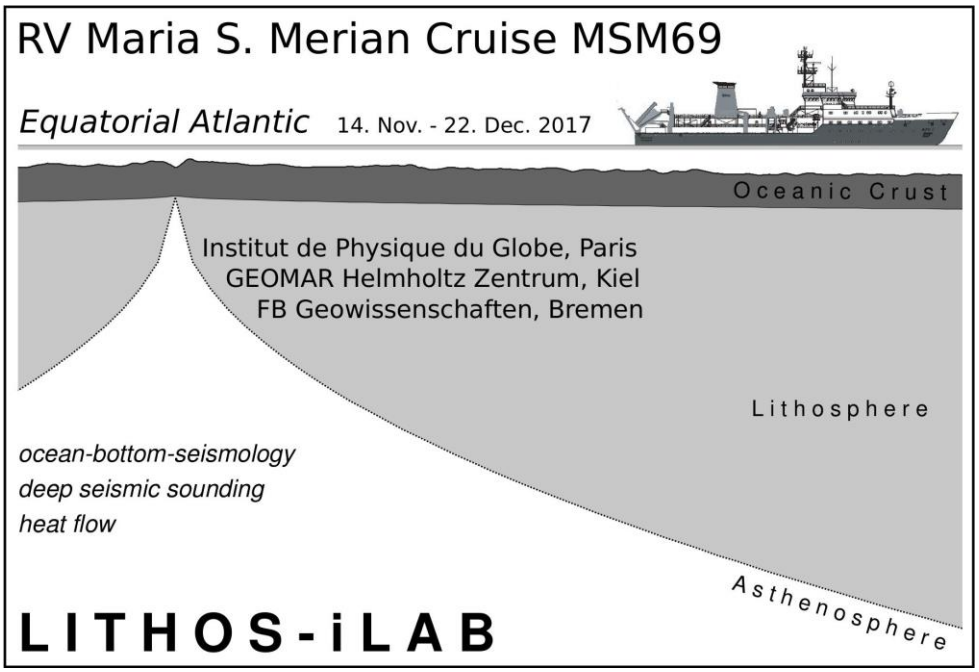

Ingo Grevemeyer, Satish Singh, Heinrich Villinger,
Cord Papenberg, and Norbert Kaul (Editors)

Editorial Assistance:

Senatskommission für Ozeanographie der Deutschen Forschungsgemeinschaft
MARUM – Zentrum für Marine Umweltwissenschaften der Universität Bremen

Leitstelle Deutsche Forschungsschiffe
Institut für Meereskunde der Universität Hamburg

2018

Table of Contents

1 Summary

The oceanic lithosphere is created by seafloor spreading at mid-ocean ridges and covers approximately 57% of the Earth surface. Properties of the oceanic crust – like its thickness and lower crustal velocity – are inherently related to the formation of the plate and can be used to infer periodicities in crustal accretion when moving away from the spreading ridge. After its formation the shallow lithosphere or crust is affected by hydrothermal circulation in the uppermost permeable crust over tens of millions of years. In turn, heat is removed from the lithosphere by circulating seawater and mineral precipitation modifies and seals open void spaces, affecting the heat loss, seismic velocity, and composition of the crust. In addition, the lithosphere cools and thickens with age, resulting in the well-known subsidence of the seabed, decreasing heat flow, geoid height, and increasing seismic velocities in the uppermost mantle. While the formation of crust and lithosphere at the spreading ridges is reasonably well studied, little is known about how crustal accretion changed over time and how crust and lithosphere change when being carried away from the underlying heat source. Understanding how lithosphere evolves with age is thus a major challenge in Earth sciences. In the equatorial Atlantic, MSM69 provided seismic data from an 1100 km long transect, call P01, surveying age-dependent features of the lithosphere, revealing crustal structure and mantle properties, including major lithospheric boundaries like Moho and decaying heat flow.

Zusammenfassung

Entlang der mittelozeanischen Rücken wird kontinuierlich neue ozeanische Lithosphäre generiert und bedeckt ca. 57% der Erdoberfläche. Die Krustenmächtigkeit und die Schallgeschwindigkeit in der Unterkruste werden durch die Schmelzgenerierung an der Rückenachse kontrolliert und bilden somit über die Zeit Änderungen im Spreizungsprozess ab. Nach ihrer Bildung führen über Millionen von Jahren hydrothermale Prozesse zu profunden Äderungen in der Struktur der Lithosphäre. Die Zirkulation von Seewasser durch die Kruste führt große Wärmemengen ab und die Ausfällungen hydrothermaler Alterationsprodukte verschließen Hohlräume und erhöhen somit die Schallgeschwindigkeit in der Oberkruste. Darüber hinaus kühlt die Lithosphäre mit dem Alter ab. Als Konsequenz der Abkühlung verdickt und verdichtet sich die Lithosphäre. Diese Änderungen spiegeln sich in der Zunahme der Wassertiefe, der Abnahme des Wärmestroms und des Geoids sowie in einer Erhöhung der seismischen Geschwindigkeit im Mantel wieder. Während die Bildungsprozesse der Lithosphäre an den Rückenachsen relativ gut untersucht sind, wissen wir nur wenig darüber, wie sich der Spreizungsprozess mit der Zeit verändert hat und welchen Einfluss altersbedingte Änderungen auf die Struktur und Eigenschaften der Lithosphäre haben. Während der Expedition MSM69 wurde im äquatorialen Atlantik südlich des Äquators ein 1100 km langer Korridor seismisch und geothermisch Untersucht, um altersabhängige Änderungen in der Krustenstruktur, die Lage bedeutender Manteldiskontinuitäten wie Moho, sowie die thermische Struktur der Lithosphäre zu untersuchen.

2 Participants

Name	Discipline	Institution
1. Ingo Grevemeyer, chief scientist	OBS	GEOMAR
2. Cord Papenberg, scientist	OBS	GEOMAR
3. Laura Gómez de la Peña, scientist	OBS	GEOMAR
4. Klaus-Peter Steffen, technicain	Airguns	GEOMAR
5. Patrick Schröder, technicain	OBS / Airguns	GEOMAR
6. Henning Schröder, scientist	OBS / Airguns	GEOMAR
7. David Lemke, student	OBS	CAU / GEOMAR
8. Kevin Growe, student	OBS	CAU / GEOMAR
9. Alexander Jüstel, student	OBS	GEOMAR
10. Lina Heine, student	OBS	CAU / GEOMAR
11. Heinrich Villinger, scientist, co-PI	Heat Flow	GeoB
12. Norbert Kaul, scientist	Heat Flow	GeoB
13. Alexander Weise, student	Heat dlow	GeoB
14. Jan-Niklas Schmidt, student	Heat Flow	GeoB
15. Satish Singh, scientist, co-PI	Seismics	IPGP
16. Pierre Guyavarch, technicain	OBS	IFREMER
17. El Madani Aissaoui, technicain	OBS	IPGP
18. Pranav Audhkhasi, scientist	Seismics	IPGP
19. Venkata Vaddineni, scientist	Seismics	IPGP

GEOMAR	Helmholtz Zentrum für Meeresforschung Kiel, Wischhofstraße 1-3, 24148 Kiel, Germany
CAU	Christian-Albrechts Universität zu Kiel Institut für Geowissenschaften Otto-Hahn-Platz, 24108 Kiel, Germany
IPGP	Institut de Physique du Globe de Paris Laboratoire de Geoscience Marine 1, rue Jussieu F-75238 Paris Cedex 05 / France
GeoB	FB 4 - Geowissenschaften Universität Bremen Klagenfurter Straße 3-4 D-28359 Bremen / Germany
IFREMER	Institut Français de Recherche pour l'Exploitation de la Mer Z.I. de la Pointe du Diable F-29280 Plouzané / France

3 Research Program

3.1 Scientific background

The lithosphere forms the outermost solid cool shell of the Earth, with an elastic rheology, supporting brittle failure. In contrast, the asthenosphere below the lithosphere exhibits viscous rheology and higher temperatures. The concept of a strong lithosphere was first introduced by Barrell (1914), who realized that the outer part of the Earth must be able to support loads like river deltas over geological timescales. Since the 1960s and hence the plate tectonic revolution, scientists define the lithosphere in terms of a number of plates that move coherently. These plates are composed of both oceanic lithosphere and thicker continental lithosphere and most tectonic earthquakes occur at the boundaries between these plates. Much of the continental lithosphere is between 500 Ma and 3500 Ma old. In contrast, the oceanic lithosphere is generally younger than 180 Ma (e.g., Müller et al., 2008) and continuously created by seafloor spreading at the mid-ocean ridges. The oceanic lithosphere comprises roughly 57% of the Earth's surface and is hence the largest geological unit of the Earth and except at ocean islands covered by water.

The crust, forming the upper portion of the lithosphere, is formed by melting of a pyrolite mantle at the mid-ocean ridges, extracting basaltic liquids to form the ocean crust and leaving a residue of harzburgite forming the underlying lower lithosphere.

Cruise MSM69 focused on two main topics:

(i) studying the crustal accretion process of the Mid-Atlantic Ridge as a function of time, surveying periodicities of crustal/lithospheric formation at slow-spreading rates; and

(ii) revealing the structure of the uppermost lithospheric mantle, including the evolution of seismic velocity structure with age and detecting any layering and seismic properties of the mantle (including the base of the lithosphere).

The cruise is associated to a number of French, UK and US American geophysical campaigns in the equatorial Atlantic, aiming to survey the lithospheric structure formed at slow-spreading rates and yielding the properties of the Lithosphere-Asthenosphere boundary. Most importantly for MSM69 are seismic lines obtained during a multi-channel seismic reflection survey conducted in 2015 - the iLAB cruise (Mehouachi and Singh, 2017; Fig. 3.1; see also chapter 3.1.3).

3.1.1 Structure and properties of the lithosphere

3.1.1.1 Structure and properties of the oceanic crust and uppermost mantle

The primary source of our knowledge of the structure of oceanic crust is the interpretation of seismic refraction experiments. The first classic compilation of seismic data of Raitt (1963) subdivided the crust into three distinct layers, which have formed the reference basis for seismic profiles for the last decades. The upper igneous crust (layer 2) is a region of strong velocity gradients, while the lower crust (layer 3) is relatively homogeneous, although it does show an increase in velocity with depth (e.g., Whitmarsh, 1978). Further, the upper crust has been sub-divided the in Layer 2A, composed of extruded basalts, and Layer 2B, formed by basaltic sheeted dikes (e.g., Christeson et al., 1994). The lower crust, or Layer 3, often called the

"oceanic layer", is inferred to be composed of gabbros (e.g., White et al., 1992). As crust ages, sediments accumulate on the igneous basement, creating Layer 1.

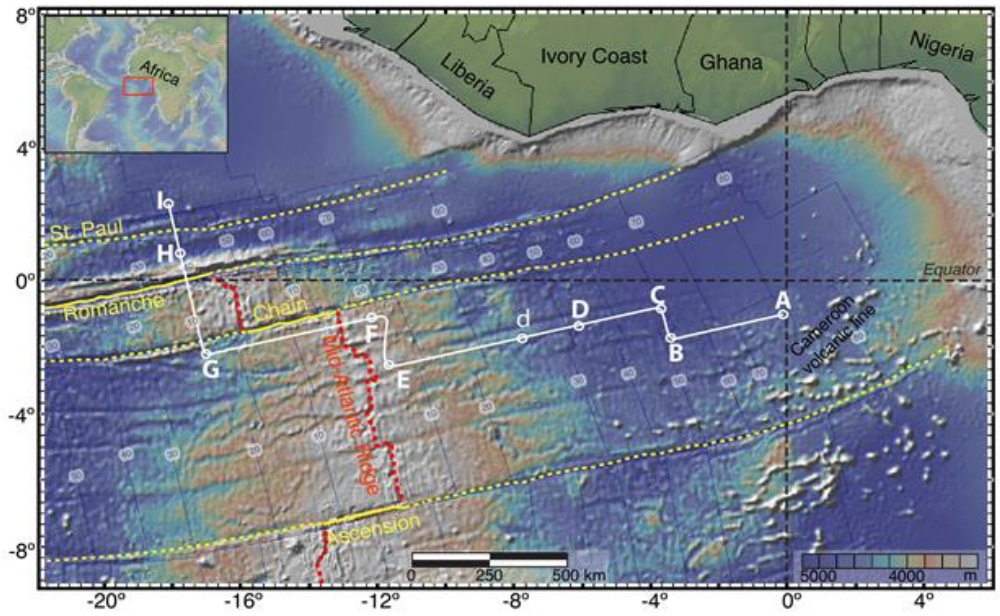

Fig. 3.1: Location map of the survey area and multi-channel seismic data acquired during iLAB cruise.

Raitt (1963) recognized that the oceanic crust is remarkably uniform. He showed that crust is 6.57 ± 1.61 km thick. Three decades later, White et al. (1992) estimated a crustal thickness of 7.08 ± 0.78 km away from anomalous regions such as fracture zones and hotspots, with extremal bounds of 5.0-8.5 km. However, today we know that crustal thickness seems to vary profoundly (Figure 3.2) and is often considered to be related to spreading rate. But even at a given spreading rate crustal thickness may vary by several kilometers (e.g., Grevemeyer et al., 2018). Crustal thickness and structure of the oceanic crust are inherently related to the process of mantle melting at mid-ocean ridges. The amount of melt produced by adiabatic decompression of the mantle and the composition of the resultant igneous crust depend on the temperature, composition, and water content of the mantle source (e.g., Korenaga et al., 2002). Normal oceanic crust with a thickness of 6-7 km and Mid-Ocean Ridge Basalt (MORB) like composition is the result of decompressional melting of a mantle source composed of dry pyrolite with a mantle temperature of ~1300°C (McKenzie and Bickle, 1988). Higher mantle temperatures will cause a thicker crust displaying faster lower crustal velocities and thus crustal thickness and lower crustal velocity can be used as proxies for mapping the effects of mantle melting on crustal accretion.

Relating seismic lower crustal velocities to crustal thickness has been extremely successful. Thus, thinner crust found in some parts of the Indian Ocean indicates along with reduced velocities in the lower crust that crust has been formed at lower mantle temperatures than in the Pacific Ocean (Figure 3.3). Furthermore, focused mantle upwelling along the Mid-Atlantic Ridge may explain along axis variation in crustal thickness (Figure 3.4). Thick crust found in the middle of spreading segments (7 to 9 km) provided significantly faster lower crustal rocks (Vp~7.15 to 7.25 km/s) than thin crust (4 to 6 km) found at the end of spreading segments (Vp~6.8 to 7.0 km/s), suggesting that mantle temperature is a key parameter controlling crustal accretion (Fig. 3.3) and is in agreement with previous model of crustal accretion (e.g., White et

al., 1992). For the slow spreading ridges, crustal thickness may vary from 4 to 8 km. Surprisingly, compilations of the seismic structure of the Atlantic Ocean generally provides crust in the order of 7 to 8 km thick (White et al., 1992) with little evidence for focused mantle upwelling. It might be important to note that among refraction seismologist the White et al. (1992) dataset has often been criticized as most surveys in the Atlantic were conducted on the North American plate off the US East coast (near Blake Spur fracture zone), perhaps indicating that the dataset might be biased. Further, the structure of young crust compiled by White et al. (1992) does not agree well with the structure found by modern surveys, arguing that new data covering a wide range of ages are needed.

Interestingly, even several decades after the concept of seafloor spreading was established, the upper mantle in the Atlantic is poorly studied. Thus, only few long-range seismic

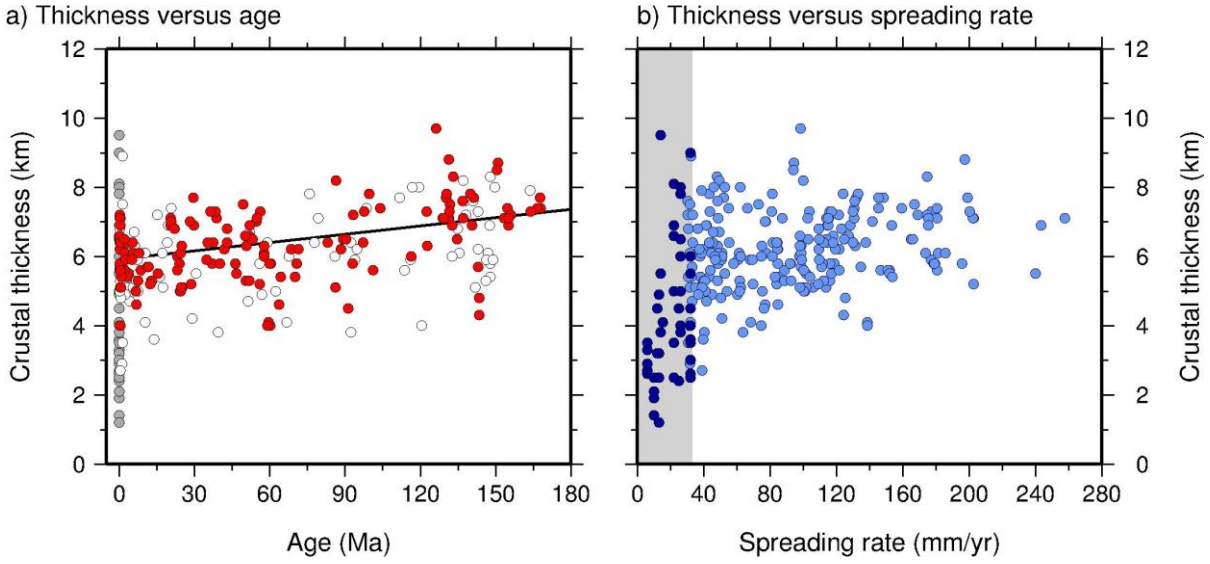

Fig. 3.2: Seismic structure as a function of age and spreading rate (from Grevemeyer et al., 2018)

refraction profiles were conducted. The LADLE group (Whitmarsh et al., 1983) provided a 1000 km long refraction line running north-south in the western North Atlantic. Explosive shots were recorded on 16 OBS (instrument spacing ~50 km). Crustal structure was crudely estimated being in the order of 7.6 km. Seismic energy penetrated down to ~65 km and indicated a layered mantle with velocities ranging from 8.2 to 8.4 km/s below Moho. Underneath, a low velocity zone was inferred. Below 53 km mantle reach velocities of 8.4 to 8.6 km/s. To the south of the Bermuda's, Lizarralde et al. (2004) conducted a 800 km long range profile recording airgun shots on 7 OBS (instrument spacing ~100 km). Crustal thickness varied from 5.5 to 7.1 km and was hence thinner than the average thickness of 7.6 km predicted for curst formed in the Atlantic (White et al., 1992). Pn arrivals were observed out to 400 km and sampled the mantle down to ~40 km. In contrast to the LADLE survey and a Russian survey across the southern Atlantic (Pavlenkova, 1996) no evidence for any low velocity zone in the mantle was detected.

3.1.1.2 Crustal aging and alteration constraint by seismic data

One of the most striking features of the oceanic crust emerging from seismic studies is the variability of Layer 2. Early interpretations by Raitt (1963) demonstrated that Layer 2 compressional wave velocities range widely, from less than 3.0 km/s to more than 6.0 km/s.

Since laboratory measurements on fresh basalts yield velocities of about 6 km/s, low seafloor velocities can only be explained by abundant porosity at a scale larger than that sampled by drilling or dredging (e.g., Hyndman and Drury, 1976).

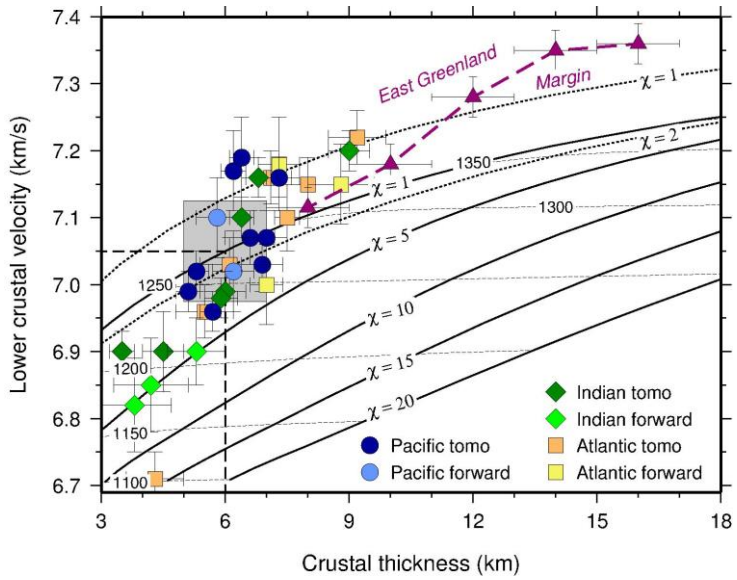

Fig. 3.3: Seismic structure of oceanic crust (Grevemeyer et al., 2018).

Seismic experiments near spreading ridges indicated that seismic velocities in the top of the igneous crust are typically much lower than those in mature oceanic crust. Based on the compilation of sonobuoy seismic refraction profiles, Houtz and Ewing (1976) suggested that upper crustal velocity structure may support an evolutionary process (Fig. 3.5). The most important results were that velocities of the uppermost crust, Layer 2A, increase until about 40 Ma. It is generally believed that hydrothermal precipitation of secondary minerals in open pore spaces of the extrusive basaltic crust is the most likely cause for changing seismic velocity with age. As a consequence, rocks become chemically altered with increasing water/rock ratio and hence crustal age. Thus, alteration is inherently linked to hydrothermal circulation and a key issue in understanding crustal aging (e.g., Alt et al., 1986).

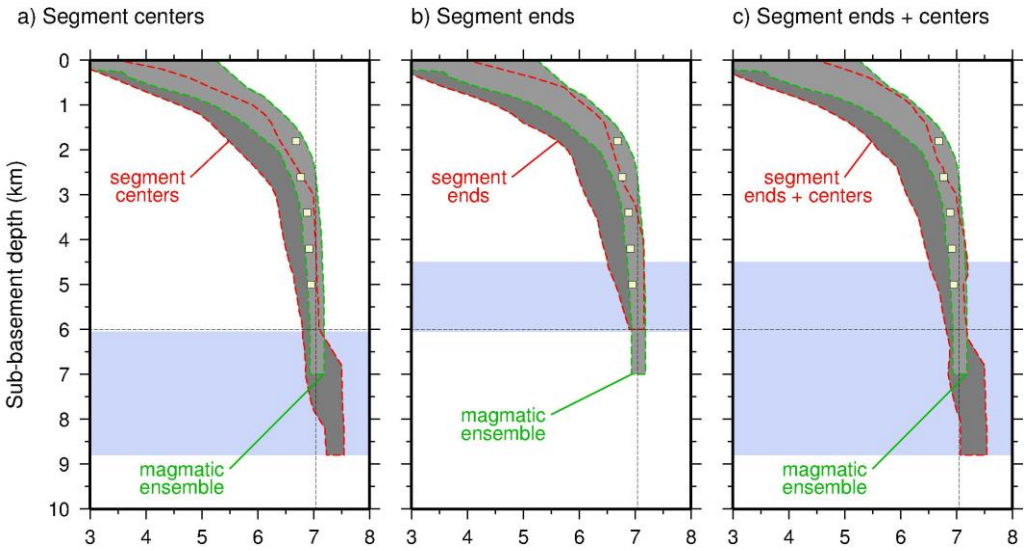

Fig. 3.4: Structure of Atlantic crust (compilation of Grevemeyer et al., (2018))

Updating the Houtz and Ewing (1976) data set, Grevemeyer and Weigel (1996) presented a new global compilation of seismic refraction compressional wave velocity data. The compilation covers a wide range of seafloor ages, from juvenile to 160 Ma old crust. The new

compilation showed a systematic variation with age. Assuming that the variation of Layer 2A velocities is given by all arrivals turned in the uppermost igneous crust, the new data support the idea that Layer 2A velocity is indeed a function of plate age.

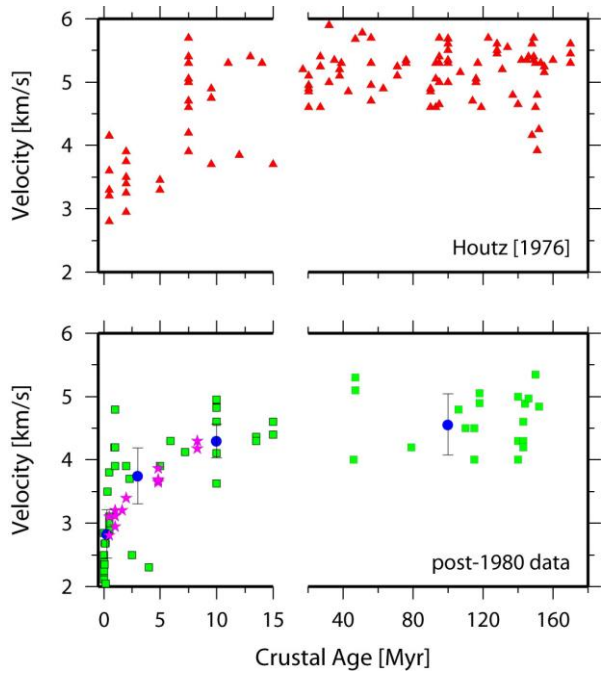

Fig. 3.5: Upper crustal seismic structure as a function of plate age (from Grevemeyer and Bartezko, 2003).

In 1995 the first systematic study was conducted at the southern East Pacific Rise to carry out a seismic flow-line experiment to investigate age-dependent features in the structure of layer 2a, covering 0.5 to 10 Ma old crust (Grevemeyer and Weigel, 1997; Grevemeyer et al., 1998). At the ridge crest, seismic velocity at the top of the crust was 2.35 km/s. With distance from the ridge axis and hence age velocities increased rapidly increased close to the ridge axis (~0.8-1 km/s per 1 Ma) and slowly thereafter (0.1-0.2 km/s per 1 Ma), reaching a velocity of ~4.5 km/s in 10 Ma old crust (Grevemeyer and Weigel, 1997; Grevemeyer et al., 1999), closely matching trends derived from global data sets (e.g., Grevemeyer and Weigel, 1996; Carlson, 1998; Grevemeyer and Bartetzko, 2003)(Fig. 3.5).

At fast spreading ridges no evidence was found that hydrothermal activity affects mid-crustal and lower crustal properties (Grevemeyer et al., 1998; Sleep and Barth, 1997). However, hydrothermal circulation is strongly dependent on the permeability structure; thus, faults and fissures will affect fluid migration and hence the evolution of crust. Therefore, mid-ocean ridges dominated by tectonism may experience more extensive hydrothermal alteration, because faults and fractures provide pathways for fluids to enter the crust. Seismic studies from extinct spreading ridges revealed that lower crustal velocities are well below those of typical mature oceanic crust (Osler and Louden, 1995; Grevemeyer et al., 1997), which has been attributed to an increasing degree of tectonism preceding extinction. In addition, alteration of lower crustal rocks may contribute. Unfortunately, little is known from so-called normal oceanic crust. However, Sleep and Barth (1997) provided an initial assessment by re-visiting velocity-depth solutions compiled by White et al. (1992). They divided the data set into Pacific and Atlantic crust, and into young and old crust, and resampled the solutions into 1 km bins. For the Pacific Ocean, these average profiles show the well documented increase in upper crustal velocities and constant velocities in the lower crust. Thus, the approach provided no indications that off-axis hydrothermal circulation affects lower crustal properties of fast spreading lithosphere. For slow spreading Atlantic crust, however, upper crustal velocities increase, while velocities in the lower crust decrease significantly with age.

Temperature can influence the compressional wave velocity of basalts, but it has a small effect (<5%) until solidus temperatures are reached. Thus near mid-ocean ridges, temperature variations will not be detected by compressional waves, except in the vicinity of an axial magma

chamber. However, seismic studies indicate that low velocities beneath mid-ocean ridges are due to elevated temperatures and the presence of partial melt in the uppermost mantle (Dunn and Toomey, 1997). In addition, Grevemeyer et al. (1998) showed that mantle velocities are lowest near the ridge crest, and increase with distance from the ridge axis, until they research values of approximately 8.0 km/s in 10 m.y. old crust (Grevemeyer et al., 1998). In mature crust, typical upper mantle velocities of 8.1 to 8.2 are common (e.g, White et al., 1992). However, processes controlling increasing velocities in the mantle over millions of years are poorly understood.

At the fossil Aegir Ridge, Grevemeyer et al. (1997) detected an anomalous Moho transition zone. One explanation is that the uppermost mantle contains some amount of hydrothermally altered peridotites. Less than 10% peridotite must be serpentinized to produce the observed velocities of 7.6-7.8 km/s. Major reductions in crustal thickness within the rift valley are related to crustal-scale normal faulting (Osler and Louden, 1995; Grevemeyer et al., 1997). Thus, pathways for hydrothermal alteration are provided by the pervasive fracturing of the entire crust. Because global data suggest that crustal scale alteration might be abundant in slow spreading crust, fluids may even penetrate into the upper mantle to alter mantle peridotite. Consequently, if faulting cuts through the entire crust, alteration of mantle rocks might be a common feature. However, serpentinization could explain reduced velocity in the mantle, but fails to explain Pn velocities increasing with age.

3.1.1.3 Structure and properties of the Lithosphere-Asthenosphere Boundary (LAB)

The oceanic lithosphere cools and thickens with age, resulting in the subsidence of the seafloor, a decaying geoid height and a decreasing heat flow while moving away from the ridge crest. The term ‘lithosphere’ has to be clarified by adding the physical property or state variable which is used to define the base of the lithosphere (Eaton et al., 2009), which is called the Lithosphere-Asthenosphere Boundary, or LAB. In its original concept the LAB is the mechanical boundary layer separating the rigid outer shell of Earth from the viscously deforming mantle and hence is defined by a sudden increase in strain rate. For scientists working on lithospheric cooling or mantle convection, it is defined as a transition layer at the base of the thermal boundary layer that separates the conductive lid above from the convective mantle below where the temperature is adiabatic. In lithospheric cooling models the base of lithosphere is defined by a constant basal temperature. Seismologists define the LAB by the presence of a low S-wave velocity zone beneath a high velocity lid. Further, a change in seismic anisotropy in the upper mantle has been found to mimic the LAB. Since the solid lithosphere should be electrically resistive whereas the viscous asthenosphere should be conductive, the boundary between a high resistivity layer above a low resistivity asthenosphere is interpreted as LAB.

The most direct evidence of the base of the mechanical lithosphere has come from surface wave studies where the lithosphere was associated with a high S-wave velocity above a low velocity and high attenuation asthenosphere with a gradual decrease in the velocity and vertical change in seismic anisotropy (Nishimura et al., 1989; Nettles and Dziewonski, 2008). Receiver functions from seismic broadband data from borehole seismometers installed in the deep ocean basins suggested a sharp boundary at the base of the lithosphere (Kawakatsu et al., 2009), indicating that the LAB occurs ~80 km for lithosphere 60 to 120 Ma old. Other seismological dataset support these observations. Rychert and Shearer (2011) mapped the depth and nature of a seismic discontinuity across the Pacific, being interpreted as LAB. Using

variations in the shapes of stacked SS waveforms, they found that the depth to the discontinuity varies from 25 to 130 km and correlates with distance from the ridge along mantle flow lines. This implies that the depth of the LAB depends on the temperature of the underlying asthenosphere and is defined by a best fitting isotherm of 930°C.

In the 1980s, long-range seismic refraction and wide-angle recording of large explosive charges fired in the Central Atlantic Ocean and provided wide-angle reflections at offsets of 200 to 600 km (Pavlenkova, 1996). Several deep-seated reflectors were observed below the South American Plate. However, their interpretation remained enigmatic. More recent seismic work in the ocean basins revealed similar wide-angle phases at large offsets, but also their interpretation remained enigmatic (e.g., Smallwood et al., 1999; Grevemeyer et al., 2001a). Nevertheless, these studies indicate that standard airgun wide-angle profiling can image the lithosphere, reaching at least down to 30-50 km by providing offsets of mantle phases at 200-300 km (Smallwood et al., 1999; Grevemeyer et al., 2001a; 2001b). Interestingly, reducing the shot induced noise-level by increasing the shot interval of airguns resulted in improved data quality and allowed offsets of up to 400 km in the Atlantic Ocean (Lizarralde et al., 2004). This fact is supported by recent long-range seismic profiling conducted in the Pacific Ocean, imaging sub-Moho structures and providing wide-angle reflections that approach the Pn branch near 185 km and 400 km range (Dan Lizarralde, pers. communication). Preliminary analysis of the airgun shots recorded at ocean-bottom seismometers (OBS) suggested that these wide-angle reflections arise from discontinuities at ~12 and ~30 km below Moho.

3.1.1.4 Lithopheric cooling and heat flow

At mid-ocean ridges lithosphere is formed continuously by seafloor spreading. As lithosphere spreads away from the ridge axis it cools and subsides. Following the realization that seafloor heat flow is highest at the ridge crest and decreases with distance and hence plate age (Langseth et al., 1965) the systematic variation of ocean depth and heat flow with age became the primary constraint on models of the thermal evolution of the lithosphere (e.g., Stein and Stein, 1992; Hasterok, 2013). However, a significant discrepancy exists between the heat flow measured at the seabed and the higher values predicted by thermal models of a conductively cooling lithosphere. This heat flow discrepancy is thought to reflect the transport of significant amounts of heat by circulating fluids (Lister, 1972). Results of this circulation are exhibited most spectacularly at the ridge crests where venting of fluids at temperatures up to 400°C occurs. On the ridge flanks the ongoing heat loss of the lithosphere drives the circulation of fluids through the porous upper layers of crust. Here at the much lower temperatures the vigor of hydrothermal circulation is reduced. However, due to the vast areas of the seafloor where such circulation can occur, perhaps 70% of the hydrothermal heat loss is off-axis (Stein and Stein, 1994).

In the axial zone, the observation of high temperature fluid venting from open fissures is evidence that high permeability path ways like fault zones control convective fluid circulation and hence the cooling process of very young crust. Within older crust, fluid circulation continues and appears to be controlled by the background permeability, yielding a heat flow pattern which roughly mimics the topography (e.g., Davis and Villinger, 1992; Fisher et al., 1994). In general, heat flow determinations on the ridge flanks reveal values well below the theoretical prediction (Stein and Stein, 1994; Villinger et al., 2002), suggesting that hydrothermal circulation is vigorously removing heat out of the oceanic lithosphere.

In crust approximately older than 60 Ma, however, the observed heat flow approaches the predicted heat flow derived from plate cooling models, indicating that hydrothermal circulation has largely ceased (Stein and Stein, 1994). The seafloor age where the observed heat flow approaches the predicted heat flow is often called the 'sealing age'. The sealing age is controlled either by a sediment cover with low vertical permeability, restricting the exchange of seawater between the crust and ocean, or precipitation of secondary minerals, reducing the permeability of the crust to values too low to support hydrothermal circulation. Thus, the sealing age is strongly dependent of regional features, like seafloor relief and sedimentation rate, varying from a few millions of year to ~80 Ma. (e.g., Villinger et al., 2002; Stein and Stein, 1994). Some heat flow studies on old oceanic crust reveal heat flow pattern which may be caused by active hydrothermal convection in Layer 2A (Fisher and von Herzen, 2005). However, this interpretation still has to be confirmed by more measurements.

Hasterok (2013; Hasterok et al., 2011) has recently shown that global filters can be selected removing sites affected by hydrothermal cooling from a global dataset. The approach basically rejects all sites where sediment thickness is <400m and where significant seafloor topography occurs within 60 km of the heat flow station. After filtering the data, heat flow allows much more robust estimates of the physical properties of a cooling lithosphere than any other parameter, including seafloor depth and geoid height (see work of Hasterok (2013) for details). In general, three different kinds of models were discussed to explain cooling of the lithosphere. The first model discussed was the half-space cooling model which was later replaced by the plate cooling model. Thus, while the half-space cools throughout the semi-infinite domain, the plate model assumes that cooling can continue to a fixed depth, the plate thickness. In contrast, the third model, the Chablis model, assumes a constant lithospheric heat flow. Based on his filtered heat flow dataset Hasterok (2013) could show that only the plate cooling model provides robust estimates after considering statistical constraints. Interestingly, the Hasterok (2010; 2013) model indicates a thinner plate of 90 km than previous models, with a plate thickness of 125 km or 95 km (Stein and Stein, 1992). The best fitting mantle temperatures ranges from 1350°C to 1425°C (Hasterok, 2010; 2013).

3.1.2 The Equatorial Mid-Atlantic

The Central Atlantic Ocean opened approximately 120 Ma ago (Müller et al., 2008). During the separation of Africa from South America a major shear zone developed, forming the transform passive margins of Ghana and Cote d'Ivoire in Africa and French Guiana and Northern Brazil in South America. The formation of large and extensive transform margin affected seafloor spreading in the Central Atlantic, forming large offset transform faults, like the Romanche Transform Fault with an offset of ~1000 km (Fig. 3.1). To the north and south several other long-lived large offset fracture zones occur, including the Chain Transform fault near 2°S with an offset of ~400 km. Interestingly, the initial segmentation of the Mid-Atlantic Ridge still governs the segmentation of the MAR (e.g., Müller et al., 2008) and the transform faults and their traces - the fracture zones - are gigantic linear features. For the Atlantic Ocean such linearity is unique, as the relative motion between the three plates of Africa, South America, and North America caused complex fracture zone pattern further north. Therefore, the Central Atlantic provides the rare opportunity to conduct surveys that require a linear profile design as

it's needed for seismic refraction and wide-angle work. Elsewhere in the Atlantic, a linear long-range profile would cross segment boundaries or hotspot tracks.

Since Africa rifted apart from South America spreading half rate to the south of the Chain Transform was in the order of 1.75 cm/yr (Müller et al., 2008), indicating a rather continuous spreading process over time. Base on gravity data crustal thickness remained reasonable constant at 4 to 7 km (Wang et al., 2011). Crustal production may have changed over time, though. Thus, in the last ~40 Ma crust is predicted being in the order of 4-5 km while crust of 40 to 120 Ma. is in the order of 6-7 km. However, the study generally fails to predict crustal thickness variation caused by focused mantle upwelling along the crest of the MAR, indicating that uncertainties of gravimetric estimates are rather high.

3.1.3 First results from iLAB survey

In March to April of 2015 the iLAB survey was conducted in the equatorial Atlantic (e.g., Mehouachi and Singh, 2017), collecting ultra-deep seismic reflection data aboard Schlumberger's seismic vessel WESTERN TRIDENT (Figure 3.1). Part of this survey provides industry-type multi-channel seismic reflection data coincident with seismic profile P01 obtained during our survey - MSM69. To enhance the low frequency signals, the seismic data obtained with the WESTERN TRIDENT were acquired using a 12-km long multi-sensor Isometrix® streamer, towed at 30 m depth. The streamer contained two hydrophones and three-component accelerometers spaced at 0.75 m. The pressure data were pre-processed in real time to produce a receiver spacing of 3.125 m. The seismic source was composed of 6 sub-arrays with 8 air-guns each, providing a total volume of compressed air of 10170 cubic inch (167 litres) at an operating pressure of 2000±100 psi. The seismic source was towed at 15 m and the shot interval varied from 75 m to 50 m, and record length from 30 s to 20 s. The vessel speed varied from 3.4 to 4 knots.

A total of 2,775 km ultra-deep seismic reflection data was acquired starting from Greenwich Meridian at 1º S, at about 75 Ma of oceanic lithosphere (Figure 3.1) in nearly E-W direction, crossing the Mid-Atlantic Ridge at 1.3º S, corresponding to zero age of the lithosphere. This part of the profile spans 0-75 Ma of the oceanic lithosphere on the African Plate. The profile extends approximately 500 km west of the Mid-Atlantic Ridge and transects 0-25 Ma of the oceanic lithosphere on the South American Plate. This E-W profile is connected with an N-S profile that traverses the two most prominent fracture zones and a transform fault on the Earth, Chain Fracture Zone, Romanche Transform Fault and St Paul Fracture Zone.

IsoMetrix data require special processing, and WesternGeco provided an infield geophysics team to perform initial preconditioning of the raw measurements into total pressure (P), plus vertical (Az) and horizontal (Ay) pressure gradients, at 3.125 m receiver intervals. A key objective of the project was to extract usable frequency content down to 1.5 Hz, and hence care was taken during the noise removal process to preserve low frequencies. The pressure and vertical gradient data were combined to remove the effect of the receiver-side ghost. Since the seafloor is very rugose across the survey area, wavefield scattering is a key issue, as well as the related multiples. Thus, the removal of scattered noise and multiples is essential for extraction of the weak signals from the mantle and LAB at 50-70 km depth.

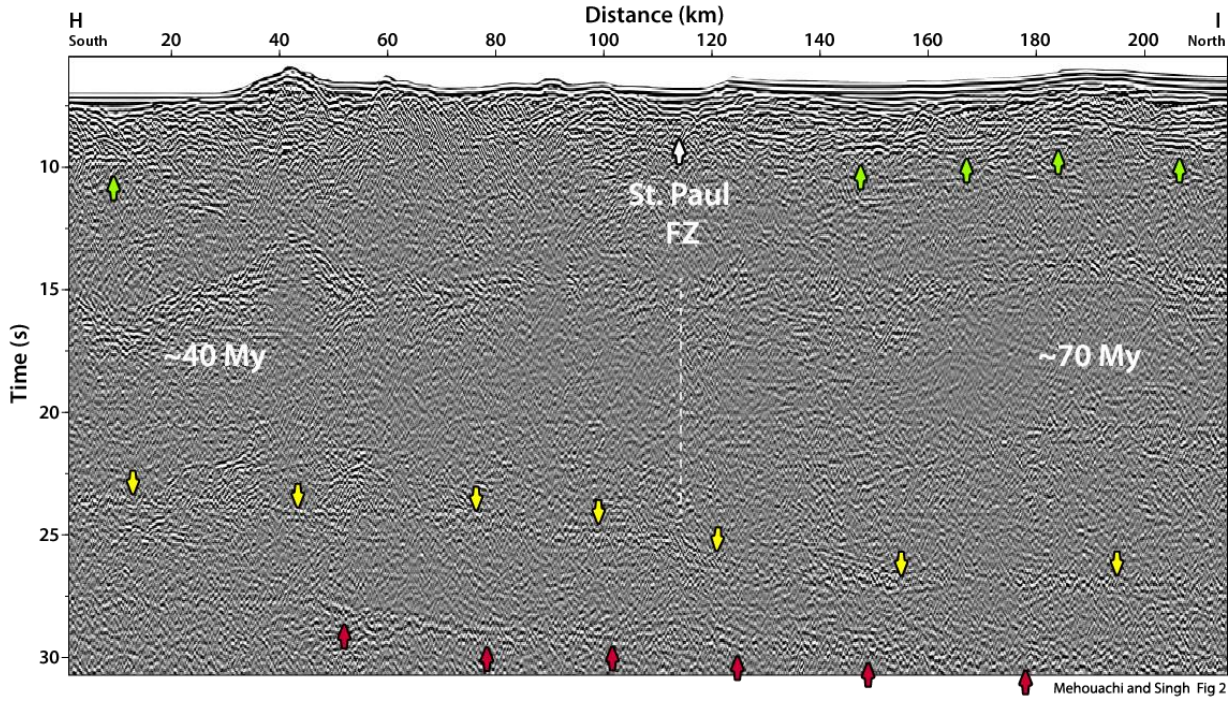

Fig. 3.6: Time domain seismic image: The seismic image along profile (H-I in Fig. 3.1). Green arrows: Moho reflections; yellow arrows: top LAB reflections; red arrows: bottom LAB reflections. The St Paul fracture zone (white arrow and dashed line) lies between 100 and 120 km distance, separating 70 Ma old oceanic lithosphere in the north from 40 Ma old lithosphere in the south. (from Mehouach and Singh, 2017).

The results from the reflection data across the St Paul FZ (Mehouachi and Singh, 2017) show two reflections; the top reflection varies from 23.5 s south of the St Paul FZ to 27 s north of it, whereas the lower reflection from 27 s to 30 s (Fig. 3.6). The age contrast along the profile is from 40 to 70 Myr across the St Paul zone. The depth conversion of the seismic image using simple velocity model indicates that the top reflection varies from 72 km to 88 km and the lower reflection from 88 to 100 km across the fracture zone. The polarity of the upper reflection is negative to that of the seafloor whereas that of the lower reflection is positive. Based on relative amplitudes of these reflections, we find that one would require 8.5% velocity contrast at these boundaries. We find that ~1.4% if melt would be required to explain this decrease in velocity. We also found that the upper reflection corresponds to an isotherm of 1260° C whereas the lower reflection to 1355° C. As this temperature is lower than the melting temperature of dry olivine, the presence water would necessary to have melted. The concentration of water increases with age, but the total amount of water remains constant suggesting the water, hence the melt, enters the channel at the ridge. We propose that the LAB consist of a water-rich melt channel, which deepens with age, but whose thickness decreases with age (Mehouachi and Singh, 2017).

3.2 Objectives and goals

MSM69 has been propose to survey changes of the physical properties of the lithosphere as a function of plate age, studying oceanic lithosphere as it matures with time and hence distance from the spreading ridge. Aims are

1. Mapping variations in the accretionary process over millions of year, revealed by crustal thickness and seismic velocities. The oceanic lithosphere is created by seafloor spreading at mid-ocean ridges. However, periodicities in the accretion may affect lithospheric formation. Variations of melt generation and mantle temperature will affect crustal formation, which will in turn affect crustal thickness and crustal velocity structure (see Fig. 3.3). Crustal thickness and seismic velocity are therefore proxies to assess periodicities in crustal accretion over time.

2. Surveying Atlantic-type crust in a poorly surveyed portion of the ocean. Crustal structure of slow spreading ridges or Atlantic-type crust has been used for many years as reference for studies of various processes, including studies of mid-ocean ridges and continental margins. However, the compilation of White et al. (1992) is based on data acquired before 1990, with the majority of data from the Western Atlantic off the US East coast. We like to challenge the view based on the White et al. compilation and like to update the reference basis for seismic studies. Further, a number of compilations of global data suggest that crust thickens with age (e.g., White et al., 1992). Is this observation real or caused by biased data?

3. Revealing upper crustal velocity structure as a function of plate age and relating changes to the hydrogeological regime as expressed by heat flow data. It is well known that upper crustal velocities increase with age and are controlled by hydrothermal precipitation of alteration products into open pore spaces of the extrusive crust. We like to survey the relationship between changes of the seismic properties of the upper crust and the sealing age (hydrothermal mining of heat). Thus, are changes of Layer 2 seismic velocity indeed related to the sealing age or does the velocity saturates (remains constant) at younger ages?

4. When does hydrothermal circulation cease in the Central Atlantic Ocean? Hydrothermal circulation is called ceased when the observed heat flow approached the conductive heat flux. Globally it occurs on seafloor roughly 60 Ma old. However, do we observe the same trend or does sealing occurs earlier or later?

5. How does the upper mantle change with age? Is the mantle layered? We know very little about the mantle structure in the oceans. We know seismic velocities are generally <7.6 km/s at zero-aged and in the vicinity of MORs, while normal mantle has velocities of >8.1 km/s. However, how do velocities change with age? How important is serpentinization for producing reduced velocities in oceanic mantle? Is the mantle indeed layered as indicated in studies conducted in the 1970s and 1980s?

6. Imaging the LAB (Lithosphere Asthenosphere Boundary) using seismic refraction and wide-angle data. In continental settings the LAB has been imaged using seismic refraction and seismological data. Large airgun arrays may not reach the same peak pressure as explosives commonly used for long-range soundings of the continents. However, a dense shot spacing (allowing stacking) and the high dynamic range of modern receivers should compensate the source effects. Recent surveys have proven that we can image several tens of kilometers into the ocean lithosphere (see discussion above). Thus, using modern recording systems and large volume airgun arrays we should be able to image the ocean lithosphere down to 50 km, perhaps down to 80 km. In lithosphere of 2 to ~60 Ma we should be able to sample the LAB as it will be

within ~5 to 30 km below Moho. It would be the first marine survey ever conducted to image the LAB from the ridge flank into an ocean basin.

7. Construction of a plate cooling model for the Central Atlantic Ocean. Newly collected heat flow data along a single transect and high resolution basement topography will provide an excellent dataset to calibrate a cooling model which is constraint by an image of the oceanic crust and the LAB.

8. Combining data and constrains from iLAB survey (see 3.1.3) and MSM69. This cruise is closely related and nurtured by the ERC advanced grant of Prof. Satish Singh of Institut de Physique du Globe, Paris (IPGP), providing industry-type multi-channel-seismic (MCS) reflection data along the main seismic transect P01. Constraints from both surveys will be interpreted jointly, providing unique insights into the structure and architecture of slow-spreading lithosphere.

To full fill the goal, an 1100 km long seismic profile, called P01, was shot in the equatorial Atlantic to the south of the Chain transform fault. The profile runs from approximately 50 Myr old seafloor in the Guinea Basin across the Mid-Atlantic Ridge, terminating about 80 km westward of the ridge crest. 71 ocean-bottom-seismometers (OBS) and hydrophones (OBH) were placed along the profile at a variable spacing of 10 to 20 km. The profile was shot at an interval of 410 m using a 86-litre airgun array fired at 210 bar.

Excellent weather conditions and a much shorter than expected turn-around and recovery time of the ocean-bottom seismic station allowed to shot a short second profile along the St. Paul fracture zone. 14 OBS/H were deployed along a 120 km long profile, called P02. Shots were fired at a much shorter shot interval of ~165 m.

4 Narrative of the Cruise

MARIA S. MERIA left the port of Mindelo on the island of Sao Vincente on 14th of November 2017 at 23:00 local time. One day earlier, however, a sand storm on the 13th of November forced a redirection of the flight from Lisbon, changing it final destination from Sao Vincente to Praia. Thus, 16 scientists and 6 crew member were “stranded” on the island of Praia in the southeast of the archipelago of Cape Verdes. Unfortunately, it was not possible to bring all scientists and crew in time from Praia to Sao Vincente. Thanks to Fortuna, it was possible to collect the “lost” scientists and crew in the morning of the 15th of November offshore of Praia at the pilot station. At about 11 a.m. on Wednesday the 15th of November 2017 the MERIAN left the archipelago, sailing for the next six days about 1500 nm southward and across the equator into the working area (Figure 4.1). About 3 hours after leaving Praia the Kongsberg swath-mapping system EM122 was switched on, recording continuously bathymetric data. Mapping was only suspended during recovery of ocean-bottom-equipment as the acoustic signals of the EM122 would interfere with the acoustic release system of the gear place onto the seafloor.

During the transit into the working area ocean-bottom-seismometers (OBS) and ocean-bottom-hydrophones (OBH) were prepared. In addition, the two airgun arrays consisting in total of 12 G-guns were setup. Preparation included two releaser tests of GEOMAR gear. During the first test on 17th of November at 9:00 a.m. the releasers were lowered down to 1000 m and

communication with a hydrophone mounted into the hull of MERIAN was established. The second test was on 18th of November at 9:00 h. Releasers were lowered to 2000 m and in parallel a CTD was run, recording the sound profile for the EM122. Thereafter, French partners tested the communication between the ship's hydrophone and a French OBS lowered with the winch down to 200 m.

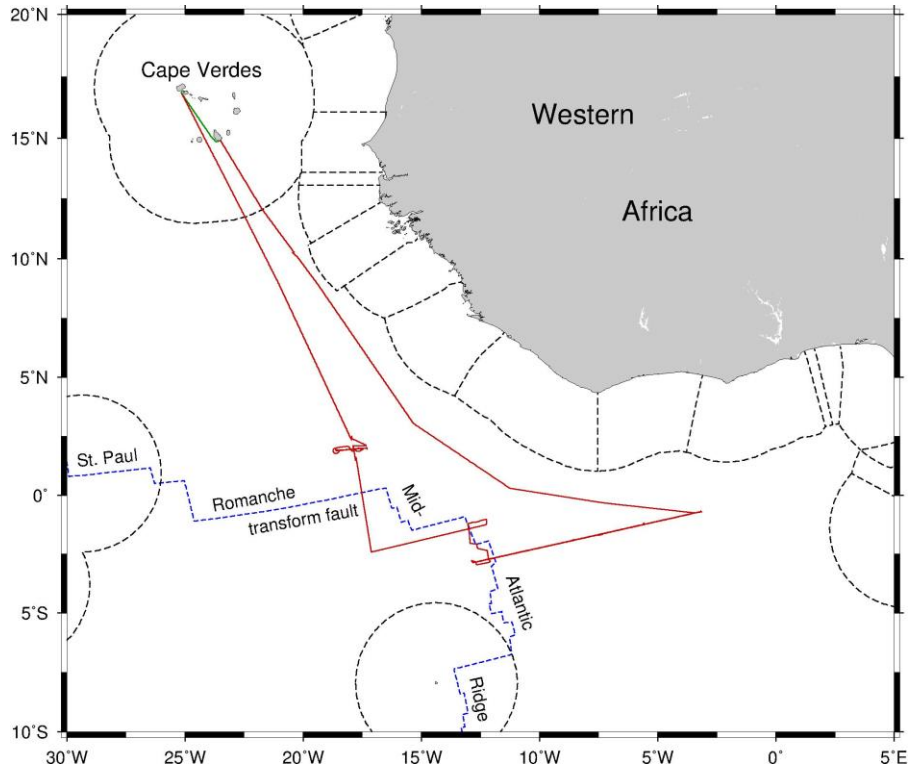

Fig. 4.1: Location map and track chart of MSM69.

Approximately at midnight of Sunday 19th of November MARIA S. MERIAN crossed the equator.

On Tuesday 21st of November, the first seismic station was deployed at 9:38 UTC along the 1100 km long seismic transect, running from approximately 50 Mio. years (Myr) old seafloor in the Guinea Abyssal Plain, across the Mid-Atlantic Ridge, into just ~1 Myr old seafloor of the South American Plate. Until Saturday 25th of November in total 71 OBS and OBH were deployed, namely 17 GEOMAR-OBH, 24 GEOMAR-OBS, and 30 IFREMER OBS. Further, three heat flow stations were conducted on ~48, ~30, and ~20 Myr old seafloor, providing 27 successful geothermal measurements.

The deployment of the two airgun arrays took place on Saturday 25th of November at 13:00 h. About one hour later, both the starboard and port arrays were in the water. The first test shots were fired on 25th of November at 15:00 UTC or 14:00 local time. At 16:21:30 UTC the MERIAN was on the seismic profile and shot #1 was fired. For the next ~7 days shots were fired every 210 s or 3.5 min at a speed of 3.8 kn and hence resulting in a shot spacing of about 410 m. Parallel to the airgun survey, shallow sediment stratigraphy was surveyed using the Parasound system.

On 26 of November at ~14:00 UTC a flotation of the starboard array was lost. The speed was reduced to 2 kn and the starboard array was recovered (14:25 UTC) and a new flotation added. Less than an hour later (14:59 UTC) both arrays were in operation again.

After about three days of continuous airgun operation a pressure hose of a 5 litre G-gun (#1) of the port array failed. The gun was suspended on 28th of November on 16:30 UTC. Latter, at 19:26 UTC the pressure of the port array dropped from 205 to 130 bars. Gun #4 was suspended at 19:37 UTC. Another drop in pressure occurred at 19:53 UTC and gun #6 was suspended as well. Yet, the starboard array remained in full operation. However, on the next day – 29th of November – the pressured drop dramatically and we had to suspend gun #8 of the starboard array. The chief scientist therefore decided to maintain both arrays. At 9:10 UTC operation of the port array was suspended and the array was recovered. MERIAN turned around and went back to the east for approximately 2 h, returning on the profile at ~11:40 UTC. All pressure connections between the airguns and the supply hoses were changed and one electric trigger cable was maintained. At ~12:30 UTC the port array was re-deployed and operation started at 12:59:30 UTC. At 15:07 the operation of the Starboard array was stopped and the array was recovered and maintained and re-deployed. At 16:35 UTC both arrays were on duty and all 12 guns fired again.

On 30th of November gun #4 of the port array lost pressure and was suspended at 19:33 UTC. Fortunately, all remaining guns did their duty until the last shot was fired on 2nd of December 2017 at 10:21 UTC. In total 2777 shots were fired along profile p01.

After finishing the airgun shooting a daily routine established. Thus, from ca. 12:30 UTC of 2nd of December to 9th of December 2017 we either recovered the 71 OBS/H or conducted heat flow surveys, moving slowly from east to west along the seismic transect. On 9th of December at 20:45 UTC all 71 OBS/H were on deck and five additional heat flow surveys were conducted, adding another 50 successful and only one failed penetration.

On Saturday 9th to Tuesday 12th of December, we conducted a multibeam mapping survey of the axis of the Mid-Atlantic Ridge between ~3°30'S to 1°30'S and run parallel to the iLAB MCS profile obtained in 2015. We crossed the equator two hours after lunch of 12th of December while "diving" into the valley of the Romanche transform fault. At 23:20 UTC, we left the mapping track and conducted a short Parasound profile to study the next heat flow site between Romanche and St. Paul fracture zone on approximately 60 Myr old seafloor. On 13th of December the heat probe was lowered and the Bremen Group "burned again the midnight oil" conducting another 8 successful measurements. After a short transit of just 3 hour the 10th heat flow survey was conducted in the valley of the St. Paul fracture zone.

In the early morning of 14th of December at 3:31 UTC the first ocean-bottom station was deployed along seismic profile P02 along the St. Paul Fracture Zone. In total 14 OBS/H were deployed at 7.5 to 15 km spacing. At 12:00 UTC the airguns were deployed about 5 nm to the northwest of the profile. The first "warm-up-shot" was at 12:42 UTC and at 13:25:30 the first shot was fired along the seismic profile. Shots were fired every 90 s at a speed of 3.5 kn, resulting into a short spacing of 170 m. About 22 hours later, on Friday 15th of December at 11:20 UTC the last shot was fired. Airguns were recovered and the first OBH released. At 13:34 UTC it was on deck and until Saturday at 7:13 UTC all 14 OBS/H were recovered. After 8 hours of seafloor mapping, extending the coverage of the St. Paul fracture zone, the next heat flow survey was conducted, obtaining 11 geothermal measurements from the centre of the fracture

zone towards its northern boundary. On Sunday 17th of December the heat probe was recovered at 9:30 UTC and a second short mapping programme was conducted. Latter, at ~17 h the last heat flow station and last scientific operation in the survey area was carried out. At 22:01 UTC the heat probe was back on deck and MARIA S. MERIAN sail towards the Cape Verdes, were the vessel met at 8 a.m. local time on 21st of December 2017 the pilot and a successful cruise ended in the harbor of Mindelo.

5 Preliminary results

5.1 Performance of scientific equipment

5.1.1 EM122 Kongsberg echosounder

The MARIA S. MERIAN is fitted with a Kongsberg EM122 1°x2° multi-beam deep ocean echosounder, with two transducer arrays fixed to the ship's hull operating at 12 kHz. Data acquisition is based on successive transmit-receive cycles of this signal. The transmit beam is 150° wide across-track and 1° along-track direction. The system has 432 beams, sampling seafloor depth at high resolution. The beam spacing can be defined as equidistant or equiangular, and the maximum seafloor coverage fixed or adjusted according to seabed and weather conditions. Seabed depth and reflectivity are recorded against UTC and GPS location. The raw depth data are processed to obtain depth contour maps, and the acoustic amplitude processed to obtain backscatter amplitudes. Swath bathymetry and backscatter data were acquired within the survey area of the equatorial Atlantic and during transit in international waters and within territorial waters of the Republic of the Cape Verdes. During MSM69 we obtained 3972 nm of along-track swath bathymetry.

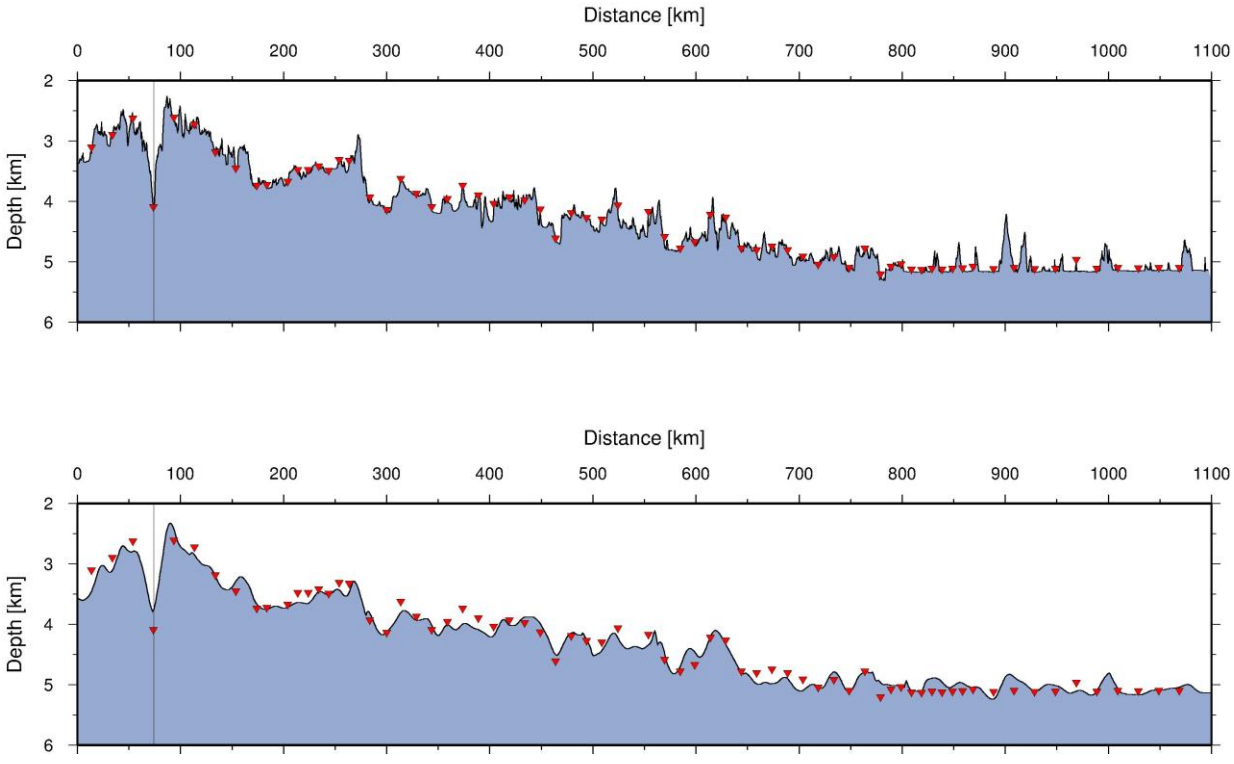

Fig. 5.1: (top) Bathymetry obtained along the main seismic transect P01; (bottom) predicted topography along the same profile. Red inverted triangles indicate OBS deployment sites plotted at EM122 depth. Note the bias with respect to the predicted topography of several hundreds of meters.

5.1.2 Sediment echosounding system – PARASOUND®

On board Maria S. Merian, an ATLAS HYDROGRAPHIC PARASOUND® P70 System is installed permanently for sediment echo sounding. The main goal of using the PARASOUND® System is the selection of suitable sites for sediment sampling and deployments of the heat flow lance. The system uses the parametric effect that means that two acoustic signals (in our case 19.8 kHz (PHF) and an automatically generated corresponding signal) are emitted simultaneously which produce through nonlinear acoustic interactions a secondary target signal of 4 kHz (SLF). This pulse travels within the emission cone of the original high frequency waves, which is limited to an opening angle of ±2°. Therefore, the footprint size of 7% of the water depth is much smaller than for conventional 3.5 kHz systems. In general the Parasound® P70 has a range from 18 – 33 kHz for the first primary frequency (PHF, primary high frequency). The second primary frequency can be varied from 18.5 - 39 kHz leading to a frequency range of 0.5 – 6 kHz with a beam width of 4.5° for the parametric difference signal, the secondary low frequency (SLF). Additionally, also the parametric sum of the primary frequencies, the secondary high frequency (SHF), can be recorded. The SLF data achieve a vertical resolution of better than 15 cm in the sediment and a maximum penetration of 100 – 200 mbsf. The maximum acoustic penetration is strongly depending on local bottom conditions and grain sizes. It varies during MSM69 in general from 0 – 200 m.

On all profiles during MSM69 the system is operated in the Quasi-Equidistant mode. This mode provides an optimal lateral coverage of the sea floor, since the echosounder calculates an intertwined trigger sequence using the 'unused' travel time of the signal in the water to emit additional pulses. This generates a nearly equally spaced transmit/receive sequence with at least twice the rate of a standard send-receive-send-sequence. Real part and phase of the envelope from the returned echo signals are saved in the ASD format. Because of the limited penetration of the echosounder signal into the sediment, only a small time window (depth window @ 1500 m/s) close to the seafloor is recorded and saved in PS3 and SEG-Y format. The PC allows buffering, transfer, and storage of the digital seismograms at very high repetition rates.

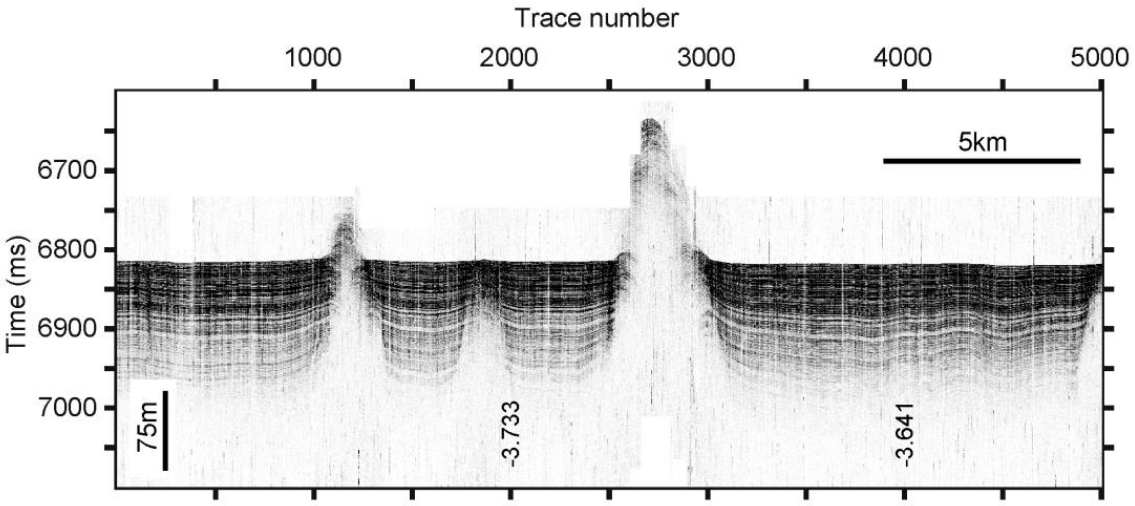

Fig. 5.2: Example of a Parasound® record at the eastern end of the refraction profile #1. Water depth is approx. 5100 m.

5.1.3 Airgun array

The seismic source comprised six G-gun clusters (12 guns) manufactured by Sercel Marine Sources Division (formerly SODERA) and Seismograph Services Inc. configured as two sub-arrays. Six guns were set up in 3 clusters. Each cluster comprises two G-guns of 4x8 l and in the middle either 2x6 l or 2x4 l (see Figs 5.3 and 5.4). The cluster arrangement provides a good primary-to-bubble signal ratio. Operating all twelve guns provides a total volume of 86 l (5250 in^3). The G-guns were operated at 207 bar (3000 psi), towed at 7.5 m depth, and fired at 210 s along the 1100 km long P01 and at 90 s along the 145 km long P02 for OBS/H acquisition. The longer shot spacing used on the first profile was chosen with the expectation to reduce shot induced noise for previous shots, nurturing a much lower noise level in deep ocean environments (e.g., Lizarralde et al., 2004). The airgun array was fired using a Longshot gun controller. MERIAN's internal Junkers compressors provided the air supply. In total, approx. 3700 shots were fired during 8 days of airgun operation.

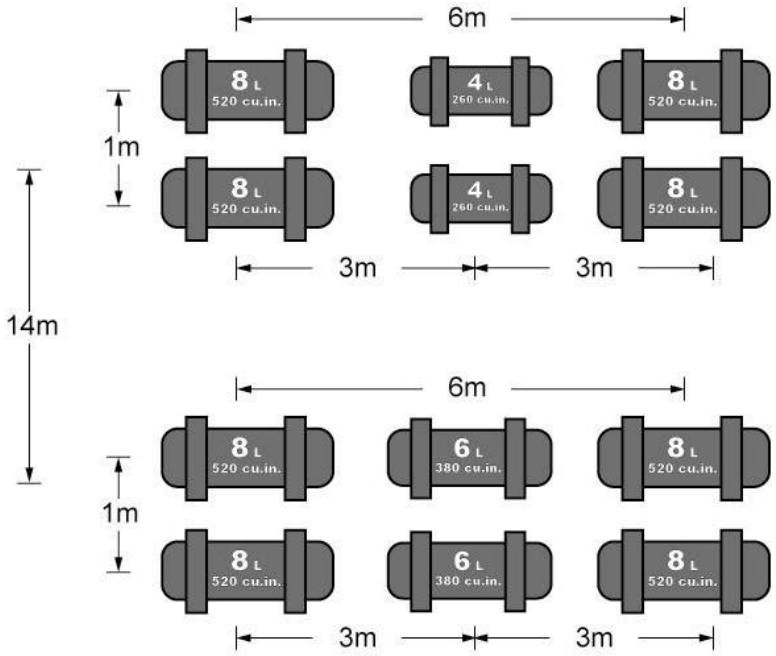

Fig. 5.3 Airgun array configuration.

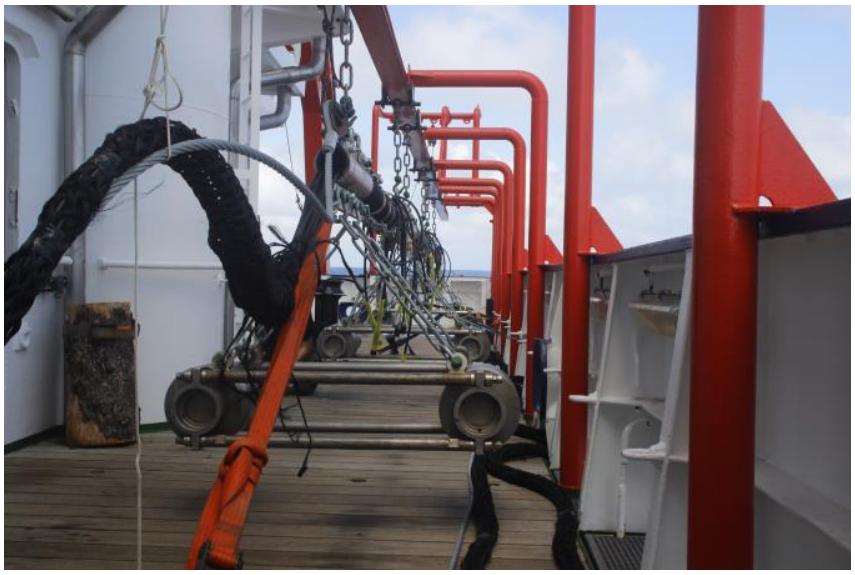

Fig. 5.4 Port airgun array (Photo: Patrick Schröder).

5.1.4 Ocean-bottom seismometer

During the survey different types of ocean-bottom seismographs where deployed. French OBSs where IFREMER's MicrOBS and GEOMAR provided both ocean-bottom hydrophones (OBHs) and OBS.

GEOMAR-OBHs just had a single hydrophone while the OBSs were equipped with a geophone and a

hydrophone. The hydrophone was either an E-2PD hydrophone from OAS Inc. or a HTI-04-PCA/ULF from High Tech Inc.; geophones where 4.5 Hz SM6 B-coils in a pressure protected housing manufactured by KUM GmbH, Kiel, modified from a package designed by Carrack Measurement Technologies. Three different kinds of data loggers were used: (i) a 24-bits data logger developed by Sercel France, (ii) 24-bits GEOLOG data logger developed by Martin Wollatz-Vogt (GEOMAR), and (iii) 32-bits 6D6 data logger from KUM GmbH, Kiel. Depending on the data logger, the sampling rate was set to either 200 or 250 Hz. GEOMAR stations used separate Titanium alloy pressure housings for the acoustic release and seismic data loggers. Buoyancy was provided by syntactic foam and all OBS/H were rated to 6000 m water depth (Fig. 5.5).

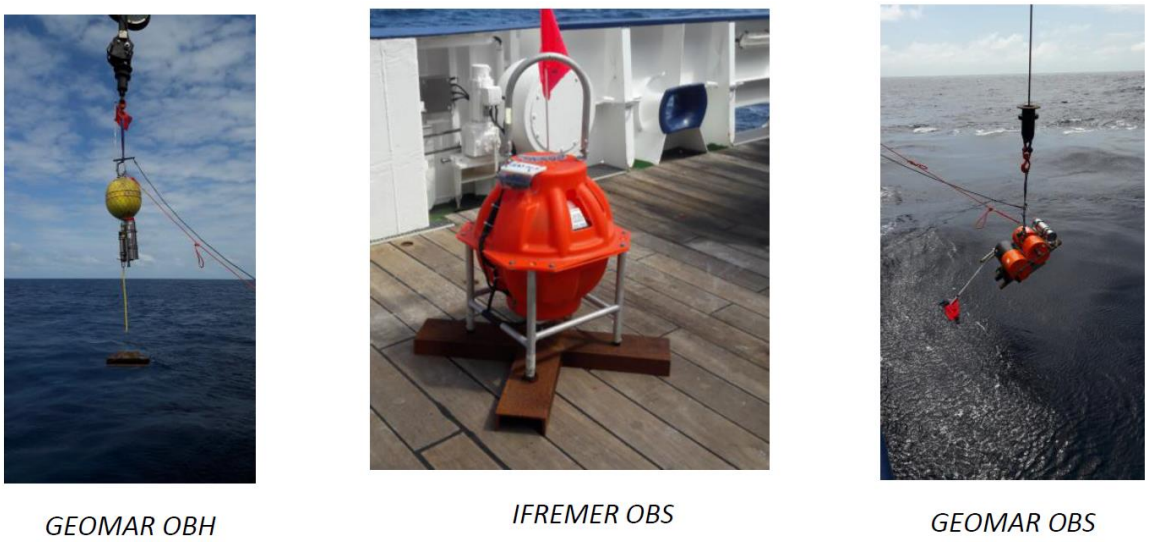

Fig. 5.5: Ocean-Bottom-Hydrophone (left) and Seismometers (middle and right) deployed during the cruise.

IFREMER provided 30 MirOBS with 4 recording channels. Electronics, releaser and batteries were housed in 17-inch glass sphere (Ffig. 5.5). The recording unit consisted of 24-bits Sercel France data logger. The hydrophone was a HTI-90-U from High Tech Inc. and a 4.5 Hz geophone. Active source data were sampled at 250 Hz.

All OBSs, regardless of type or supplier, were synchronized to GPS-derived UTC time before deployment and after recovery and the data corrected for clock drift prior to conversion to SAC and SEG-Y format.

In total, 86 deployments were made throughout the cruise; MirOBSs were deployed at 36 sites, GEOMAR-OBHs at 18 and GEOMAR-OBSs at 31 sites. All deployed OBSs and OBHs were recovered successfully and in general instruments were released after the first acoustic release command was sent. The IFREMER MirOBS had a perfect run; thus, all OBSs recorded data suitable for geophysical data analysis, though some components had poor data. Unfortunately, one GEOLOG recorder and one Sercel data logger operated by GEOMAR failed to record any data (error of flash memory). In addition, six newly manufactured 6D6 recorders had a malfunctioning of the hydrophone channel, providing a poor signal to noise ratio.

Initial onboard seismic data processing suggests that the airgun array provided energy useful for seismic refraction profiling in the frequency range of ~3 to 16 Hz with little energy of far-offset first arrivals >20 Hz (Fig. 5.6). Secondary wide-angle reflections from the crust-

mantle boundary or seismic Moho generally had much lower frequencies of ~3 to 8 Hz. Often, the occurrence of wide-angle reflections was actually best seen by the much lower frequency content of secondary energy occurring at about 15-30 km offset.

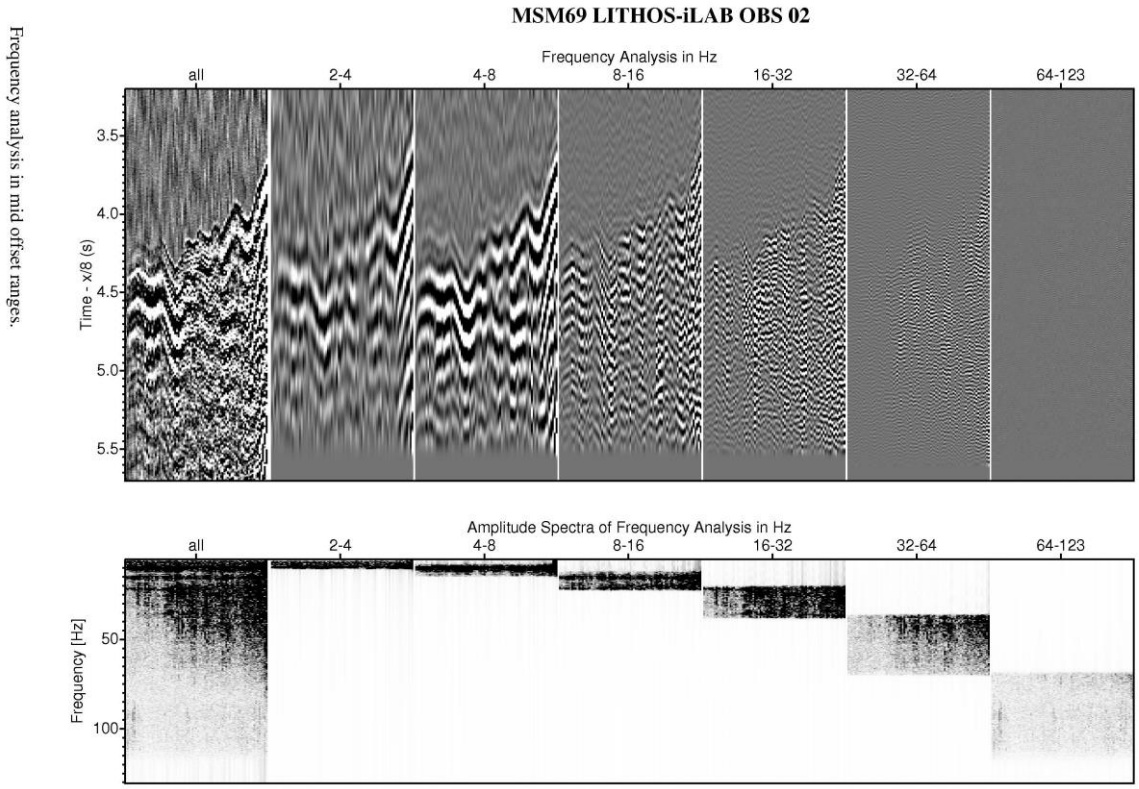

Fig. 5.6: Frequency analysis / content of seismic data.

5.1.5 Marine potential field data

A KSS31M marine gravimeter was installed in the "Gravimeterraum" by the University of Hamburg in Bremerhaven to record the gravity field during MSM69. The instrument, however, stopped operating a few days after the vessel left Bremerhaven and before the scientific party entered the vessel in Mindelo. Unfortunately, the scientific party and the ship's electrician were not able to fix the failure of internal batteries. Therefore, we were not able to acquire any gravity data during the survey.

In addition, it was planned to operate a marine magnetometer along the main survey lines. Unfortunately, the cable of 30 m length of the Bremen magnetometer would have been too short to provide a save operation of the instrument as it would have been towed between the two airgun arrays. Therefore, MSM69 failed to obtain any potential field data.

5.1.6 Marine geothermal measurements

During the cruise we exclusively use the 6 m long Bremen heat flow probe also called Giant Heat Flow Probe (GHF). The mechanically robust heat probe is designed for operation in a pogo-style mode with a wide application range from 6000 m deep sea trenches with mostly soft sediments to the upper continental slope, where sediments are often sandy and difficult to

penetrate. Due to the 6 m length of its temperature sensor string, undisturbed temperature gradients can be determined even where seasonal bottom water temperature variations are superimposed on the undisturbed temperature field close to the sea floor.

The heat probe is constructed in the classical "violin bow" design (Hyndman et al., 1979; Hartmann and Villinger, 2002), with 21 thermistors distributed over an active length of 5.2 m in 0.26 m intervals mounted inside an oil filled hydraulic tube (O.D. 14 mm) which is attached to the strength member (O.D. 130 mm). The sensor tube also contains a heater wire for the generation of high energy heat pulses of typically 800 J/m. This energy pulse is used for in situ thermal conductivity measurements according to the pulsed needle probe method (Lister, 1979). Stainless steel is used for the heat probe, with special high strength non corrosive steel for the strength member and the fins attaching the sensor tube to it. The complete data acquisition unit including power supply (Sea & Sun, Trappenkamp, Germany) is housed in a single 110 mm O.D. x 300 mm long titanium pressure case and mounted inside the probe's weight stand. A second pressure case of the same size houses the batteries for heat pulses. For heat flow stations during this cruise data acquisition unit #488 was used. The signal of the temperature sensors is measured with a resolution of 20-bit at a sample rate of 1 sec, resulting in a final temperature resolution of better than 1 mK at ambient seafloor temperatures. A calibrated PT-100 seawater sensor on top of the weight stand allows to measure the absolute bottom water temperature and to check the calibration of the sensor string in deep water with high accuracy. Inclination and acceleration of the probe is measured to monitor the penetration process into the sediments and potential disturbances during the actual measurement period. During this cruise, the heat probe is deployed using the 18 mm coring wire and operated in a completely autonomous mode with internal data storage and automated heat pulses.

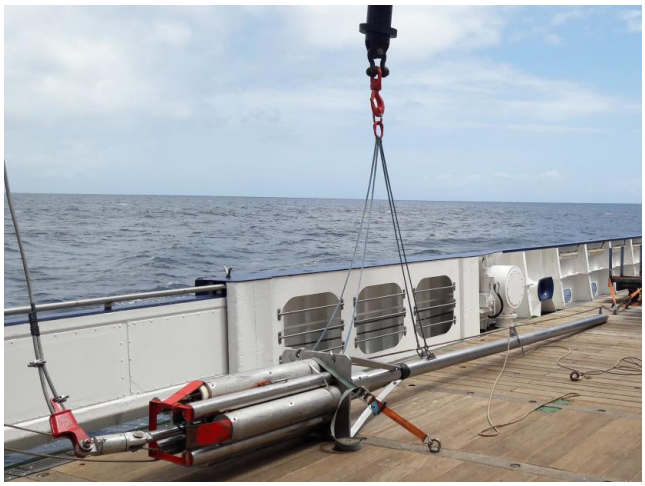

Fig. 5.7: Violin-bow design heat probe

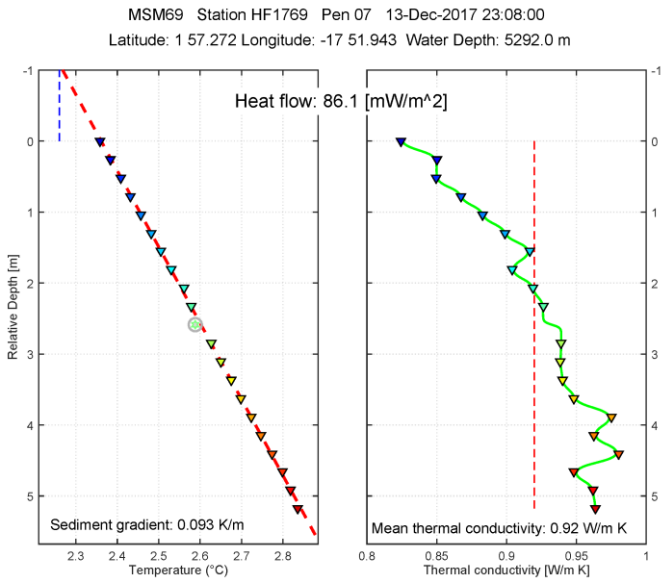

Fig. 5.8: Heat flow estimate from geothermal measurements

Winch speed for penetration of the heat probe is 0.8 to 1.0 m/s for maximum penetration into the sediment. Time to equilibrate to in situ temperatures is assumed to be 7 to 8 minutes; time for heat pulse decay observation takes another 8 minutes. The mean duration of one measurement, including transit of

about 1 km between waypoints, is about 1 - 1.5 h per single point of measurement. The heat probe position at depth could not be monitored as the new Sonardyne USBL system on board of MARIA S. MERIAN is not yet calibrated.

Penetration of the heat probe into the upper meters of the soft sediments generates a thermal disturbance due to frictional heating, and in addition the sensor string has to come into thermal equilibrium with the sediments. This means that the probe stays in the sediment for about 7 to 8 minutes; however it will not have equilibrated at the end of this time. Therefore the temperature decay has to be fitted to a theoretical decay model (Villinger and Davis, 1987; Hartmann and Villinger, 2002). In situ thermal conductivity is measured with the heat pulse method (Lister, 1979) where the sensor string is heated up for typically 20 to 30 s and the thermal conductivity is derived from the 8 minute long temperature decay. Fig. 5.3 shows two examples of heat flow measurements made during MSM69.

During MSM69 in total 105 geothermal gradient measurements were conducted, providing a unique modern heat flow dataset from the equatorial Atlantic Ocean.

5.2 First scientific results from shipboard data

During the cruise, we acquired seismic wide-angle seismic refraction data along the main profile P01, surveying lithosphere formed at the Mid-Atlantic Ridge and the temporal variability of the spreading process expressed in terms of crustal thickness and crustal velocity structure. Further, excellent weather and excellent performance of instrumentation, scientific party and crew provided one day of slack time that was used to survey a short second profile, P02, sampling the structure of the St. Paul fracture zone during the transit back to Mindelo. In addition, heat flow data were obtained in all survey areas, characterizing the thermal state and heat loss of oceanic lithosphere in the equatorial Atlantic.

5.2.1 Seismic profile P01 – 1100 km long lithospheric flow-line transect

The profile P01 runs from 12.8°W/2.8°S,for 75 km on the South American plate (see Fig. 5.10), crosses the Mid-Atlantic Ridge and terminates at 3.2°W/0.7°S, covering zero-age to approximately 50 Myr old lithosphere of the African plate. The seismic refraction and wide-

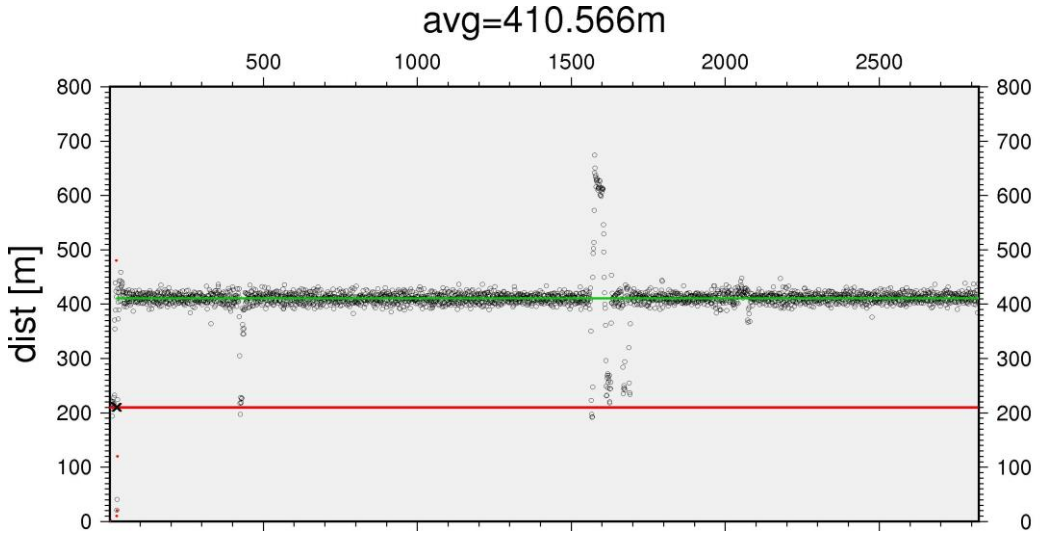

Fig. 5.9: Seismic shot statistics of P01

angle transect was covered with 71 Ocean-Bottom-Seismometers and hydrophones (OBH01 to OBS72) spaced at 10 to 20 km intervals. The line coincides with iLAB-MCS profile C-E (see Fig. 3.1). The profile was shot at an increased interval of 210 s (Fig. 5.9) to decrease the shot-induced-level (e.g., Lizarralde et al., 2004), improving signal-noise-ratio. A total of 2735 shots were fired in 6 days and 18 hours. The average vessel speed was 3.8 knots and the shot spacing was around 410 m, varying by ±20 m.

Two OBSs along the profile failed to record data (OBS36 and OBS61). One of the OBS had a malfunctioning of a new generation of data logger and the other had a disc writing error after some hours before shooting started. In addition, OBH01, OBS17, OBS21, OBH31, OBS34 and OBH67 recorded rather poor data. All data logger were of the new 6D6 type. For OBH67 we could establish that the poor signal-noise ratio was caused by the hydrophone. All others had a poor dynamic range at frequencies of >1 Hz. These data loggers had a serial number of 61607125 or greater. However, 14 6D6 data loggers with smaller serial numbers provided an excellent performance.

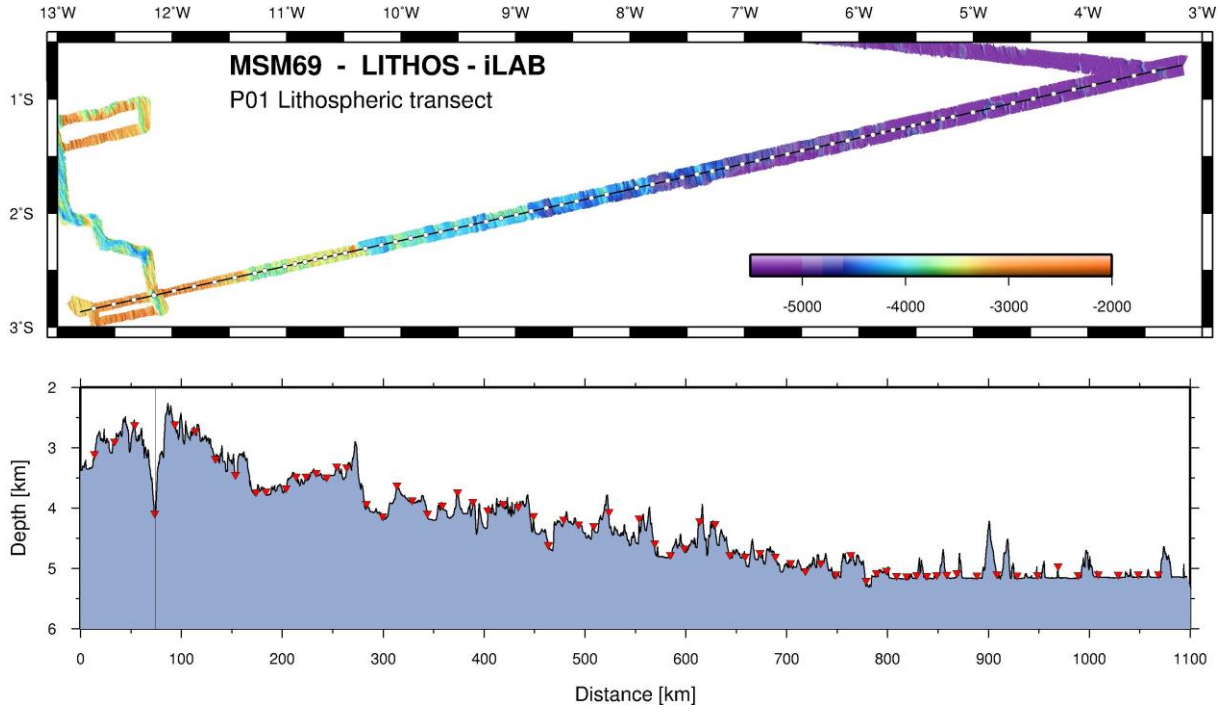

Fig. 5.10: EM122 bathymetry along the main transect P01

In general, data quality along the profile was very good, providing offsets of 80 to 150 km (Figs 5.11 to 5.20) at most seismic stations. At some locations scattering from relief of several hundreds of meters affected the wavefield. However, even OBH68 within the median valley and hence a relief of about 2 km had excellent data. Most stations indicated clear crustal phases (Pg), a wide-angle reflections from the crust-mantle boundary (PmP), and a upper mantle refraction branch (Pn). PmP is generally of lower frequencies than the refracted phases and can therefore be identified quite clearly in about 70% of the OBS records.

An interesting observation comes from the seafloor topography, providing almost flat seafloor at ~700 km to 1000 km distant from the ridge axis (profile-km 800 to 1100 km – see Fig. 5.10). In general, we would expect a strong relationship to lithospheric cooling, promoting a

subsidence of ~360 m per 1 Mio. years. A first inspection of data suggests that the feature is not related to sedimentary blanketing. Thus, even basement depth support rather constant depth.

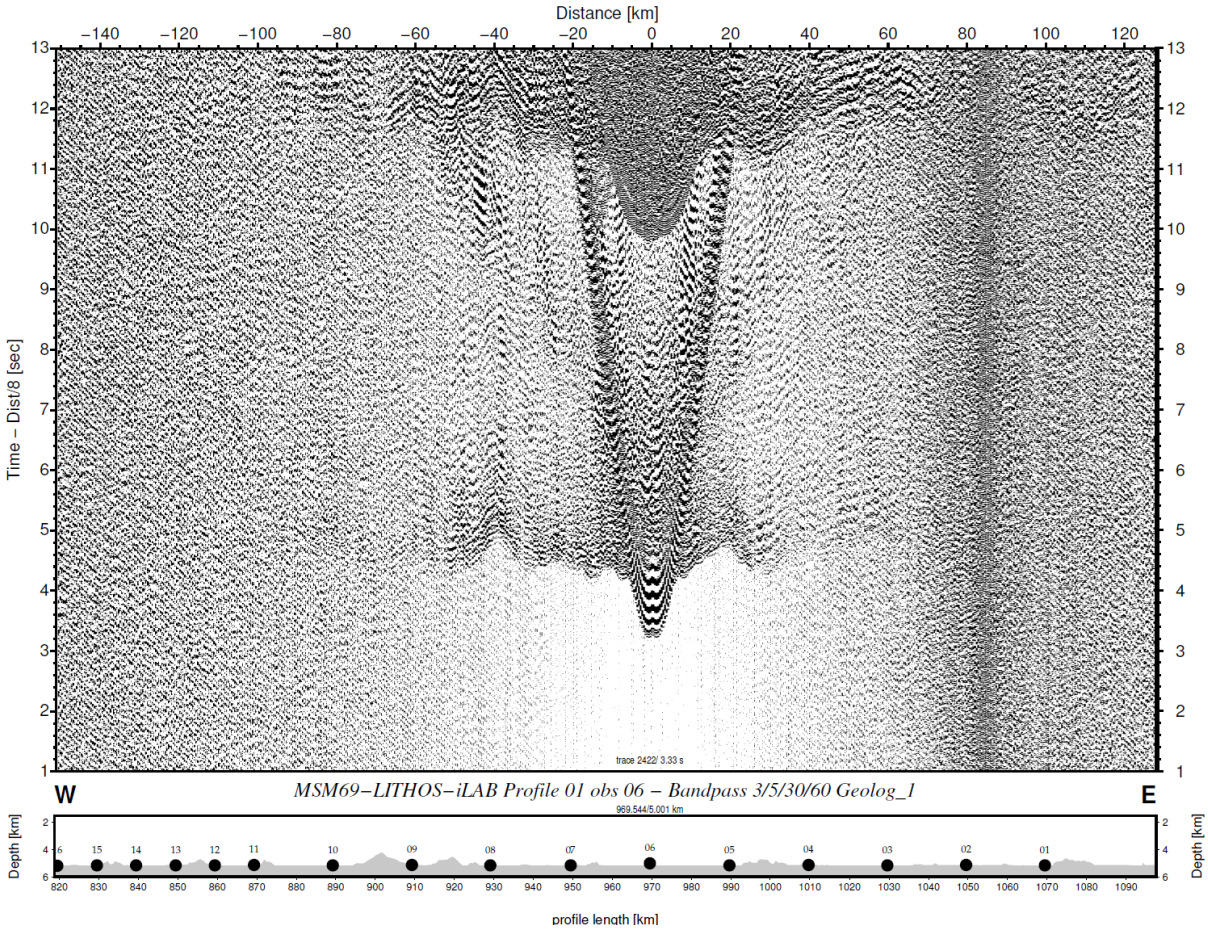

Fig. 5.11: Record section (hydrophone) of OBS06

The record sections support that some of the lateral changes of the seafloor topography are matched by changes in seismic structure. Thus, OBS/H with number of 01 to ~20 show different pattern than OBS/H farther west. For example, OBS06, OBS10 and the eastern branch of OBS18 provided different characteristics than the western branch of OBS18, or OBS26 or OBS32. OBS located farther west than OBS30 have generally the best developed PmP phases – like OBS38, OBH48 or OBS56. Approaching the ridge axis, OBS/H generally provide shorter offsets, but still show clear crustal and mantle arrivals, including PmP wide-angle reflections, like OBH65 and OBH68 within the median valley of the Mid-Atlantic Ridge.

Initial interpretation from the offset range of PmP arrivals suggest that crust will be in the order of 6 km +/- 1 km. Further, fast apparent velocities of ~8 km/s imply that the upper mantle will not be profoundly hydrated. This interpretation is supported by fast Sn apparent velocity of about 4.6 km/s. S-waves are generally very well developed and often show larger offsets than P-wave, but have not been studied in any detail.

Unfortunately, first inspection of the data did not indicate any prominent wide-angle arrivals from greater depth either representing layering of the lithosphere or the base of the lithosphere (LAB) itself. However, a more careful inspection of data will be conducted in the future.

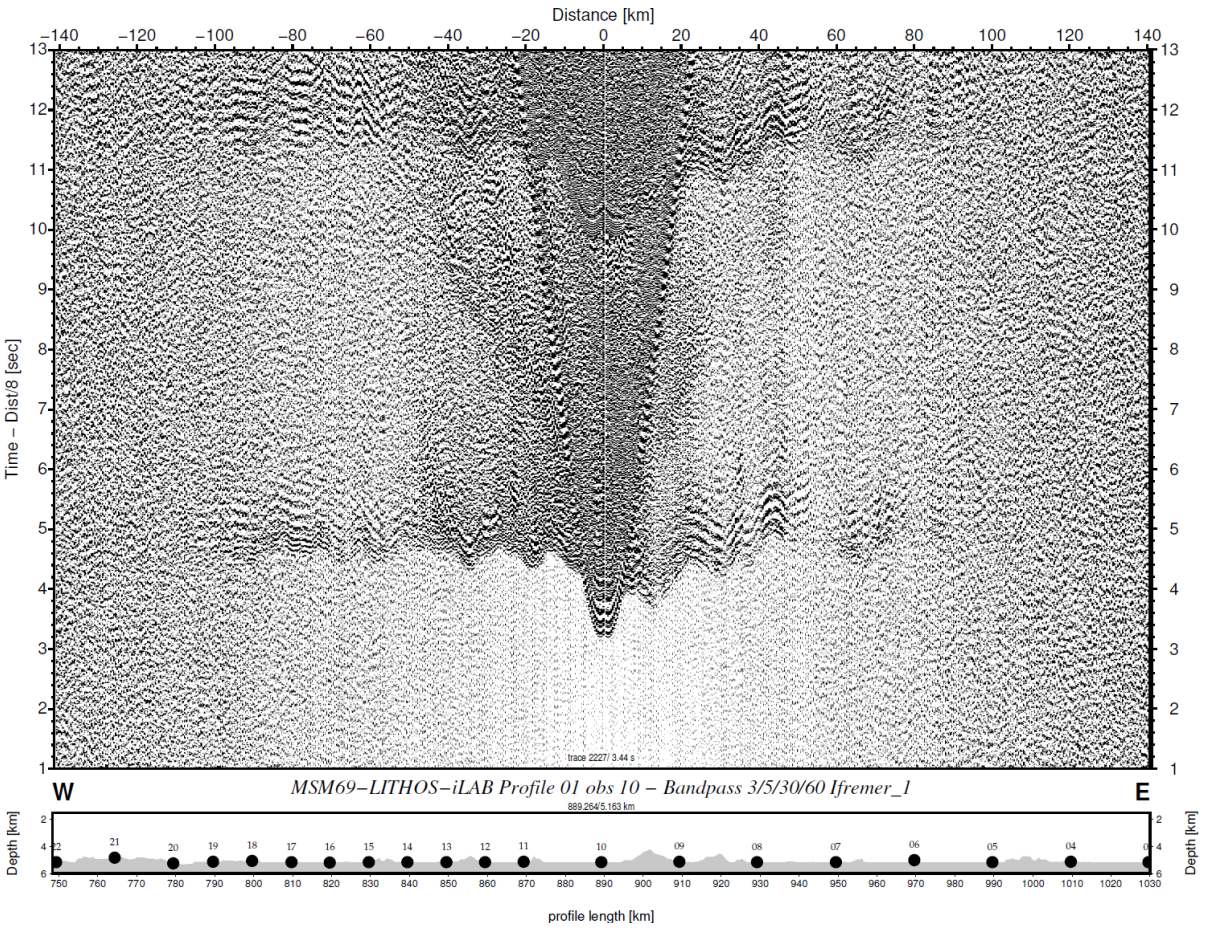

Fig. 5.12: Record section (hydrophone) of OBS10

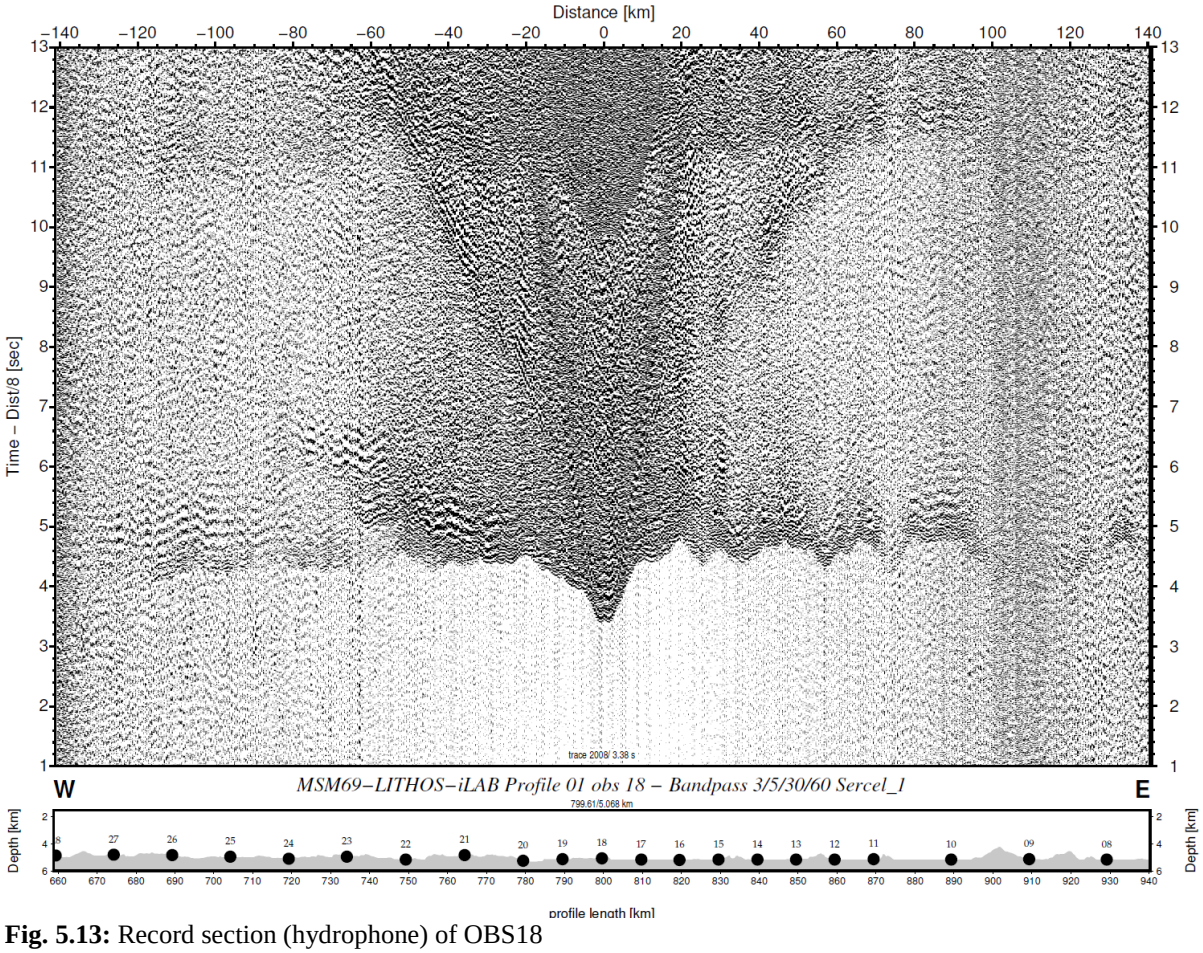

Fig. 5.13: Record section (hydrophone) of OBS18

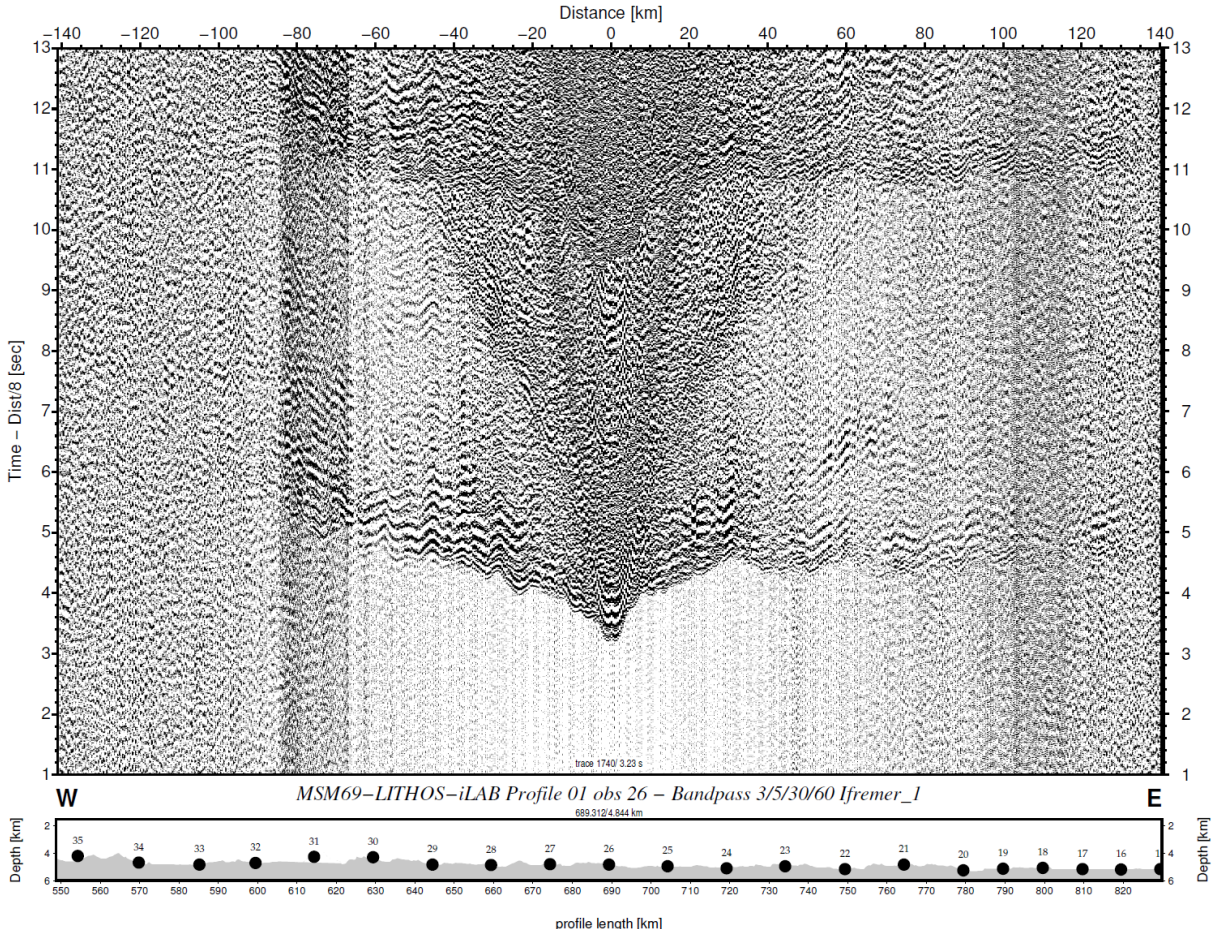

Fig. 5.14: Record section (hydrophone) of OBS26

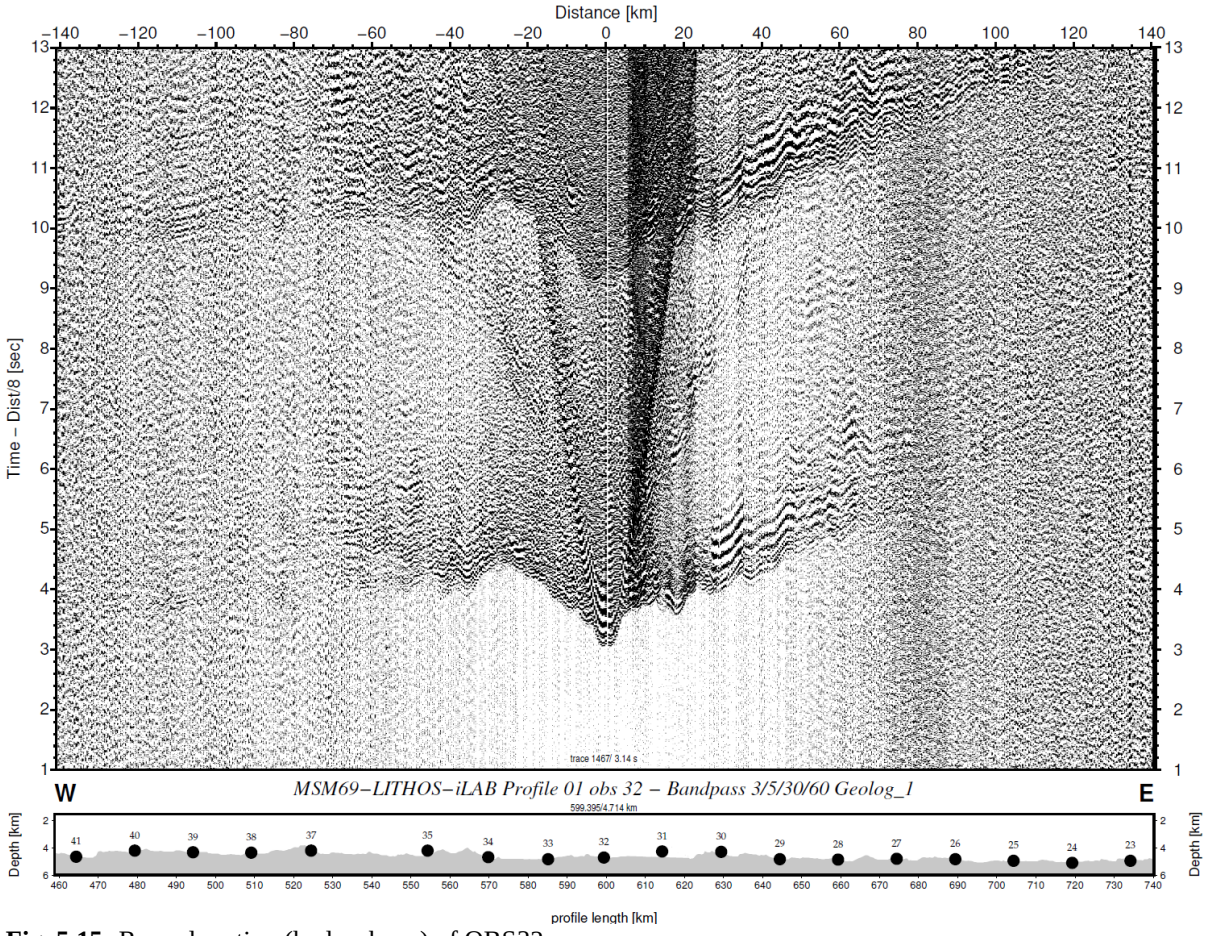

Fig. 5.15: Record section (hydrophone) of OBS32

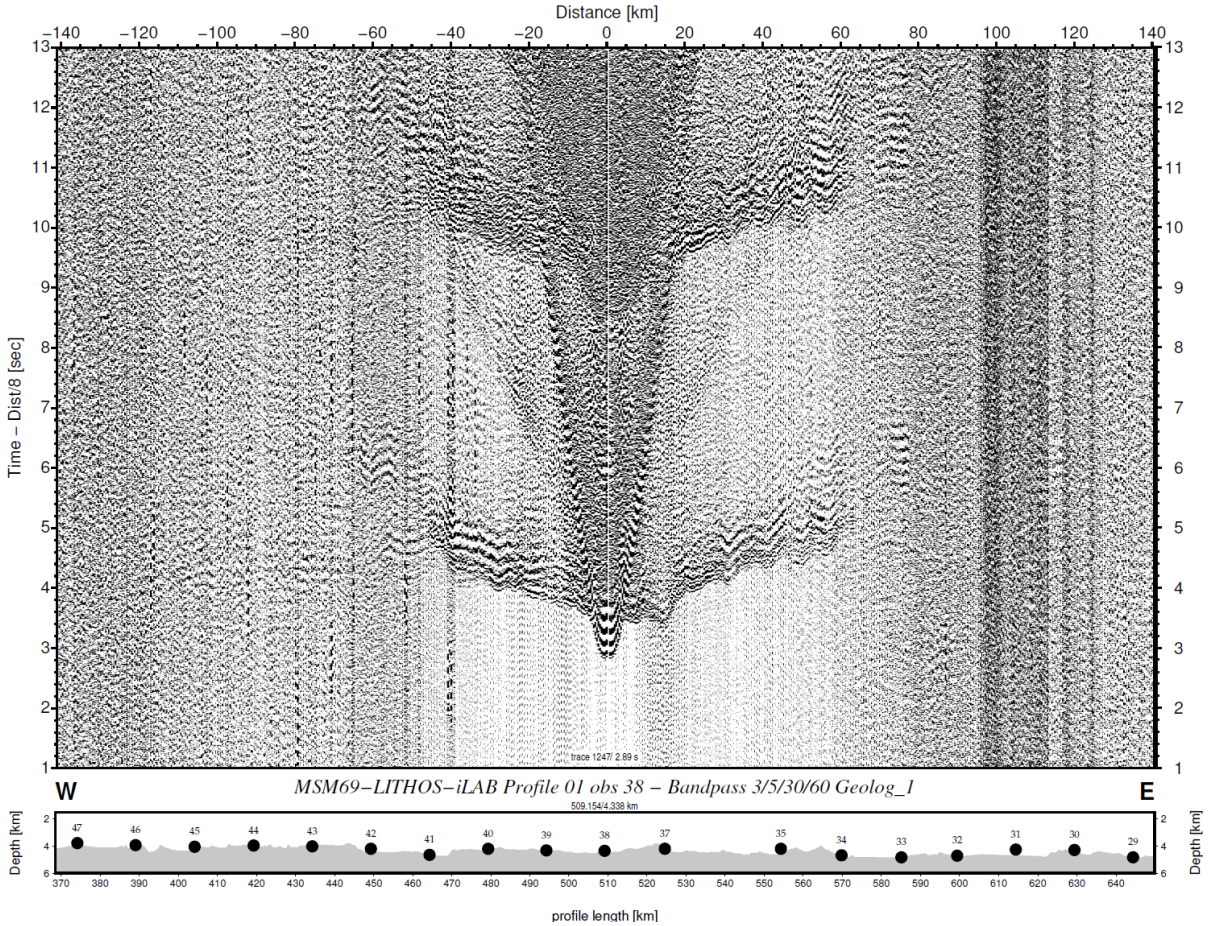

Fig. 5.16: Record section (hydrophone) of OBS38

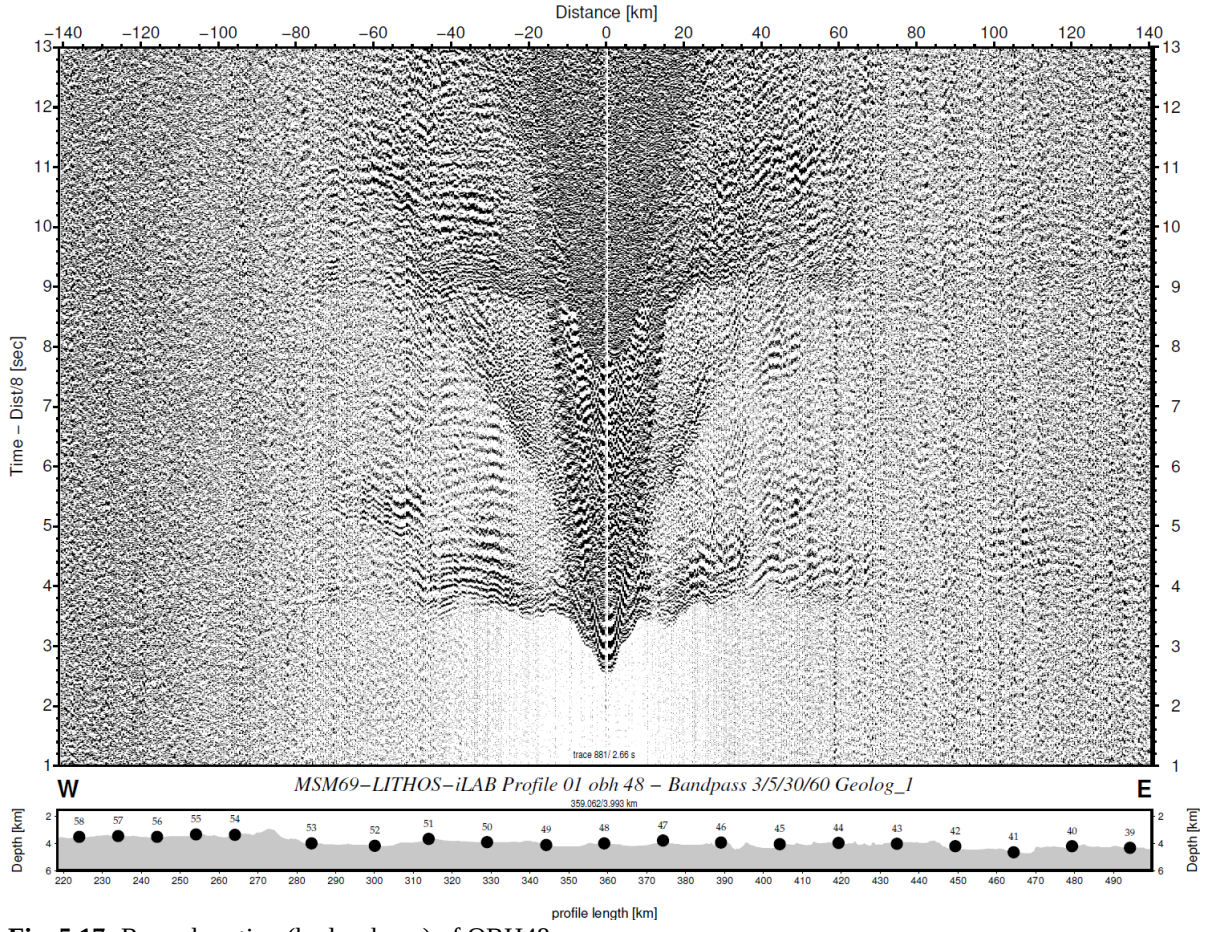

Fig. 5.17: Record section (hydrophone) of OBH48

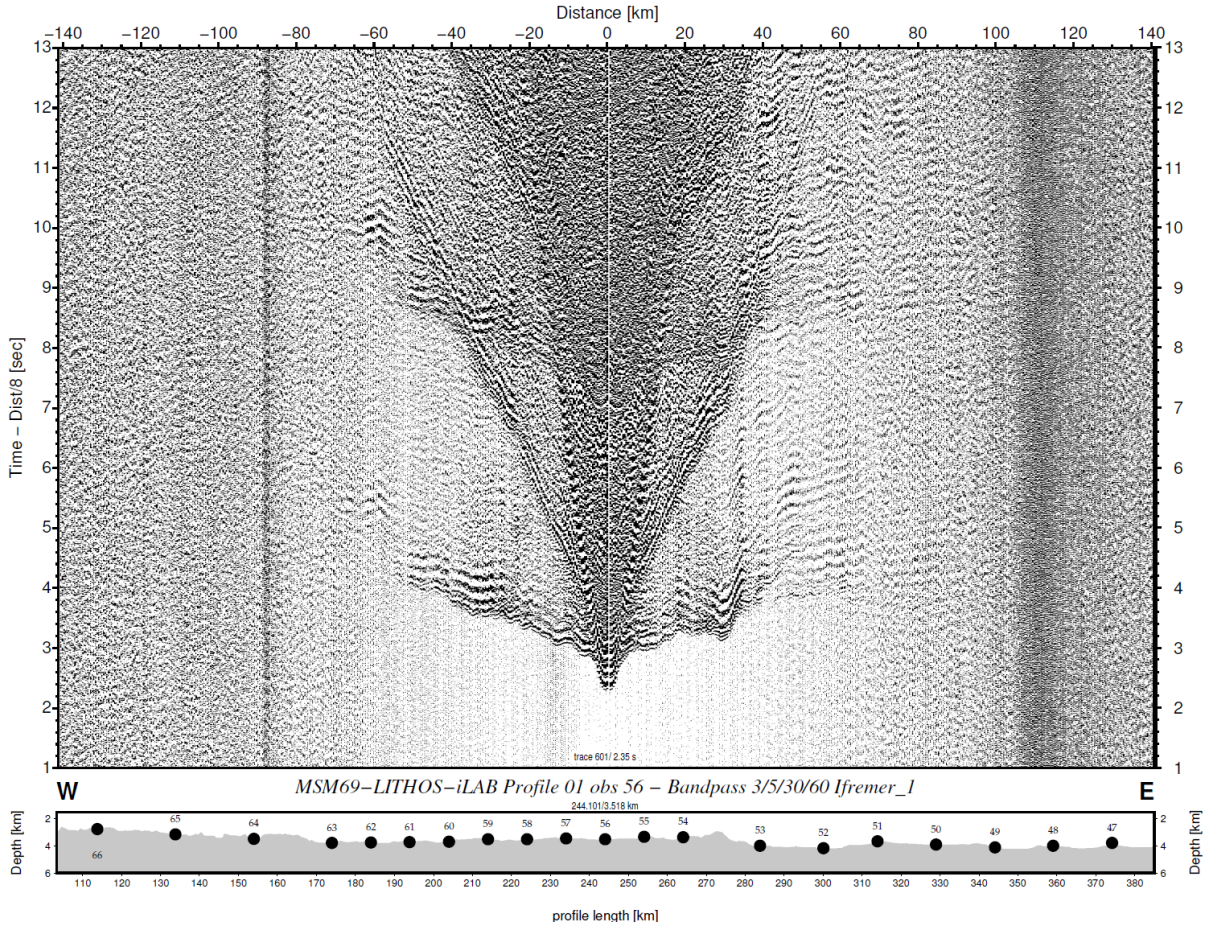

Fig. 5.18: Record section (hydrophone) of OBS56

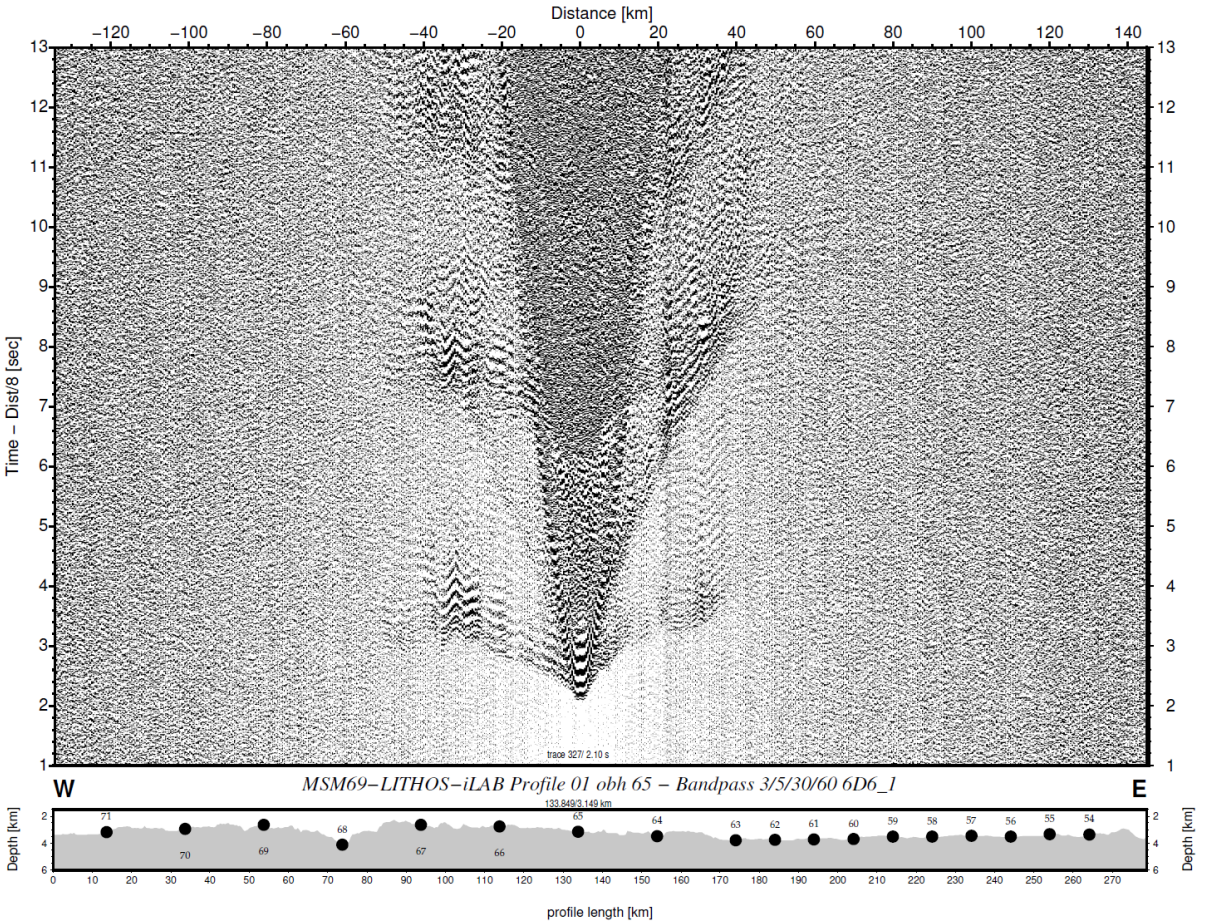

Fig. 5.19: Record section (hydrophone) of OBH65

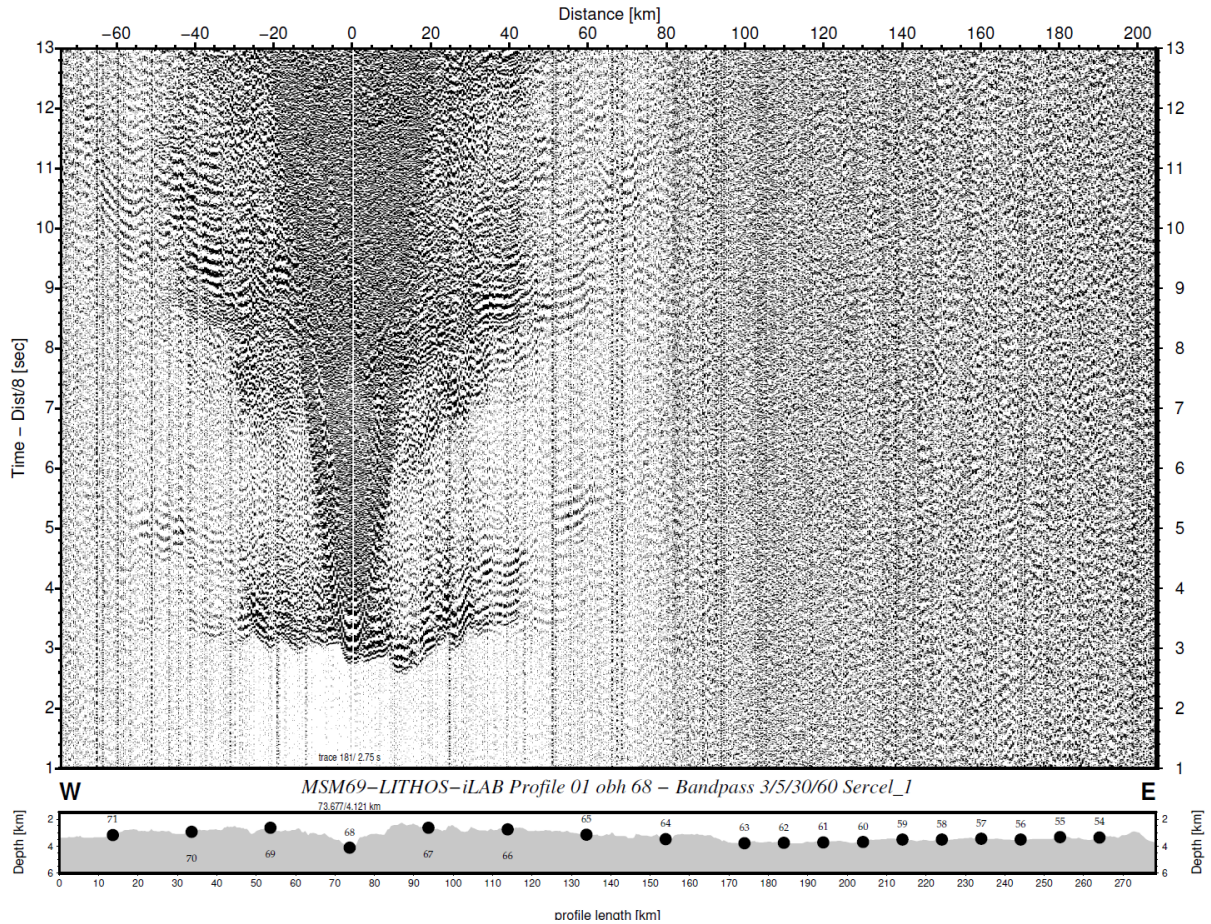

Fig. 5.20: Record section (hydrophone) of OBH68

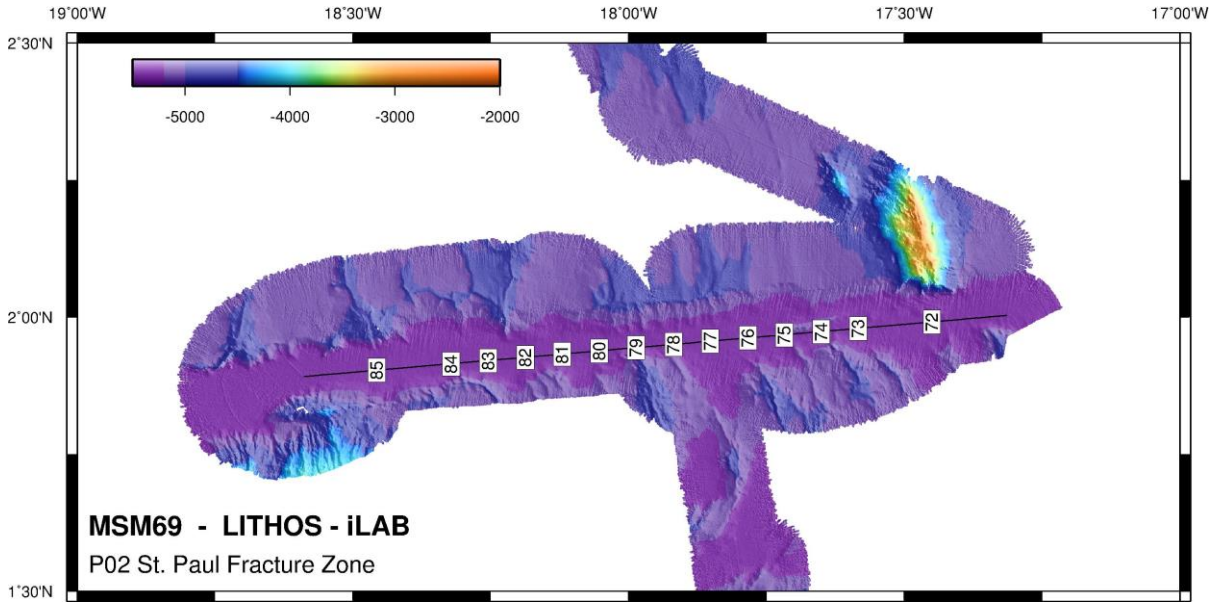

Fig. 5.21: EM122 bathymetry along seismic profile P02

5.2.2 Seismic profile P02 – sampling the lithosphere along the St. Paul Fracture Zone

The second seismic profile P02 was conducted within the valley of the St. Paul Fracture Zone, crossing the northernmost iLAB MCS profile of Mehouach and Singh (2017)(see Fig. 3.1

and 3.6). Along the seismic refraction and wide-angle profile 12 Ocean-Bottom-Seismometers (OBS73 to OBS84) and two Ocean-Bottom-Hydrophones (OBH72 to OBH85) were deployed at 7.5 to 15 km intervals and at an average water depth of ~5500 m (Fig. 5.21). The profile was shot at an interval of 90 s and a total of 895 shots were fired at an average vessel speed was 3.5 knots, resulting into an average shot spacing of 165 m (Fig. 5.22). The flat bathymetric obtained along the fracture zone suggested that the valley is covered with some hundreds of meters of sediments, which is supported by MCS data (Fig. 3.6).

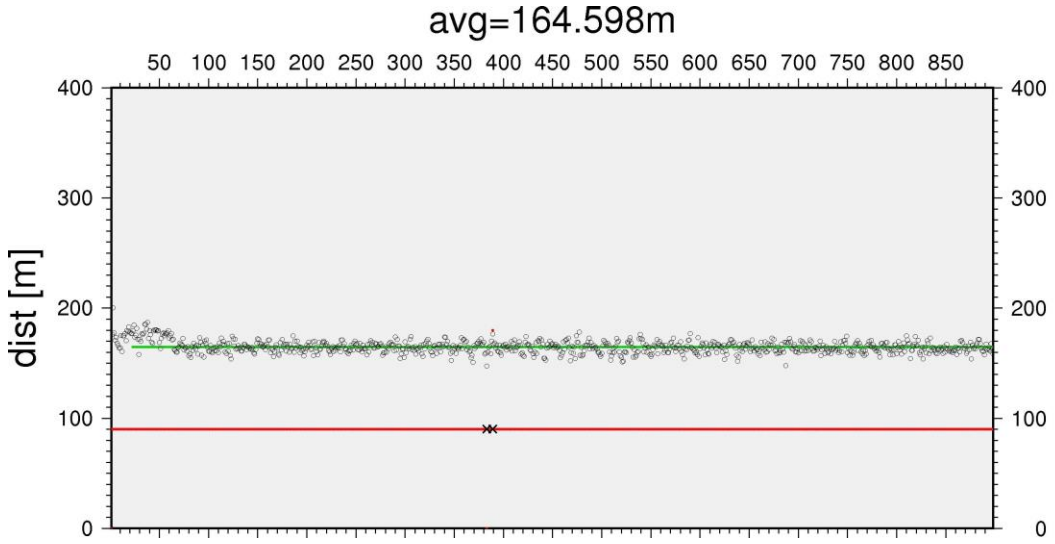

Fig. 5.22: Seismic shot statistics of P02

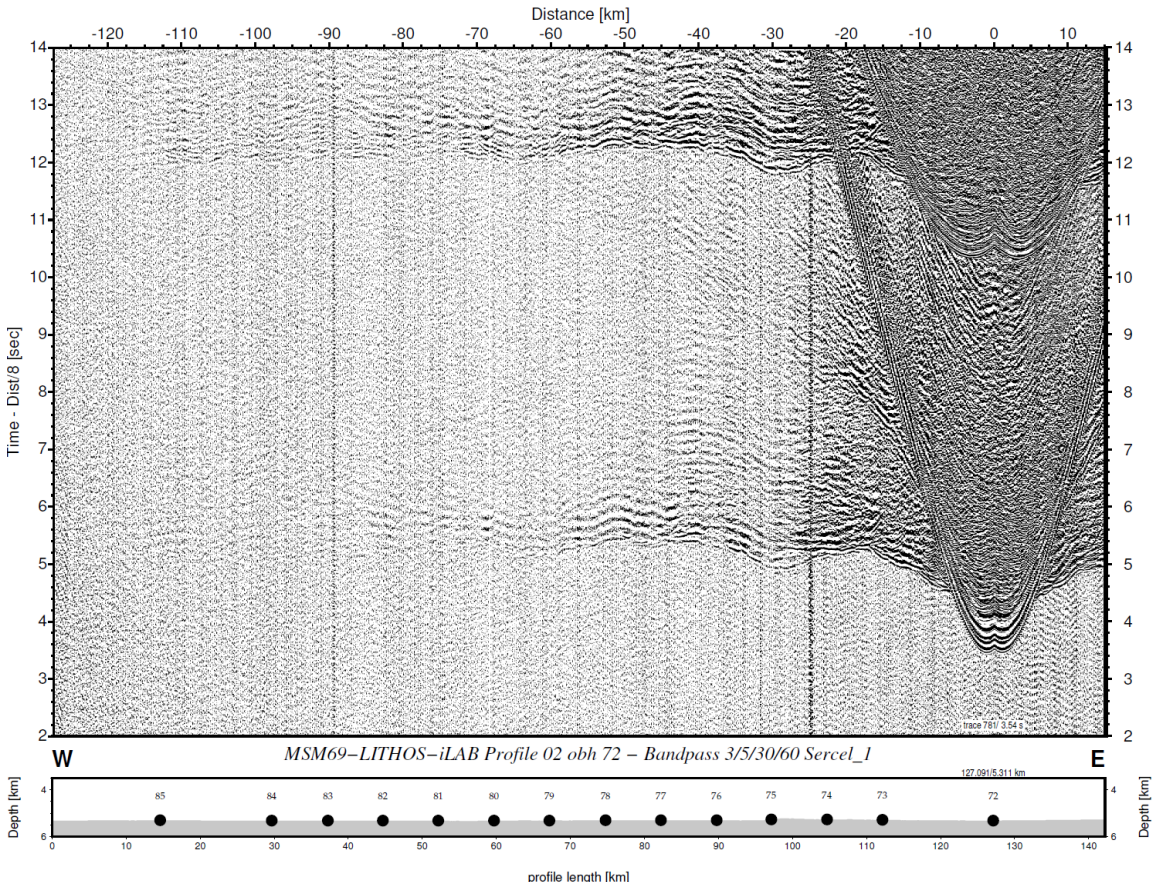

Fig. 5.23: Record section (hydrophone) of OBH72

The data quality along the profile is very good, providing offsets over the entire length of the profile (Figs 5.23 and 5.24). Some scattering in the record sections suggests that the basement is rather rough. All stations indicate clear crustal phases (Pg) and an upper mantle refraction branch (Pn). Further, most stations provide a wide-angle reflection from the crust-mantle boundary (PmP). The short offset of ~15 to 20 km of PmP indicates thin crust of ~4-5 km. A mantle velocity of ~ 8 km/s suggests that the mantle along the fracture zone is rather dry and that serpentinization is not an important issue.

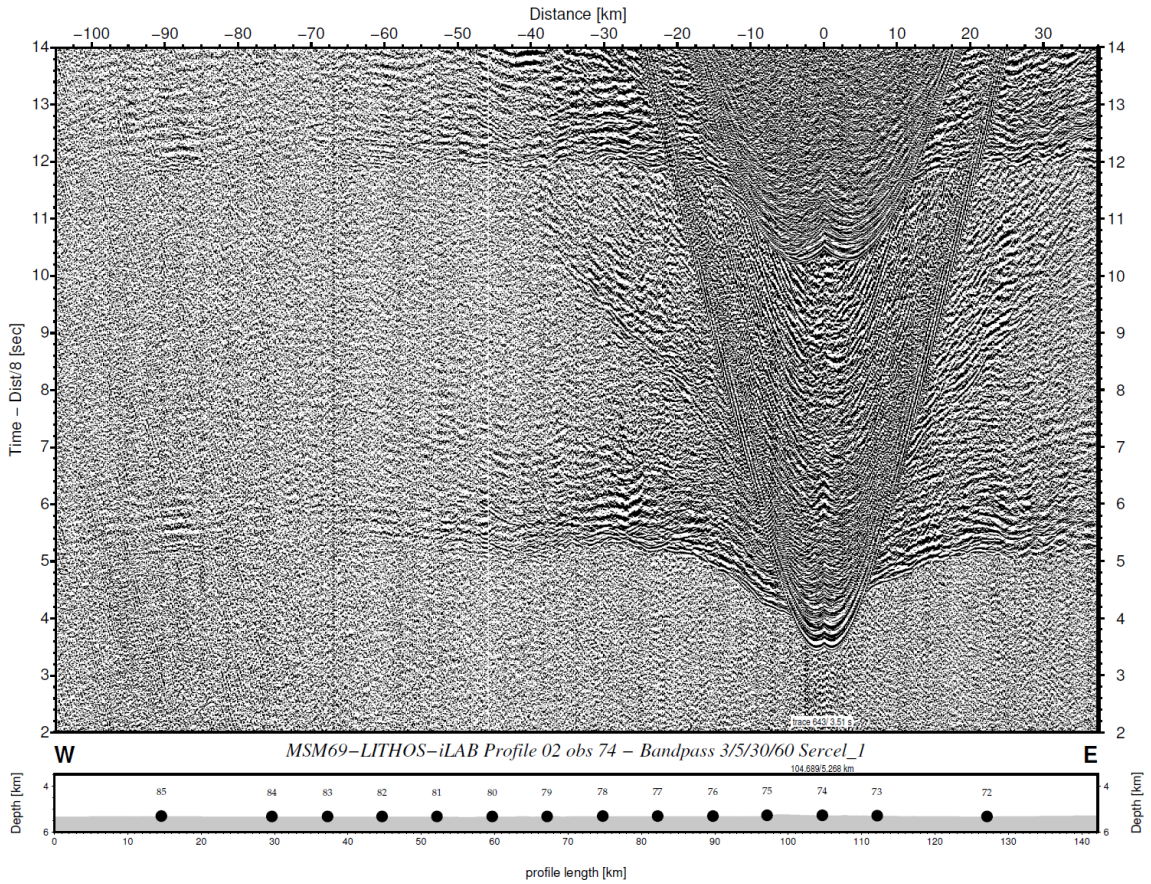

Fig. 5.24: Record section (hydrophone) of OBS74

5.2.3 Heat flow surveying – first results

One of the scientific goals of the cruise was to map heat flow along the iLAB MCS/refraction profile(s) and compare the results to the published heat flow vs. age models. Heat flow values will be also used as one of the constraints when interpreting properties of Layer 2A mapped with the MCS long streamer system.

We made 75 measurements along the MCS profile C-E starting at a water depth of approx. 5130 m at the eastern end of the profile and ending at a water depth approx. 3200 m at the western end. Separation of the measurements was in most cases 1000 m. Sediment thickness varied between a few tens of meters to several hundreds of meters in small basins. Details will be available once the high-frequency part of the MCS data is processed. Depth penetration of Parasound was in most cases not sufficient to determine basement depth. Also thin sediment cover is probably frequent on slopes where no good Parasound record could be obtained. There was only one location where the probe could not penetrate and fell over. In situ thermal

conductivity measurements show a fairly uniform thermal conductivity of the sediments varying between 0.8 and 1 W/mK. Where no in situ thermal conductivity was measured a constant value

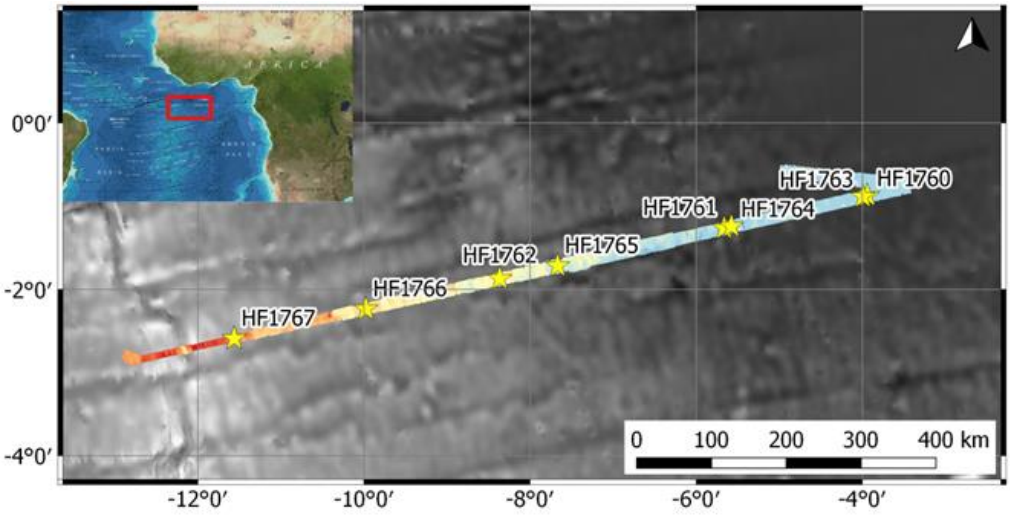

Fig. 5.25: Heat flow stations along seismic transect P01. Each station consists from 7 to 10 individual measurement points. The measured swath bathymetry is superimposed of the global satellite bathymetry.

of 0.9 W/mK was assumed. Due to the lack of a USBL system, all positions are ship's positions during the measurement. We have to assume that the probe was about 100 to 300 west of the ship's location as we surveyed from west to east due to prevailing wind and current conditions.

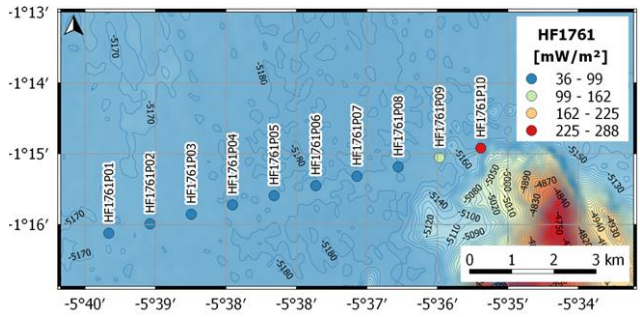

Fig. 5.26: Example of a heat flow station – HF1761.

Locations of heat flow stations HF1760, HF1761 and HF1762 were chosen based on the available MCS data but without prior knowledge of the detailed swath bathymetry. These measurements were done during the OBS deployment phase whenever there was a convenient time slot available. After shooting the refraction profile, Parasound and swath bathymetry obtained along P01 were used for picking the locations of stations HF1763 to HF1767. All locations are shown in Fig. 5.25 and details can be found in the Appendix. An example of a detailed location map of each station can be found in Fig. 5.26 and the corresponding Parasound profile in Figure 5.27. All other detailed maps can be found in the Appendix.

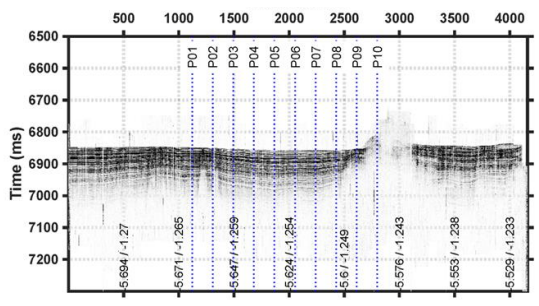

Fig. 5.27: Parasound profile along HF1761.

Fig. 5.28 shows measured heat flow vs crustal age in comparison with the lithosphere conductive cooling curve (Hasterok, 2013). Crustal age was determined based on the age grid provided by Müller et al. (2008). As expected most of the values on crust younger than 40 Ma show a considerable scatter, however, the median of the values at each location is well below the predicted conductive cooling model. Latest compilations of world-wide published heat flow (Hasterok, 2013) show for this age range values below and above the cooling curve. In our study

all but a few values are very low which may mean that the segment we mapped is cooled very efficiently by hydrothermal circulation. In only one case (Fig. 5.26), we found an extremely high heat flow value which may point to local discharge at the foot of a north-dipping basement ridge. The global heat flow data base shows only two values in the segment we were working in which are in the same range as our values. However, one has to keep in mind that almost all heat flow values of this time period were based on temperature measurements at three different depths so their reliability is in cases questionable. If one filters the global data set and plots only values below 30 mW/m^2 very few published values between the equator and 10°S are as low as the ones in our segment. Ongoing analysis of layer 2A by the research group of S. Singh (IPGP) will help to understand much better the mapped heat flow variations. Additional figures presenting measurements and Parasound are shown in the Supplementary material; Figs. A1-A7.

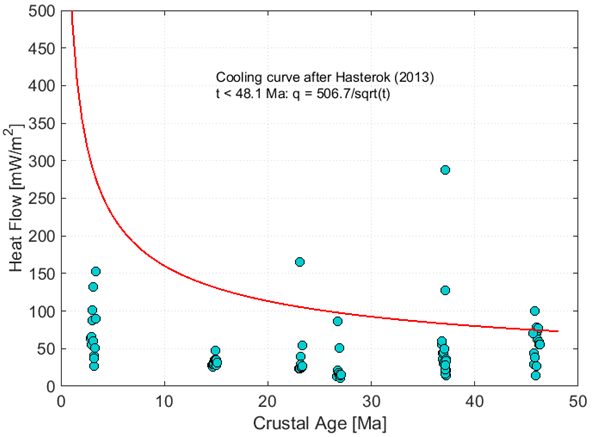

Fig. 5.28: Heat flow vs age along seismic transect P01 in comparison with expected heat flow (Hasterok, 2013) of a conductively cooling lithosphere.

The second part of the heat flow survey was concentrated on the Saint Paul Fracture Zone, along the main iLAB reflection seismic profile (Fig. 5.29). 40 Ma old oceanic crust south of St. Paul FZ meets 70 Ma year old crust north of St. Paul FZ. The question is if the fracture zone itself has a thermal signal due to the way it was created and if the heat flow south and north of it reflects the expected values for 40 and 70 Ma old oceanic crust. Due to time constraints heat flow profiles were planned on the basis of the existing iLAB MCS line across the fracture zone (Mehouachi and Singh, 2017) and Parasound and multibeam surveys were run afterwards.

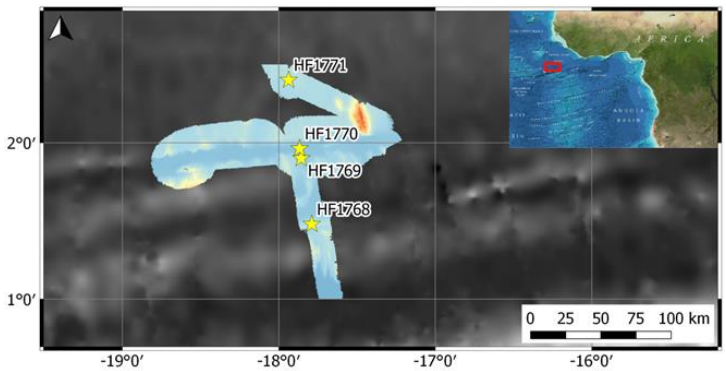

Fig. 5.29: Location of the heat flow stations across St. Paul Fracture Zone.

In situ thermal conductivity measurements show a fairly uniform thermal conductivity of the sediments varying between 0.8 and 1 W/mK. Where no in situ thermal conductivity was measured a constant value of 0.9 W/mK was assumed. Again, due to the lack of a USBL system, locations of penetrations are approximated by the ship's positions during the measurement. Thus, we have to assume that the probe was about 100 to 300 south of the ship's location as we surveyed from south to north due to prevailing wind and current conditions. Results of heat flow measurements and Parasound are shown in the Supplementary material; Figs A8-A11.

Heat flow increases on profile HF1768 systematically towards north with values in the range of 60 to 80 mW/m^2 which is close to the expected value of a conductively cooling lithosphere. Right on the FZ values decrease versus North and show considerable scatter

between 80 and 90 mW/m^2. However, no systematic variation of heat flow with changing sediment thickness can be observed at first sight. The scatter of the values at the FZ will become less after the final processing of the data. Parasound profile at HF1770 shows a large slump at the deepest part of the FZ. Sedimentary structures at the slope of profile HF1770 are again poorly imaged. Seismic data will allow modeling the effect of varying basement topography on heat flow. The three values of HF1771 are around 70 mW/m^2 are somewhat high in comparison with expected heat flow at 40 Ma year of crust but maybe the location was still too close to the FZ. We have no Parasound record at profile HF1771. For all profiles temperatures at the sediment-basement interface will be calculated to assess the thermal state of the upper boundary of Layer 2A.

6 Station lists

MSM69_1-1	CTD/Rosette	2017-11-17T08:32:00	7.31754	-18.27496	-4831					max depth/on ground
MSM69_2-1	CTD/Rosette	2017-11-18T08:42:00	3.42106	-15.59416	-4850					max depth/on ground
MSM69_2-2	Ocean bottom seismometer	2017-11-18T10:58:00	3.42107	-15.59415	-1000	2017-11-18T11:19:00	3.42105	-15.59416		information
MSM69_3-1	Ocean bottom seismometer	2017-11-21T08:38:00	-0.75470	-3.42330	-5145	2017-12-02T12:21:00	-0.75408	-3.42886		OBS deployed
MSM69_4-1	Ocean bottom seismometer	2017-11-21T09:36:00	-0.79476	-3.59884	-5132	2017-12-02T14:02:00	-0.79390	-3.60981		OBS deployed
MSM69_5-1	Ocean bottom seismometer	2017-11-21T10:37:00	-0.83424	-3.77417	-5134	2017-12-02T15:50:00	-0.83428	-3.77857		OBS deployed
MSM69_6-1	Heat-Flow probe	2017-11-21T11:45:00	-0.87230	-3.94027	-5132	2017-11-21T23:07:00	-0.85830	-3.87880	-5141.1	in the water
MSM69_7-1	Ocean bottom seismometer	2017-11-22T00:10:00	-0.87425	-3.94950	-5206	2017-12-02T17:43:00	-0.87366	-3.95472		OBS deployed
MSM69_8-1	Ocean bottom seismometer	2017-11-22T01:10:00	-0.91458	-4.12373	-5159	2017-12-03T07:14:00	-0.91369	-4.13027		OBS deployed
MSM69_9-1	Ocean bottom seismometer	2017-11-22T02:11:00	-0.95383	-4.29915	-5062	2017-12-03T09:09:00	-0.95311	-4.30443		OBS deployed
MSM69_10-1	Ocean bottom seismometer	2017-11-22T03:09:00	-0.99371	-4.47493	-5151	2017-12-03T11:16:00	-0.99320	-4.48351		OBS deployed
MSM69_11-1	Ocean bottom seismometer	2017-11-22T04:06:00	-1.03340	-4.65230	-5164	2017-12-03T13:15:00	-1.03172	-4.65963		OBS deployed
MSM69_12-1	Ocean bottom seismometer	2017-11-22T05:06:00	-1.07320	-4.82637	-5145	2017-12-03T15:41:00	-1.07182	-4.83358		OBS deployed
MSM69_13-1	Ocean bottom seismometer	2017-11-22T06:06:00	-1.11267	-5.00205	-5169	2017-12-03T17:59:00	-1.11253	-5.00857		OBS deployed
MSM69_14-1	Ocean bottom seismometer	2017-11-22T07:05:00	-1.15277	-5.17742	-5118	2017-12-03T20:24:00	-1.15337	-5.18266		OBS deployed
MSM69_15-1	Ocean bottom seismometer	2017-11-22T07:40:00	-1.17291	-5.26498	-5147	2017-12-03T22:36:00	-1.17347	-5.27026		OBS deployed
MSM69_16-1	Ocean bottom seismometer	2017-11-22T08:16:00	-1.19240	-5.35263	-5144	2017-12-04T00:57:00	-1.19282	-5.35932		OBS deployed
MSM69_17-1	Ocean bottom seismometer	2017-11-22T08:51:00	-1.21236	-5.44033	-5162	2017-12-04T03:16:00	-1.21245	-5.44658		OBS deployed
MSM69_18-1	Ocean bottom seismometer	2017-11-22T09:26:00	-1.23185	-5.52868	-5148	2017-12-04T05:28:00	-1.23087	-5.53503		OBS deployed
MSM69_19-1	Heat-Flow probe	2017-11-22T10:38:00	-1.26185	-5.66497	-5162	2017-11-22T23:54:00	-1.24382	-5.58575	-5087.1	in the water
MSM69_20-1	Ocean bottom seismometer	2017-11-23T00:29:00	-1.25235	-5.61577	-5175	2017-12-04T19:13:00	-1.25131	-5.62175		OBS deployed
MSM69_21-1	Ocean bottom seismometer	2017-11-23T01:09:00	-1.27196	-5.70315	-5159	2017-12-04T20:20:00	-1.27185	-5.70623		OBS deployed
MSM69_22-1	Ocean bottom seismometer	2017-11-23T01:45:00	-1.29169	-5.79084	-5081	2017-12-04T21:28:00	-1.29228	-5.79373		OBS deployed
MSM69_23-1	Ocean bottom seismometer	2017-11-23T02:19:00	-1.31186	-5.87855	-5120	2017-12-04T22:40:00	-1.31114	-5.88296		OBS deployed
MSM69_24-1	Ocean bottom	2017-11-23T02:52:00	-1.33211	-5.96682	-5287	2017-12-04T23:38:00	-1.33269	-5.96822		OBS deployed

	seismometer									
MSM69_25-1	Ocean bottom seismometer	2017-11-23T03:40:00	-1.36161	-6.09852	-4825	2017-12-05T01:09:00	-1.36200	-6.10515		OBS deployed
MSM69_26-1	Ocean bottom seismometer	2017-11-23T04:29:00	-1.39094	-6.23013	-5158	2017-12-05T02:30:00	-1.38784	-6.23990		OBS deployed
MSM69_27-1	Ocean bottom seismometer	2017-11-23T05:20:00	-1.42075	-6.36172	-4960	2017-12-05T03:30:00	-1.41933	-6.36913		OBS deployed
MSM69_28-1	Ocean bottom seismometer	2017-11-23T06:07:00	-1.45098	-6.49330	-5096	2017-12-05T05:37:00	-1.44833	-6.49899		OBS deployed
MSM69_29-1	Ocean bottom seismometer	2017-11-23T06:54:00	-1.48068	-6.62480	-4941	2017-12-05T07:42:00	-1.47865	-6.62966		OBS deployed
MSM69_30-1	Ocean bottom seismometer	2017-11-23T07:42:00	-1.51050	-6.75637	-4852	2017-12-05T09:18:00	-1.50521	-6.77299		OBS deployed
MSM69_31-1	Ocean bottom seismometer	2017-11-23T08:29:00	-1.53959	-6.88838	-4809	2017-12-05T11:23:00	-1.53789	-6.89069		OBS deployed
MSM69_32-1	Ocean bottom seismometer	2017-11-23T09:20:00	-1.56932	-7.01964	-4874	2017-12-05T13:35:00	-1.56727	-7.02324		OBS deployed
MSM69_33-1	Ocean bottom seismometer	2017-11-23T10:07:00	-1.59942	-7.15122	-4819	2017-12-05T15:49:00	-1.59647	-7.15625		OBS deployed
MSM69_34-1	Ocean bottom seismometer	2017-11-23T10:54:00	-1.62900	-7.28294	-4282	2017-12-05T17:58:00	-1.62678	-7.28820		OBS deployed
MSM69_35-1	Ocean bottom seismometer	2017-11-23T11:43:00	-1.65890	-7.41468	-4241	2017-12-05T18:48:00	-1.65703	-7.42014		OBS deployed
MSM69_36-1	Ocean bottom seismometer	2017-11-23T12:31:00	-1.68922	-7.54576	-4711	2017-12-05T20:02:00	-1.69036	-7.54945		OBS deployed
MSM69_37-1	Ocean bottom seismometer	2017-11-23T13:17:00	-1.71814	-7.67796	-4823	2017-12-05T21:08:00	-1.71401	-7.67669		OBS deployed
MSM69_38-1	Ocean bottom seismometer	2017-11-23T14:03:00	-1.74801	-7.80949	-4665	2017-12-06T12:57:00	-1.74755	-7.81128		OBS deployed
MSM69_39-1	Ocean bottom seismometer	2017-11-23T14:50:00	-1.77738	-7.94112	-4404	2017-12-06T13:52:00	-1.77766	-7.94854		OBS deployed
MSM69_40-1	Ocean bottom seismometer	2017-11-23T15:37:00	-1.80709	-8.07275	-4276	2017-12-06T16:08:00	-1.80534	-8.07771		OBS deployed
MSM69_41-1	Ocean bottom seismometer	2017-11-23T16:25:00	-1.83676	-8.20435	-4162	2017-12-06T17:15:00	-1.84512	-8.20851		OBS deployed
MSM69_42-1	Heat-Flow probe	2017-11-23T17:34:00	-1.87177	-8.37636	-4482	2017-11-23T20:22:00	-1.87167	-8.37614		in the water
MSM69_42-2	Heat-Flow probe	2017-11-23T20:57:00	-1.86971	-8.36735	-1000	2017-11-24T08:29:00	-1.85385	-8.29699	-4290.9	in the water
MSM69_43-1	Ocean bottom seismometer	2017-11-24T08:56:00	-1.86664	-8.33663	-4330	2017-12-06T18:21:00	-1.86676	-8.34191		OBS deployed
MSM69_44-1	Ocean bottom seismometer	2017-11-24T09:50:00	-1.89613	-8.46812	-4309	2017-12-06T20:13:00	-1.89728	-8.47153		OBS deployed
MSM69_45-1	Ocean bottom seismometer	2017-11-24T10:43:00	-1.92580	-8.59963	-4201	2017-12-06T22:17:00	-1.92824	-8.60192		OBS deployed
MSM69_46-1	Ocean bottom seismometer	2017-11-24T11:35:00	-1.95519	-8.73110	-4643	2017-12-07T00:22:00	-1.95746	-8.73029		OBS deployed
MSM69_47-1	Ocean bottom seismometer	2017-11-24T12:24:00	-1.98467	-8.86339	-4210	2017-12-07T02:36:00	-1.98851	-8.86466		OBS deployed
MSM69_48-1	Ocean bottom seismometer	2017-11-24T13:17:00	-2.01434	-8.99487	-4917	2017-12-07T04:40:00	-2.01492	-8.99693		OBS deployed
MSM69_49-1	Ocean bottom	2017-11-24T14:07:00	-2.04402	-9.12655	-3966	2017-12-07T06:33:00	-2.04365	-9.12943		OBS deployed

	seismometer									
MSM69_50-1	Ocean bottom seismometer	2017-11-24T14:53:00	-2.07400	-9.25794	-4067	2017-12-07T08:30:00	-2.07311	-9.26186		OBS deployed
MSM69_51-1	Ocean bottom seismometer	2017-11-24T15:40:00	-2.10306	-9.38997	-3918	2017-12-07T09:32:00	-2.10308	-9.39411		OBS deployed
MSM69_52-1	Ocean bottom seismometer	2017-11-24T16:27:00	-2.13266	-9.52154	-3770	2017-12-07T10:36:00	-2.13248	-9.52494		OBS deployed
MSM69_53-1	Ocean bottom seismometer	2017-11-24T17:13:00	-2.16202	-9.65316	-3990	2017-12-07T11:29:00	-2.16093	-9.65544		OBS deployed
MSM69_54-1	Ocean bottom seismometer	2017-11-24T17:59:00	-2.19190	-9.78476	-4149	2017-12-07T12:44:00	-2.18946	-9.78922		OBS deployed
MSM69_55-1	Ocean bottom seismometer	2017-11-24T18:47:00	-2.22156	-9.91664	-3900	2017-12-07T13:36:00	-2.22027	-9.92090		OBS deployed
MSM69_56-1	Ocean bottom seismometer	2017-11-24T19:32:00	-2.25092	-10.04851	-3656	2017-12-08T04:31:00	-2.25005	-10.05143		OBS deployed
MSM69_57-1	Ocean bottom seismometer	2017-11-24T20:19:00	-2.28036	-10.18019	-4173	2017-12-08T05:32:00	-2.28579	-10.17323		OBS deployed
MSM69_58-1	Ocean bottom seismometer	2017-11-24T21:08:00	-2.30992	-10.31174	-3933	2017-12-08T06:38:00	-2.31182	-10.31772		OBS deployed
MSM69_59-1	Ocean bottom seismometer	2017-11-24T22:08:00	-2.34896	-10.48725	-3337	2017-12-08T08:41:00	-2.34847	-10.49135		OBS deployed
MSM69_60-1	Ocean bottom seismometer	2017-11-24T22:46:00	-2.36893	-10.57508	-3344	2017-12-08T09:46:00	-2.36884	-10.58080		OBS deployed
MSM69_61-1	Ocean bottom seismometer	2017-11-24T23:24:00	-2.38828	-10.66302	-3510	2017-12-08T10:56:00	-2.38846	-10.66803		OBS deployed
MSM69_62-1	Ocean bottom seismometer	2017-11-25T00:02:00	-2.40785	-10.75068	-3438	2017-12-08T12:09:00	-2.40784	-10.75316		OBS deployed
MSM69_63-1	Ocean bottom seismometer	2017-11-25T00:41:00	-2.42743	-10.83877	-3517	2017-12-08T13:34:00	-2.42854	-10.84245		OBS deployed
MSM69_64-1	Ocean bottom seismometer	2017-11-25T01:15:00	-2.44703	-10.92687	-3518	2017-12-08T14:36:00	-2.44309	-10.95509		OBS deployed
MSM69_65-1	Ocean bottom seismometer	2017-11-25T01:51:00	-2.46704	-11.01452	-3701	2017-12-08T16:05:00	-2.46733	-11.01793		OBS deployed
MSM69_66-1	Ocean bottom seismometer	2017-11-25T02:26:00	-2.48634	-11.10242	-3707	2017-12-08T16:50:00	-2.48917	-11.10659		OBS deployed
MSM69_67-1	Ocean bottom seismometer	2017-11-25T03:02:00	-2.50598	-11.19014	-3754	2017-12-08T17:33:00	-2.50674	-11.19359		OBS deployed
MSM69_68-1	Ocean bottom seismometer	2017-11-25T03:37:00	-2.52542	-11.27802	-3770	2017-12-08T18:29:00	-2.52709	-11.28565		OBS deployed
MSM69_69-1	Ocean bottom seismometer	2017-11-25T04:35:00	-2.56444	-11.45386	-3473	2017-12-08T19:47:00	-2.56371	-11.45641		OBS deployed
MSM69_70-1	Ocean bottom seismometer	2017-11-25T05:33:00	-2.60392	-11.62956	-3201	2017-12-08T21:15:00	-2.60303	-11.63353		OBS deployed
MSM69_71-1	Ocean bottom seismometer	2017-11-25T06:30:00	-2.64302	-11.80510	-2745	2017-12-09T11:36:00	-2.64121	-11.81005		OBS deployed
MSM69_72-1	Ocean bottom seismometer	2017-11-25T07:27:00	-2.68233	-11.98085	-2643	2017-12-09T13:03:00	-2.68158	-11.98475		OBS deployed
MSM69_73-1	Ocean bottom seismometer	2017-11-25T08:26:00	-2.72056	-12.15693	-4085	2017-12-09T14:51:00	-2.71970	-12.16014		OBS deployed
MSM69_74-1	Ocean bottom seismometer	2017-11-25T09:34:00	-2.75993	-12.33259	-2599	2017-12-09T16:13:00	-2.75919	-12.33573		OBS deployed

MSM69_75-1	Ocean bottom seismometer	2017-11-25T10:37:00	-2.79937	-12.50818	-2894	2017-12-09T18:03:00	-2.79803	-12.51238		OBS deployed
MSM69_76-1	Ocean bottom seismometer	2017-11-25T11:42:00	-2.83819	-12.68404	-3068	2017-12-09T19:54:00	-2.83723	-12.68834		OBS deployed
MSM69_77-1	Seismic	2017-11-25T12:58:00	-2.77187	-12.88729	-3132	2017-12-02T09:58:00	-0.71396	-3.15610	-5127.5	Airgun in water
MSM69_77-2	ParaSound	2017-11-25T15:28:00	-2.86409	-12.79668	-3364	2017-12-02T09:23:00	-0.69933	-3.17210	-5133.3	profile start
MSM69_77-3	Multibeam	2017-11-25T15:28:00	-2.86409	-12.79666	-3364	2017-12-02T09:24:00	-0.69932	-3.17194	-5133.3	profile start
MSM69_78-1	Heat-Flow probe	2017-12-02T18:26:00	-0.88607	-4.00329	-4958	2017-12-03T05:18:00	-0.87276	-3.94145		in the water
MSM69_79-1	Heat-Flow probe	2017-12-04T05:53:00	-1.24092	-5.57673	-5111	2017-12-04T18:26:00	-1.17590	-5.59222		in the water
MSM69_80-1	Heat-Flow probe	2017-12-05T21:33:00	-1.71670	-7.66953	-4822	2017-12-06T10:52:00	-1.69889	-7.58977	-4511.5	in the water
MSM69_81-1	Heat-Flow probe	2017-12-07T14:10:00	-2.23507	-9.97913	-3821	2017-12-08T02:58:00	-2.21542	-9.89021		in the water
MSM69_82-1	Heat-Flow probe	2017-12-08T22:00:00	-2.58934	-11.56353	-3215	2017-12-09T09:41:00	-2.57639	-11.50631	-3170.2	in the water
MSM69_83-1	Multibeam	2017-12-09T20:05:00	-2.85409	-12.68122	-3077	2017-12-12T22:21:00	1.59263	-17.76502	-5284.6	profile start
MSM69_84-1	ParaSound	2017-12-12T22:21:00	1.59192	-17.76470	-5285	2017-12-12T23:33:00	1.46462	-17.78776	-5030	profile start
MSM69_85-1	Heat-Flow probe	2017-12-13T00:14:00	1.48005	-17.78992	-5053	2017-12-13T11:33:00	1.54271	-17.79991	-5256.5	in the water
MSM69_86-1	Heat-Flow probe	2017-12-13T13:43:00	1.90083	-17.85761	-5255	2017-12-13T23:43:00	1.95453	-17.86571	-5292.6	in the water
MSM69_87-1	Ocean bottom seismometer	2017-12-14T02:31:00	1.99070	-17.44968	-5310	2017-12-15T12:34:00	1.99375	-17.45242		OBS deployed
MSM69_88-1	Ocean bottom seismometer	2017-12-14T03:25:00	1.97983	-17.58410	-5271	2017-12-15T14:02:00	1.99029	-17.58779		OBS deployed
MSM69_89-1	Ocean bottom seismometer	2017-12-14T03:54:00	1.97362	-17.65120	-5263	2017-12-15T15:00:00	1.98451	-17.65614		OBS deployed
MSM69_90-1	Ocean bottom seismometer	2017-12-14T04:25:00	1.96807	-17.71827	-5264	2017-12-15T16:06:00	1.97818	-17.72471		OBS deployed
MSM69_91-1	Ocean bottom seismometer	2017-12-14T04:55:00	1.96176	-17.78520	-5273	2017-12-15T17:27:00	1.97116	-17.78985		OBS deployed
MSM69_92-1	Ocean bottom seismometer	2017-12-14T05:25:00	1.95628	-17.85251	-5286	2017-12-15T19:01:00	1.96438	-17.85586		OBS deployed
MSM69_93-1	Ocean bottom seismometer	2017-12-14T05:56:00	1.95034	-17.91987	-5288	2017-12-15T20:28:00	1.95722	-17.92184		OBS deployed
MSM69_94-1	Ocean bottom seismometer	2017-12-14T06:27:00	1.94426	-17.98718	-5305	2017-12-15T22:14:00	1.95230	-17.98965		OBS deployed
MSM69_95-1	Ocean bottom seismometer	2017-12-14T06:58:00	1.93828	-18.05467	-5313	2017-12-15T23:48:00	1.94663	-18.05840		OBS deployed
MSM69_96-1	Ocean bottom seismometer	2017-12-14T07:27:00	1.93267	-18.12163	-5315	2017-12-16T01:12:00	1.93854	-18.12303		OBS deployed
MSM69_97-1	Ocean bottom seismometer	2017-12-14T07:56:00	1.92666	-18.18887	-5307	2017-12-16T02:26:00	1.93218	-18.19095		OBS deployed
MSM69_98-1	Ocean bottom seismometer	2017-12-14T08:33:00	1.92135	-18.25607	-5317	2017-12-16T03:35:00	1.92550	-18.25670		OBS deployed
MSM69_99-1	Ocean bottom seismometer	2017-12-14T09:08:00	1.91503	-18.32324	-5317	2017-12-16T04:46:00	1.91941	-18.32562		OBS deployed
MSM69_100-1	Ocean bottom seismometer	2017-12-14T10:03:00	1.90320	-18.45764	-5287	2017-12-16T06:12:00	1.90689	-18.45957		OBS deployed
MSM69_101-1	Seismic	2017-12-14T11:14:00	1.93689	-18.63148	-5241	2017-12-15T10:58:00	1.98236	-17.29323	-5233.5	Airgun in water

MSM69_102-1	Multibeam	2017-12-14T12:14:00	1.89445	-18.59381	-5315	2017-12-15T10:10:00	2.00279	-17.31620	-5251.8	profile start
MSM69_103-1	ParaSound	2017-12-14T12:14:00	1.89445	-18.59381	-5315	2017-12-15T10:10:00	2.00280	-17.31592	-5254.7	profile start
MSM69_104-1	Multibeam	2017-12-16T06:25:00	1.88181	-18.47069	-5268	2017-12-16T16:13:00	2.08419	-17.88671	-5025.4	profile start
MSM69_105-1	ParaSound	2017-12-16T14:59:00	1.87729	-17.85895	-5212	2017-12-16T16:13:00	2.08419	-17.88671	-5025.4	profile start

Tab. 6.1: Deployment of Ocean-Bottom-Seismometers (OBS) and Hydrophones (OBH)

Station	Position						Depth	Time drift of data loggers								
P01																
obh01	00°	45,2933'	S	003°	25,4118'	W	5148	2017	325	08	24	336	13	38	70	GEOMAR
obs02	00°	47,6715'	S	003°	35,8775'	W	5141	2017	325	08	10	336	15	20	0	GEOMAR
obs03	00°	50,0567'	S	003°	46,3762'	W	5150	2017	325	10	41	336	16	57	84	GEOMAR
obs04	00°	52,4373'	S	003°	56,8570'	W	5145	2017	325	20	45	336	19	28	0	GEOMAR
obh05	00°	54,8320'	S	004°	07,4030'	W	5158	2017	325	21	24	337	08	21	87	GEOMAR
obs06	00°	57,2300'	S	004°	17,9663'	W	5012	2017	325	21	04	337	10	18	2	GEOMAR
obs07	00°	59,6307'	S	004°	28,5432'	W	5159	2017	326	02	43	337	12	20	0	GEOMAR
obs08	01°	02,0538'	S	004°	39,2205'	W	5165	2017	325	21	39	337	14	24	-119	GEOMAR
obs09	01°	04,4210'	S	004°	49,6560'	W	5144	2017	325	14	34	337	16	47	21	Ifremer
obs10	01°	06,8098'	S	005°	00,1923'	W	5163	2017	325	14	57	337	19	05	-216	Ifremer
obs11	01°	09,1868'	S	005°	10,6763'	W	5127	2017	325	15	18	337	21	31	-55	Ifremer
obs12	01°	10,3737'	S	005°	15,9123'	W	5150	2017	325	15	38	337	23	43	-267	Ifremer
obs13	01°	11,5545'	S	005°	21,1230'	W	5156	2017	325	15	59	338	02	02	-4154	Ifremer
obs14	01°	12,7448'	S	005°	26,3758'	W	5172	2017	325	16	15	338	04	23	-74	Ifremer
obs15	01°	13,9348'	S	005°	31,6275'	W	5160	2017	325	16	30	338	06	41	-84	Ifremer
obh16	01°	15,1238'	S	005°	36,8765'	W	5179	2017	326	19	20	338	20	34	-2	GEOMAR
obs17	01°	16,2942'	S	005°	42,0422'	W	5170	2017	326	21	03	338	21	27	304	GEOMAR
obs18	01°	17,4967'	S	005°	47,3528'	W	5081	2017	326	22	07	338	22	39	-139	GEOMAR
obs19	01°	18,6945'	S	005°	52,6455'	W	5128	2017	326	19	44	338	22	14	59	GEOMAR
obh20	01°	19,9037'	S	005°	57,9870'	W	5250	2017	327	02	19	339	00	48	-189	GEOMAR
obs21	01°	21,6937'	S	006°	05,8943'	W	4823	2017	327	03	27	339	02	16	-1310	GEOMAR
obs22	01°	23,4883'	S	006°	13,8265'	W	5146	2017	326	20	04	339	03	41	0	GEOMAR
obs23	01°	25,2900'	S	006°	21,7902'	W	4964	2017	327	02	42	339	14	24	0	GEOMAR
obs24	01°	27,0650'	S	006°	29,6417'	W	5094	2017	326	16	00	339	06	45	1	Ifremer
obs25	01°	28,8483'	S	006°	37,5275'	W	4959	2017	326	16	14	339	08	49	5	Ifremer
obs26	01°	30,6222'	S	006°	45,3788'	W	4846	2017	326	16	27	339	10	25	81	Ifremer
obs27	01°	32,4052'	S	006°	53,2698'	W	4789	2017	326	16	41	339	12	29	28	Ifremer
obs28	01°	34,1822'	S	007°	01,1355'	W	4850	2017	326	16	53	339	14	40	-71	Ifremer
obs29	01°	35,9603'	S	007°	09,0112'	W	4824	2017	326	17	06	339	16	53	-169	Ifremer
obs30	01°	37,7458'	S	007°	16,9215'	W	4300	2017	326	17	21	339	19	02	-218	Ifremer
obh31	01°	39,5295'	S	007°	24,8262'	W	4256	2017	327	04	02	339	19	57	274	GEOMAR
obs32	01°	41,3040'	S	007°	32,6898'	W	4717	2017	327	04	32	339	21	19	0	GEOMAR
obs33	01°	42,9970'	S	007°	40,1968'	W	4820	2017	327	04	56	339	22	25	-16	GEOMAR
obs34	01°	44,8173'	S	007°	48,2693'	W	4627	2017	327	12	40	340	14	05	29	GEOMAR
obh35	01°	46,6612'	S	007°	56,4525'	W	4210	2017	327	05	10	340	15	12	4	GEOMAR
obs36	01°	48.422‘	S	008°	04.368‘	W	4272							no	data	GEOMAR
obs37	01°	50,1865'	S	008°	12,1060'	W	4104	2017	327	15	07	340	18	29	41	GEOMAR
obs38	01°	52,0040'	S	008°	20,1788'	W	4339	2017	328	07	04	340	19	31	-6	GEOMAR
obs39	01°	53,7717'	S	008°	28,0337'	W	4309	2017	327	08	15	340	21	18	-332	Ifremer
obs40	01°	55,5350'	S	008°	35,8707'	W	4227	2017	327	09	09	340	23	25	-49	Ifremer
obs41	01°	57,3085'	S	008°	43,7588'	W	4653	2017	327	16	34	341	01	27	75	Ifremer
obs42	01°	59,0925'	S	008°	51,6945'	W	4170	2017	327	16	18	341	03	40	-46	Ifremer

obs43	02°	00,8665'	S	008°	59,5890'	W	4011	2017	327	16	48	341	05	46	164	Ifremer
obs44	02°	02,6422'	S	009°	07,4952'	W	3968	2017	327	17	01	341	07	36	-64	Ifremer
obs45	02°	04,4225'	S	009°	15,4243'	W	4077	2017	327	17	10	341	09	36	-36	Ifremer
obh46	02°	06,2035'	S	009°	23,3605'	W	3935	2017	328	10	21	341	10	47	-93	GEOMAR
obs47	02°	07,9713'	S	009°	31,2408'	W	3775	2017	328	10	34	341	11	47	261	GEOMAR
obh48	02°	09,7522'	S	009°	39,1833'	W	3992	2017	328	10	22	341	12	37	0	GEOMAR
obs49	02°	11,5160'	S	009°	47,0513'	W	4130	2017	328	10	53	341	13	54	0	GEOMAR
obs50	02°	13,3047'	S	009°	55,0365'	W	3905	2017	328	15	12	342	14	44	1	GEOMAR
obh51	02°	15,0727'	S	010°	02,9297'	W	3655	2017	328	15	29	342	05	50	-141	GEOMAR
obs52	02°	16,7118'	S	010°	10,2527'	W	4178	2017	328	15	42	342	06	46	-2	GEOMAR
obs53	02°	18,6248'	S	010°	18,8033'	W	3970	2017	328	15	51	342	07	46	107	GEOMAR
obs54	02°	20,9467'	S	010°	29,1882'	W	3353	2017	328	10	29	342	09	46	-73	Ifremer
obs55	02°	22,1303'	S	010°	34,4792'	W	3338	2017	328	11	04	342	10	53	53	Ifremer
obs56	02°	23,3007'	S	010°	39,7143'	W	3521	2017	328	11	17	342	12	00	-66	Ifremer
obs57	02°	24,4780'	S	010°	44,9875'	W	3445	2017	328	11	58	342	13	17	406	Ifremer
obs58	02°	25,6568'	S	010°	50,2637'	W	3509	2017	328	12	20	342	14	38	-70	Ifremer
obs59	02°	26,8318'	S	010°	55,5315'	W	3510	2017	328	13	38	342	15	44	40	Ifremer
obs60	02°	28,0100'	S	011°	00,8095'	W	3707	2017	328	13	51	342	17	08	-51	Ifremer
obs61	02°	29.185‘	S	011°	06.150‘	W	3706							no	data	GEOMAR
obh62	02°	30,3690'	S	011°	11,3827'	W	3758	2017	328	22	21	342	19	20	158	GEOMAR
obs63	02°	31,5460'	S	011°	16,6628'	W	3772	2017	328	20	10	342	19	43	-3	GEOMAR
obh64	02°	33,8987'	S	011°	27,2190'	W	3481	2017	328	21	35	342	21	06	608	GEOMAR
obh65	02°	36,2515'	S	011°	37,7835'	W	3209	2017	328	14	35	342	22	23	282	GEOMAR
obh66	02°	38,6028'	S	011°	48,3545'	W	2745	2017	328	21	19	343	13	00	1 ms	GEOMAR
obh67	02°	40,9518'	S	011°	58,9098'	W	2636	2017	328	22	26	343	14	14	2 ms	GEOMAR
obh68	02°	43,3010'	S	012°	09,4840'	W	4128	2017	328	21	57	343	16	03	-178	GEOMAR
obh69	02°	45,6422'	S	012°	20,0287'	W	2650	2017	328	22	26	343	14	14	2	GEOMAR
obs70	02°	47,9822'	S	012°	30,5760'	W	2924	2017	328	22	34	343	19	05	-100	Ifremer
obs71	02°	50,3227'	S	012°	41,1265'	W	3128	2017	328	22	51	343	21	09	82	Ifremer
P02																
obh72	01°	59,4650'	N	017°	26,9640'	W	5147	2017	347	20	01	349	13	48	9	GEOMAR
obs73	01°	58,7620'	N	017°	35,0280'	W	5141	2017	347	20	57	349	15	16	0	GEOMAR
obs74	01°	58,4090'	N	017°	39,0660'	W	5150	2017	347	21	03	349	16	09	-16	GEOMAR
obs75	01°	58,0570'	N	017°	43,0980'	W	5147	2017	347	21	24	349	17	19	-22	GEOMAR
obs76	01°	57,7050'	N	017°	47,1300'	W	5141	2017	347	19	51	349	18	39	-6	Ifremer
obs77	01°	57,3530'	N	017°	51,1680'	W	5150	2017	347	20	07	349	20	06	-11	Ifremer
obs78	01°	57,0000'	N	017°	55,2000'	W	5147	2017	347	20	17	349	21	32	4	Ifremer
obs79	01°	56,6470'	N	017°	59,2320'	W	5141	2017	347	20	30	349	23	19	54	Ifremer
obs81	01°	56,2940'	N	018°	03,2700'	W	5150	2017	347	20	41	350	00	51	-10	Ifremer
obs81	01°	55,9410'	N	018°	07,3020'	W	5147	2017	347	20	55	350	02	15	-4	Ifremer
obs82	01°	55,5880'	N	018°	11,3340'	W	5141	2017	347	21	16	350	02	00	0	GEOMAR
obs83	01°	55,2340'	N	018°	15,3720'	W	5150	2017	347	21	29	350	04	45	0	GEOMAR
obs84	01°	54,8810'	N	018°	19,4040'	W	5150	2017	347	21	42	350	05	56	0	GEOMAR
obh85	01°	54,1730'	N	018°	27,4680'	W	5147	2017	347	21	50	350	07	24	0	GEOMAR

Tab. 6.2: Seismic profiles

MSM69 – LITHOS-iLAB:
Airgun shooting

Profile	No. Shots	Latitude 1		Longitude 1		Latitude 2		Longitude 2	
P01	2777	2.865	S	12.800	W	0.700	S	3.175	W
P02	870	1.917	N	18.598	W	2.003	N	17.312	W

Tab. 6.3: Location of heat flow sites

Note: locations are ship's positions and not probe positions during the measurement at the seabed.

ID	Latitude		Longitude		Water Depth [m]	Date	Penetration Time (UTC)
	DD	MM.MMM	DDD	MM.MMM			
HF1760 - MSM69_6							
HF1760P01	-0	52.338	-3	56.417	5130	21.11.2017	14:16:50
HF1760P02	-0	52.22	-3	55.89	5134	21.11.2017	15:28:45
HF1760P03	-0	52.1	-3	55.36	5139	21.11.2017	16:34:00
HF1760P04	-0	51.984	-3	54.836	5138	21.11.2017	17:35:05
HF1760P05	-0	51.858	-3	54.306	5138	21.11.2017	18:52:10
HF1760P06	-0	51.737	-3	53.780	5139	21.11.2017	20:06:25
HF1760P07	-0	51.618	-3	53.254	5136	21.11.2017	21:18:35
HF1760P08	-0	51.5	-3	52.73	5138	21.11.2017	22:33:55
HF1761 - MSM69_19							
HF1761P01	-1	15.712	-5	39.898	5161	22.11.2017	13:04:50
HF1761P02	-1	15.592	-5	39.372	5162	22.11.2017	14:25:00
HF1761P03	-1	15.471	-5	38.845	5168	22.11.2017	15:33:44
HF1761P04	-1	15.351	-5	38.317	5166	22.11.2017	16:45:59
HF1761P05	-1	15.234	-5	37.787	5176	22.11.2017	17:46:40
HF1761P06	-1	15.108	-5	37.254	5173	22.11.2017	18:56:30
HF1761P07	-1	14.987	-5	36.727	5172	22.11.2017	20:01:50
HF1761P08	-1	14.868	-5	36.200	5168	22.11.2017	21:14:40
HF1761P09	-1	14.750	-5	35.672	5176	22.11.2017	22:19:20
HF1761P10	-1	14.629	-5	35.145	5165	22.11.2017	23:15:30
HF1762 - MSM69_42							
HF1762P01	-1	52.182	-8	22.041	4504	23.11.2017	23:14:20
HF1762P02	-1	52.064	-8	21.514	4498	24.11.2017	00:19:00
HF1762P03	-1	51.943	-8	20.886	4338	24.11.2017	01:33:00
HF1762P04	-1	51.829	-8	20.465	4329	24.11.2017	02:45:50
HF1762P05	-1	51.710	-8	19.937	4365	24.11.2017	04:02:10
HF1762P06	-1	51.590	-8	19.410	4395	24.11.2017	05:11:00
HF1762P07	-1	51.468	-8	18.874	4400	24.11.2017	06:14:40
HF1762P08	-1	51.350	-8	18.348	4390	24.11.2017	07:10:20
HF1762P09	-1	51.230	-8	17.819	4284	24.11.2017	08:01:50
HF1763 - MSM69_78							
HF1763P02	-0	53.050	-3	59.660	5115	02.12.2017	22:08:10
HF1763P03	-0	52.930	-3	59.130	5137	02.12.2017	23:11:20
HF1763P04	-0	52.818	-3	58.600	5138	03.12.2017	00:14:20
HF1763P05	-0	52.700	-3	58.070	5149	03.12.2017	01:26:50
HF1763P06	-0	52.586	-3	57.542	5133	03.12.2017	02:50:00
HF1763P07	-0	52.478	-3	57.017	5135	03.12.2017	04:00:20
HF1763P08	-0	52.363	-3	56.487	5130	03.12.2017	05:11:30

HF1764 - MSM69_79							
HF1764P01	-1	14.452	-5	34.593	5107	04.12.2017	08:15:20
HF1764P02	-1	13.895	-5	34.723	5161	04.12.2017	09:26:20
HF1764P03	-1	13.337	-5	34.855	5169	04.12.2017	11:03:50
HF1764P04	-1	12.781	-5	34.989	5171	04.12.2017	12:27:00
HF1764P05	-1	12.224	-5	35.125	5170	04.12.2017	13:44:50
HF1764P06	-1	11.669	-5	35.259	5171	04.12.2017	15:09:00
HF1764P07	-1	11.115	-5	35.403	5164	04.12.2017	16:16:20
HF1764P08	-1	10.559	-5	35.536	5163	04.12.2017	17:28:10
HF1765 - MSM69_80							
HF1765P01	-1	43.001	-7	40.172	4821	05.12.2017	23:51:20
HF1765P02	-1	42.878	-7	39.634	4796	06.12.2017	00:58:10
HF1765P03	-1	42.760	-7	39.105	4651	06.12.2017	02:10:10
HF1765P04	-1	42.648	-7	38.578	4635	06.12.2017	03:16:40
HF1765P05	-1	42.530	-7	38.047	4594	06.12.2017	04:22:00
HF1765P06	-1	42.413	-7	37.514	4550	06.12.2017	05:43:40
HF1765P07	-1	42.288	-7	36.979	4635	06.12.2017	06:53:10
HF1765P08	-1	42.169	-7	36.447	4656	06.12.2017	08:06:30
HF1765P09	-1	42.051	-7	35.917	4595	06.12.2017	09:23:20
HF1765P10	-1	41.932	-7	35.386	4512	06.12.2017	10:22:50
HF1766 - MSM69_81							
HF1766P01	-2	14.111	-9	58.680	3823	07.12.2017	16:15:35
HF1766P02	-2	13.991	-9	58.154	3826	07.12.2017	17:17:50
HF1766P03	-2	13.868	-9	57.620	3859	07.12.2017	18:23:45
HF1766P04	-2	13.750	-9	57.084	3871	07.12.2017	19:24:00
HF1766P05	-2	13.632	-9	56.567	3887	07.12.2017	20:34:50
HF1766P06	-2	13.514	-9	56.040	3890	07.12.2017	21:37:30
HF1766P07	-2	13.395	-9	55.513	3894	07.12.2017	22:43:15
HF1766P08	-2	13.276	-9	54.985	3896	07.12.2017	23:51:50
HF1766P09	-2	13.158	-9	54.459	3907	08.12.2017	00:49:10
HF1766P10	-2	13.043	-9	53.939	3901	08.12.2017	01:47:20
HF1766P11	-2	12.926	-9	53.412	3902	08.12.2017	02:49:00
HF1767 - MSM69_82							
HF1767P01	-2	35.360	-11	33.811	3215	08.12.2017	23:57:30
HF1767P02	-2	35.295	-11	33.541	3227	09.12.2017	00:37:20
HF1767P03	-2	35.241	-11	33.284	3229	09.12.2017	01:30:20
HF1767P04	-2	35.182	-11	33.021	3211	09.12.2017	02:09:40
HF1767P05	-2	35.123	-11	32.757	3242	09.12.2017	02:48:10
HF1767P06	-2	35.064	-11	32.494	3285	09.12.2017	03:37:30
HF1767P07	-2	35.003	-11	32.230	3391	09.12.2017	04:28:27
HF1767P08	-2	34.944	-11	31.966	3386	09.12.2017	05:13:55
HF1767P09	-2	34.882	-11	31.696	3378	09.12.2017	06:02:00
HF1767P10	-2	34.822	-11	31.431	3240	09.12.2017	06:34:25
HF1767P12	-2	34.702	-11	30.906	3112	09.12.2017	08:12:55
HF1767P13	-2	34.644	-11	30.641	3191	09.12.2017	08:56:40
HF1767P14	-2	34.584	-11	30.378	3200	09.12.2017	09:41:00

HF1768 - MSM69_85							
HF1768P01	1	28.803	-17	47.395	5043	13.12.2017	02:34:40
HF1768P02	1	29.339	-17	47.490	5069	13.12.2017	03:47:30
HF1768P03	1	29.876	-17	47.575	5100	13.12.2017	05:04:10
HF1768P04	1	30.415	-17	47.653	5123	13.12.2017	06:13:10
HF1768P05	1	30.954	-17	47.739	5164	13.12.2017	07:20:40
HF1768P06	1	31.491	-17	47.825	5160	13.12.2017	08:36:25
HF1768P07	1	32.028	-17	47.912	5201	13.12.2017	09:44:20
HF1768P08	1	32.564	-17	47.996	5256	13.12.2017	10:54:30
HF1769 - MSM69_86							
HF1769P01	1	54.049	-17	51.428	5263	13.12.2017	16:07:10
HF1769P02	1	54.587	-17	51.515	5267	13.12.2017	17:12:30
HF1769P03	1	55.123	-17	51.599	5280	13.12.2017	18:31:30
HF1769P04	1	55.660	-17	51.685	5278	13.12.2017	19:38:20
HF1769P05	1	56.197	-17	51.771	5281	13.12.2017	20:51:40
HF1769P06	1	56.734	-17	51.857	5291	13.12.2017	22:00:00
HF1769P07	1	57.272	-17	51.943	5292	13.12.2017	23:08:00
HF1770 - MSM69_106							
HF1770P01	1	57.805	-17	52.029	5299	16.12.2017	19:29:50
HF1770P02	1	58.343	-17	52.115	5288	16.12.2017	20:41:55
HF1770P03	1	58.880	-17	52.200	5294	16.12.2017	21:59:40
HF1770P04	1	59.417	-17	52.285	5292	16.12.2017	23:09:40
HF1770P05	1	59.954	-17	52.371	5268	17.12.2017	00:29:20
HF1770P06	2	0	-17	52.457	5179	17.12.2017	01:41:45
HF1770P07	2	1.028	-17	52.544	5122	17.12.2017	02:56:00
HF1770P08	2	1.565	-17	52.629	5077	17.12.2017	04:23:10
HF1770P09	2	2.104	-17	52.715	4952	17.12.2017	05:32:00
HF1770P10	2	2.642	-17	52.800	4963	17.12.2017	06:45:50
HF1770P11	2	3.177	-17	52.888	4980	17.12.2017	07:59:55
HF1771 - MSM69_108							
HF1771P01	2	24.123	-17	56.243	5044	17.12.2017	18:09:50
HF1771P02	2	24.659	-17	56.321	5033	17.12.2017	19:19:50
HF1771P03	2	25.196	-17	56.405	5012	17.12.2017	20:37:50

7 Data and Sample Storage and Availability

Seismic data will be available after 1st of July 2020 at the PANGAEA World Data Centre, Bremerhaven (http:// http://www.pangaea.de).

Bathymetric data recorded during the survey MSM69 are available at the Bathymetric Data Centre of the the Bundesamt für Seeschifffahrt und Hydrographie, Rostock (http://www.bsh.de/en/Marine_data/Hydrographic_surveys_and_wreck_search/Bathymetry).

Table 7.1: Data storage and availability

Type	Database	Available	Free Access	Contact
Bathymetry	www.bsh.de	Jan. 18	Jan. 16	bathymetrie@bsh.de
OBS data				
GEOMAR	PANGAEA	Oct. 19	Jul. 20	igrevemeyer@geomar.de
IPGP	PANGAEA	Oct. 19	Jul .20	singh@ipgp,fr
Heat Flow				
Univ. Bremen	PANGAEA	Oct. 19	Jul. 20	vill@uni-bremen.de

PANGAEA: World Data Centre, Bremerhaven (htwww.pangaea.de)

8 Acknowledgements

We acknowledge the excellent and professional sea-going operations of the MARIA S. MERIAN during MSM69, by Captain Björn Maas and his crew. Ship time has been funded by the Deutsche Forschungsgemeinschaft / German Science Foundation (DFG). In addition, German participants acknowledge funding from the DFG, supporting transportation, travelling and airgun operation. German OBSs were provided and funded by GEOMAR's OCEANS programme and French OBS and participation of French Partners by an ERC advanced grant to Satish Singh.

9 References

Alt, J.C., J. Honnorez, C. Laverne, and R. Emmermann, 1986. Hydrothermal alteration of a 1 km section through the upper oceanic crust, Deep Sea Drilling Project Hole 504B: Mineralogy, chemistry, and evolution of seawater-basalt interactions. J. Geophys. Res. 91: 10309-10335.

Barrell, J., 1914. The strength of the Earth's crust. Journal of Geology, 22, 425–433.

Carlson, R.L., 1998. Seismic velocities in the uppermost oceanic crust: Age dependence and the fate of layer 2A. J. Geophys. Res., 103: 7069-7077.

Christeson, G.L., G.M. Purdy, and G.J. Fryer, 1994. Seismic constraints on shallow crustal emplacement processes at the fast spreading East Pacific Rise. J. Geophys. Res., 99: 17957-17973.

Davis, E.E., and H. Villinger, 1992. Tectonic and thermal structure of the middle valley sedimented rift, northern Juan de Fuca Ridge. Proc. Ocean Drill. Program Initial Rep., 139, 9-41.

Dunn, R.A., and Toomey, D.R., 1997. Seismological evidence for three-dimensional melt migration beneath the East Pacific Rise, Nature, 388, 259-262.

Eaton, D.W., Darbyshire, F., Evans, R.L., Grutter, H., Jones, A.G., Yuan, X., 2009. The elusive lithosphere-asthenosphere boundary (LAB) beneath cratons, Lithos 109, 1–22

Fisher, A.T., K. Becker, and T.N. Narasinham, 1994. Off-axis hydrothermal circulation: Parametric test of a refined model of processes at DSDP/ODP site 504. J. Geophys. Res., 99: 3097-3121.

Fisher, A. T. and Von Herzen, R. P. (2005) Models of hydrothermal circulation within 106 Ma seafloor: Constraints on the vigor of fluid circulation and crustal properties, below the Madeira Abyssal Plain. Geochemistry Geophysics Geosystems 6, Q11001.

Grevemeyer, I., and W. Weigel, 1996. Seismic velocities of the uppermost igneous crust versus age. Geophys. J. Int., 124: 631-635.

Grevemeyer, I., and W. Weigel, 1997. Increase of seismic velocities in upper oceanic crust: The "superfast" spreading East Pacific Rise at 14°14'S. Geophys. Res. Lett., 24: 217-220.

Grevemeyer, I. and A. Bartetzko, 2003. Hydrothermal ageing of oceanic crust: inferences from seismic studies and well logging, in Hydrogeology of Oceanic Lithosphere, eds. E.E. Davis and H. Elderfield, Cambridge University Press., pp 128-150.

Grevemeyer, I., W. Weigel, R.B. Whitmarsh, F. Avedik, and G.A. Dehghani, 1997. The Aegir Rift: crustal structure of an extinct spreading axis. Mar. Geophys. Res., 19: 1-23.

Grevemeyer, I., W. Weigel, and C. Jennrich, 1998. Structure and ageing of oceanic crust at 14°S on the East Pacific Rise, Geophys. J. Int., 135: 573-584.

Grevemeyer, I., N. Kaul, H. Villinger, and W. Weigel, 1999. Hydrothermal activity and the evolution of the seismic properties of upper oceanic crust, J. Geophys. Res., 104: 5069-5079.

Grevemeyer, I., E.R. Flueh, C. Reichert, J. Bialas, D. Kläschen, and C. Kopp, 2001a. Crustal architecture and deep structure of the Ninetyeast Ridge hotspot trail from active-source ocean bottom seismology, Geophys. J. Int., 144, 414-413.

Grevemeyer, I., W. Weigel, S. Schüssler, F. Avedik, 2001b. Crustal and upper mantle seismic structure and lithospheric flexure along the Society Island hotspot chain, Geophys. J. Int., 137, 123-140.

Grevemeyer, I., C.R. Ranero, and M. Ivandic, 2018, Structure of oceanic crust and serpentinization at subduction trenches, Geosphere, 14, doi:10.1130/GES01537.1.

Hartmann, A., and H. Villinger, 2002. Inversion of marine heat flow measurements by expansion of the temperature decay function. Geophys. J. Int., 148, 628–636.

Hasterok, D.,Chapman,D.,Davis,E.,2011.Oceanic heatflow: implications for global heat loss. Earth Planet. Sci. Lett., 311,386–395.

Hasterok, D., 2010. Thermal state of the oceanic and continental lithosphere, PhD. Thesis, University of Utha, 167pp.

Hasterok, D., 2013. A heat flow based cooling model for tectonic plates, Earth Planet. Sci. Lett., 361, 34-43.

Houtz, R., and J. Ewing, 1976. Upper crustal structure as a function of plate age. J. Geophys. Res., 81: 2490-2498.

Hutnak, M., A. T. Fisher, R. Harris, C. Stein, K. Wang, G. Spinelli, M. Schindler, H. Villinger, and E. Silver, 2008. Surprisingly large heat and fluid fluxes driven through midplate outcrops on ocean crust, Nat. Geosci., 1, 611–614, doi:10.1038/ngeo264.

Hyndman, R.D., and M.J. Drury, 1976. The physical properties of oceanic basement rocks from deep drilling on the Mid-Atlantic Ridge. J. Geophys. Res., 81, 4042-4060.

Hyndman, R.D., Davis, E.E., Wright, J., 1979, The measurements of marine geothermal heat flow by a multipenetration probe with digital acoustic telemetry and insitu thermal conductivity, Mar. Geophys. Res., 4, 181–205.

Kawakatsu, H., Kumar, P., Takei, Y., Shinohara, M., Kanazawa, T., et al., 2009. Seismic evidence for sharp lithosphere-asthenosphere boundaries of oceanic plates. Science 324:499–502

Korenaga, J., P. B. Kelemen, and W. S. Holbrook, 2002. Methods of resolving the origin of large igneous provinces from crustal seismology, J. Geophys. Res., 107, 2178, doi:10.1029/2001JB001030.

Langseth, M.G., P.J. Grim, and M. Ewing, 1965. Heat flow measurements in the East Pacific Ocean, J. Geophys. Res., 70: 367-380.

Lister, C.R.B., 1972. On the thermal balance of a mid-ocean ridge. Geophys. J. R. Astron. Soc., 26: 515-535.

Lister, C.R.B., 1979, The pulse-probe method of conductivity measurement, Geophys. J. R. Astr. Soc. 57, 451–461.

Lizarralde,D., Gaherty, J.B., Collins, J.A., Hirth, G., Kim, S.D., 2004. Spreading-rate dependence of melt extraction at mid-ocean ridges from mantle seismic refraction data, Nature, 432, 744-747.

Lizarralde, D., J.B. Gaherty, J.A. Collins, G. Hirth, R.L. Evans, 2012. Structure of Pacific-plate upper mantle from active-source seismic measurements of the NoMelt experiment, Fall Meeting of the American Geophysical Union, T33G-2732.

McKenzie, D. P., and M. J. Bickle, 1988. The volume and composition of melt generated by extension of the lithosphere, J. Petrol., 29, 625–679.

Mehouachi, F., and S.C. Singh, 2017, Water-rich sub-lithospheric melt channel in the equatorial Atlantic Ocean, Nature Geoscience, 11, doi:10.1038/s41561-017-0034-z.

Müller, R.D., Sdrolias, M., Gaina, C., and Roest, W. R., 2008. Age, spreading rates, and spreading asymmetry of the world's ocean crust, Geochem. Geophys. Geosyst., 9, Q04006, doi:10.1029/2007GC001743.

Muller, M.R., Robinson, C.J., Minshull, R.S., and Bickle, M.J., 1997. Thin crust beneath ocean drilling program borehole 735B at the Southwest Indian Ridge? Earth Planet. Sci. Lett., 148:93-108.

Naif, S., Key, K., Constable, S., Evans, R.L. 2013, Melt-rich channel observed at the lithospheric-asthenospheric boundary, Nature doi:10.1038/nature11939, 495, 356-359

Nettles, M., and Dziewonski, A.M., 2008. Radially anisotropic shear velocity structure of the upper mantle globally and beneath North America. J. Geophys. Res. 113, B02303

Nishimura, C.E., Forsyth, D.W., 1989. The anisotropic structure of the upper mantle in the Pacific. Geophys. J. Int., 96, 203–2

Osler,J.C., and K.E. Louden, 1995. The extinct spreading centre in the Labrador Sea: I - crustal structure from a 2-D seismic refraction velocity model. J. Geophys. Res., 100: 2261-2278.

Pavlenkova, N.I., 1996. General features of the uppermost mantle stratification from long-range seismic profiles, Tectonophysics, 264, 261-278.

Raitt, R.W., 1963. The crustal rocks, in The sea, Vol. 3, ed. M.N. Hill, Interscience, New York, 85-102.

Rychert, C.A., and Shearer, P.M., 2011. Imaging the lithosphere-asthenosphere boundary beneath the Pacific using SS waveform modeling, J. Geophys. Res., 116, B07307, doi:10.1029/2010JB008070

Sleep, N.H., and G.A. Barth, 1997. The nature of lower crust and shallow mantle emplaced at low spreading rates. Tectonophysics, 279: 181-191.

Smallwood, J.R., Staples, R.K., Richardson, K.R., and White, R.S., 1999. Crustal generation above the Iceland mantle plume: from continental rift to oceanic spreading center, J. geophys. Res., 104, 22885-22902.

Stein, C.A., and S. Stein, 1992. A model for the global variation in oceanic depth and heat flow with lithospheric age. Natur,e 359: 123-129.

Stein, C.A., and S. Stein, 1994. Constraints on hydrothermal heat flux trough the oceanic lithosphere from global heat flow. J. Geophys. Res., 99: 3081-3095.

Villinger, H., Davis, E.E., 1987, A new reduction algorithm for marine heat flow measurements, J. Geophys. Res., 92, 12846–12856.

Villinger, H., I. Grevemeyer, N. Kaul, J. Hauschild, and M. Pfender, 2002. Hydrothermal heat flux through aged oceanic crust: where does the heat escape?. Earth Planet. Sci. Lett., 202: 159-170.

Wang, T., J. Lin, B. Tucholke, and Y. J. Chen, 2011. Crustal thickness anomalies in the North Atlantic Ocean basin from gravity analysis, Geochem. Geophys. Geosyst., 12, Q0AE02, doi:10.1029/2010GC003402.

White, R.S., D. McKenzie, and R.K. O'Nions, 1992. Oceanic crustal thickness from seismic measurements and rare earth element inversion. J. Geophys. Res., 97: 19683-19715.

Whitmarsh, R.B., 1978. Seismic refraction studies of the upper igneous crust in the North Atlantic and porosity estimates for layer 2. Earth Plant. Sci. Lett., 37: 451-464.

Whitmarsh, R.B., et al., 1983. A lithospheric seismic refraction profile in the western North Atlantic, Geophys. J.R. astron. Soc., 75, 23-69

Appendix – Supplementary material heat flow sites

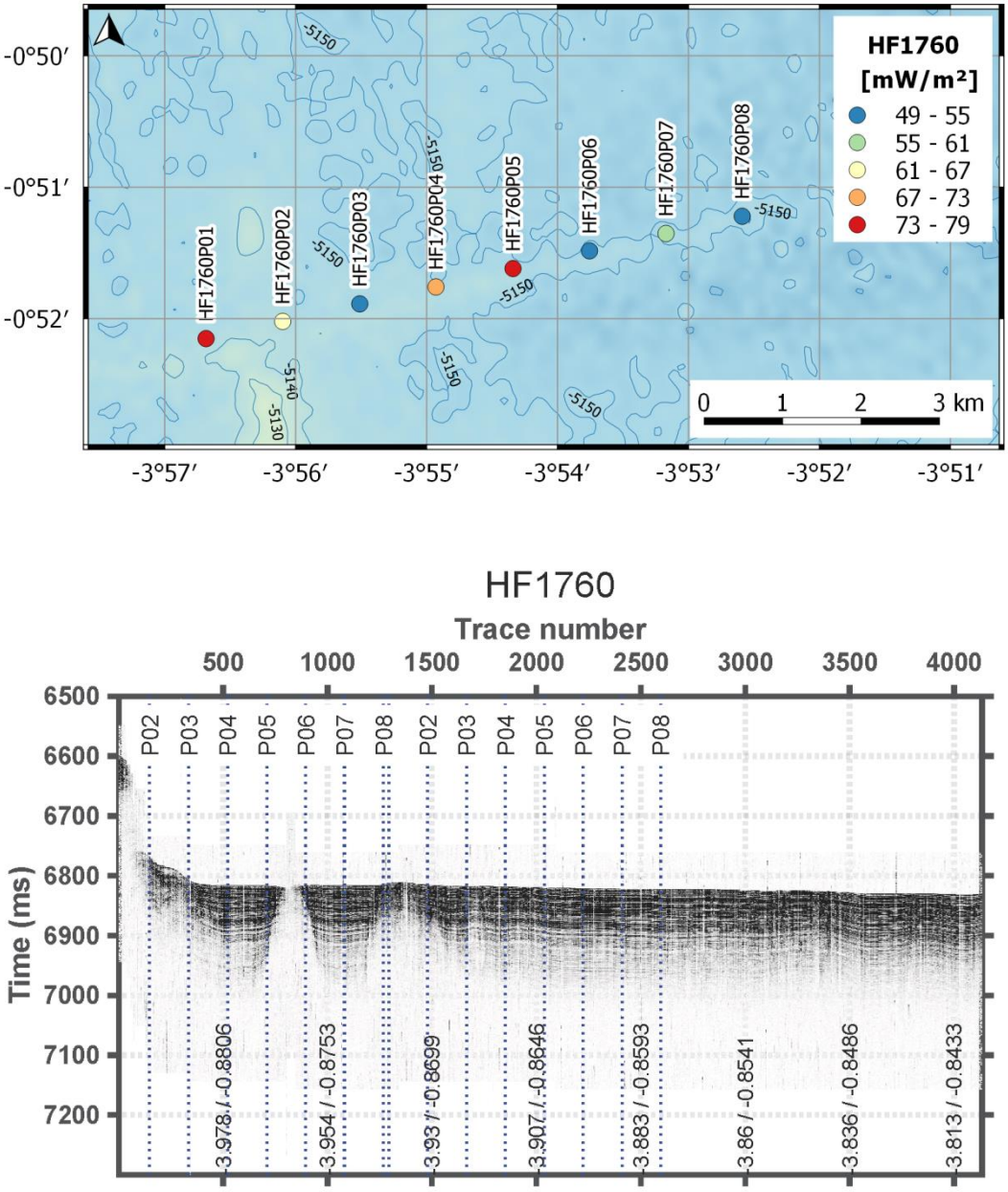

Fig. A1. Bathymetry and Parasound record of HF1760.

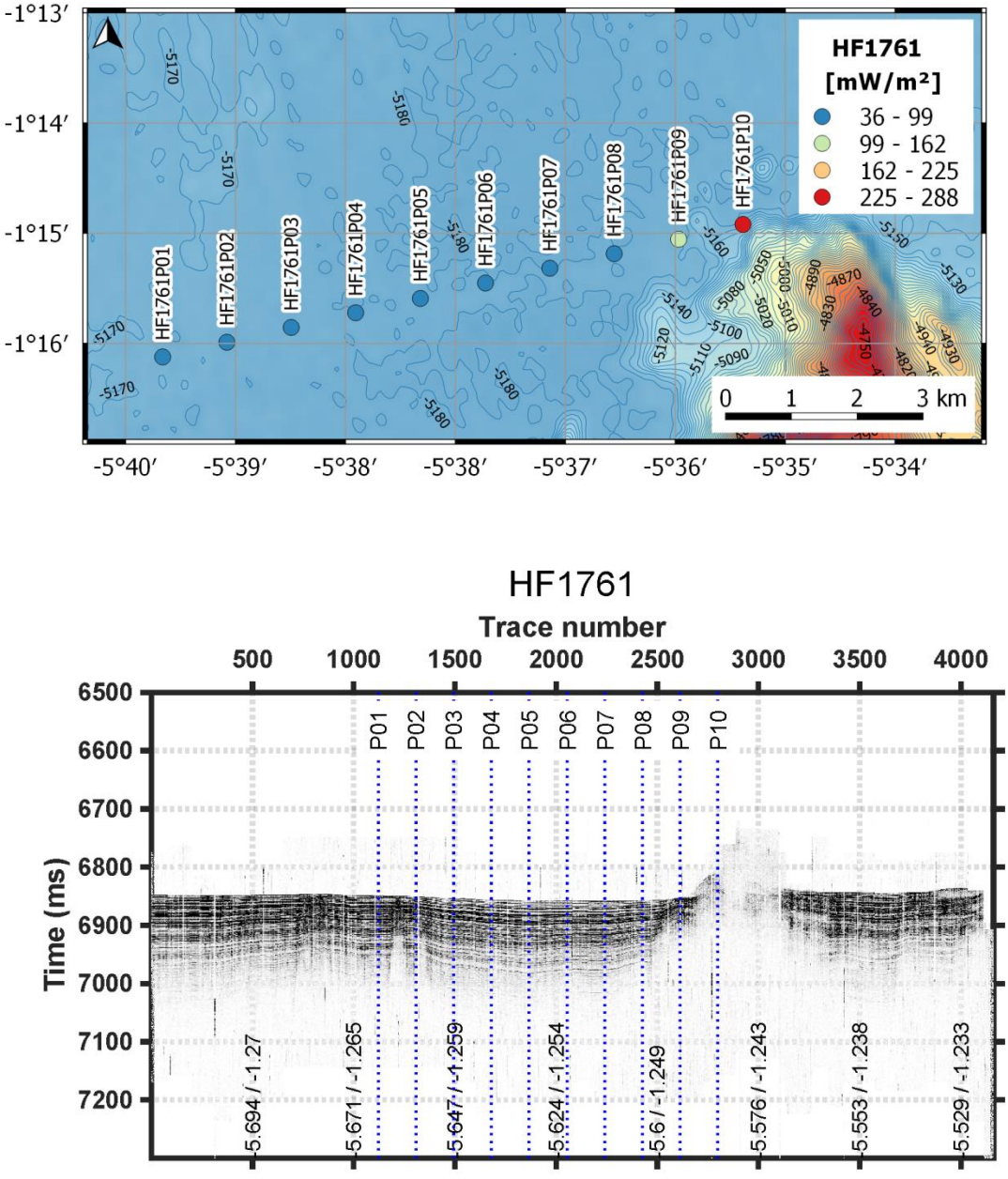

Fig. A2. Bathymetry and Parasound record of HF1761.

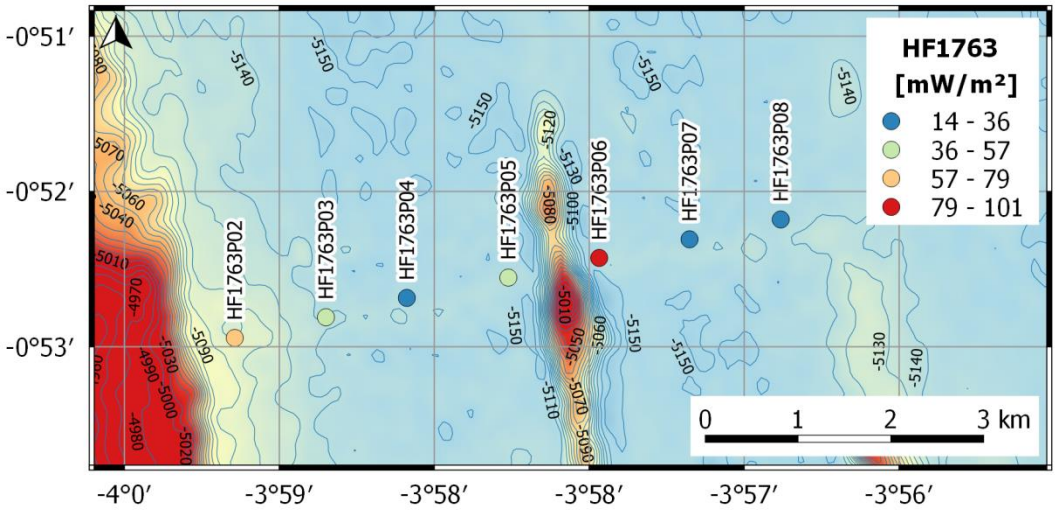

Fig. A3. Bathymetry record of HF1763.

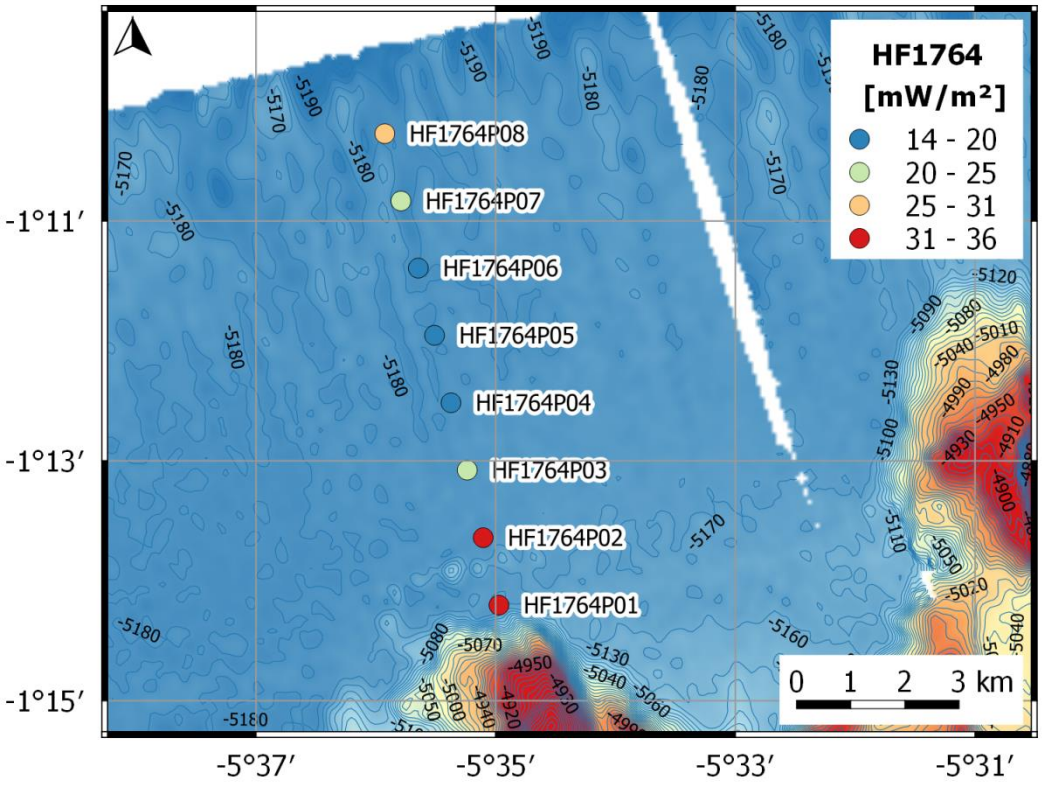

Fig. A4. Bathymetry record of HF1764. No Parasound .record is available for this profile.

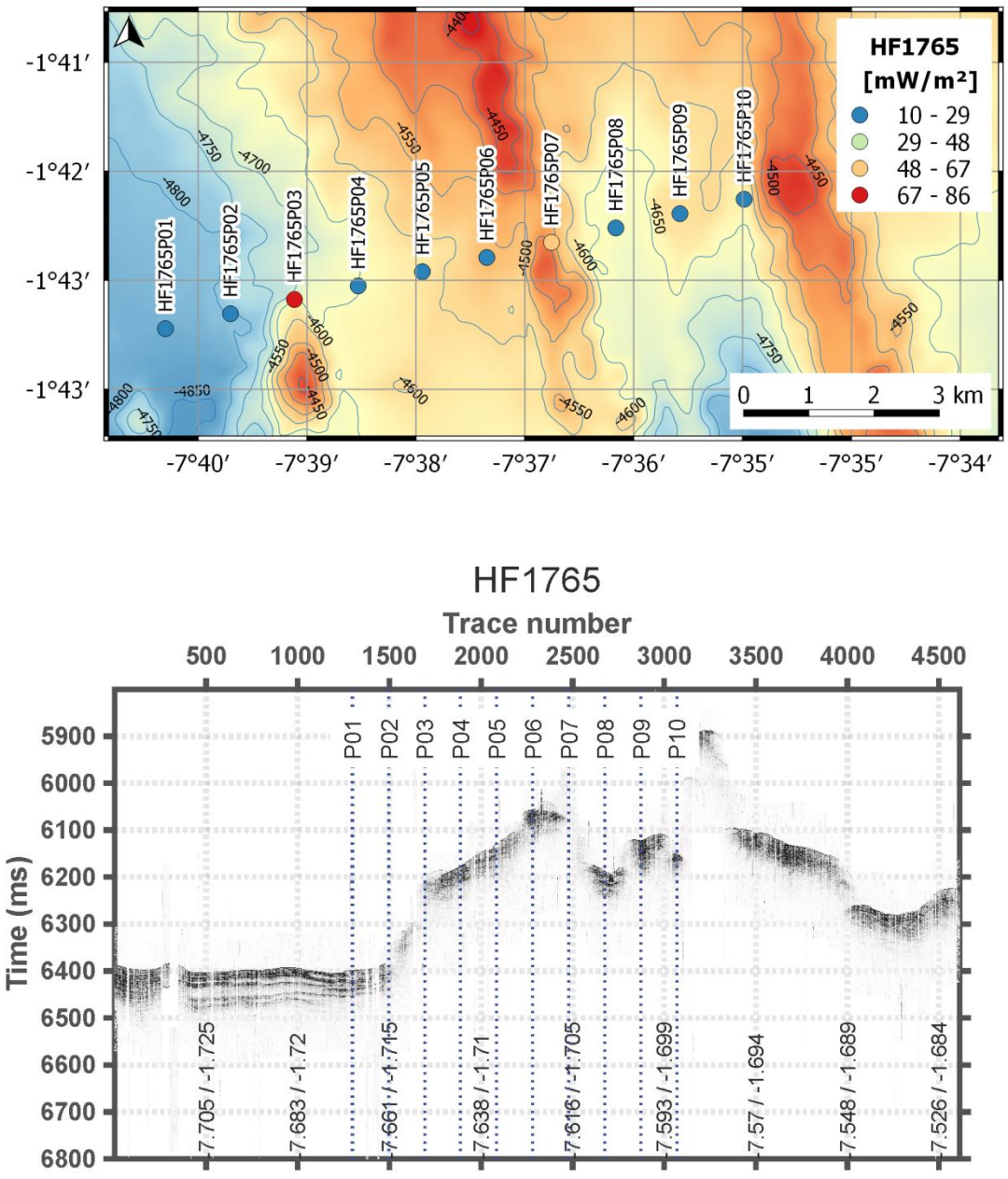

Fig. A5. Bathymetry and Parasound record of HF1765.

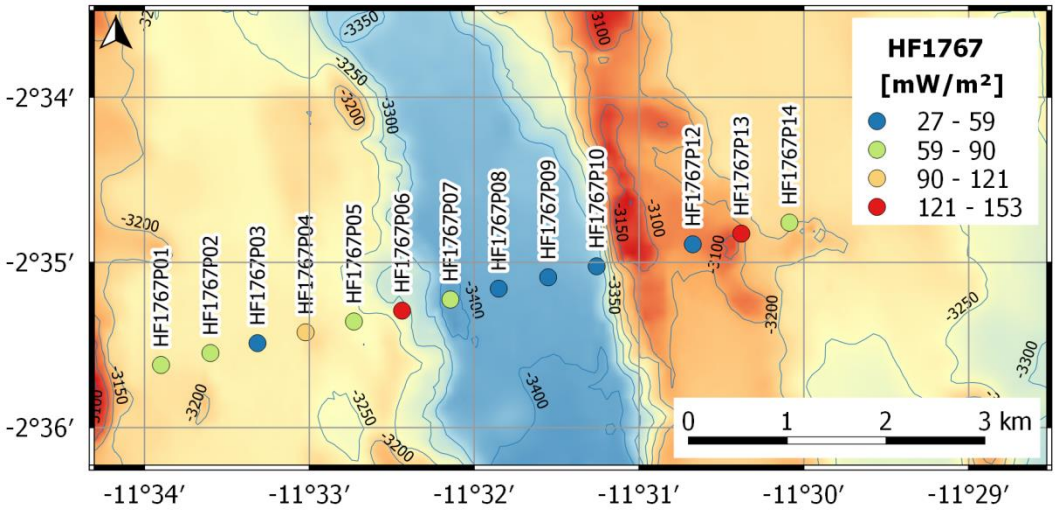

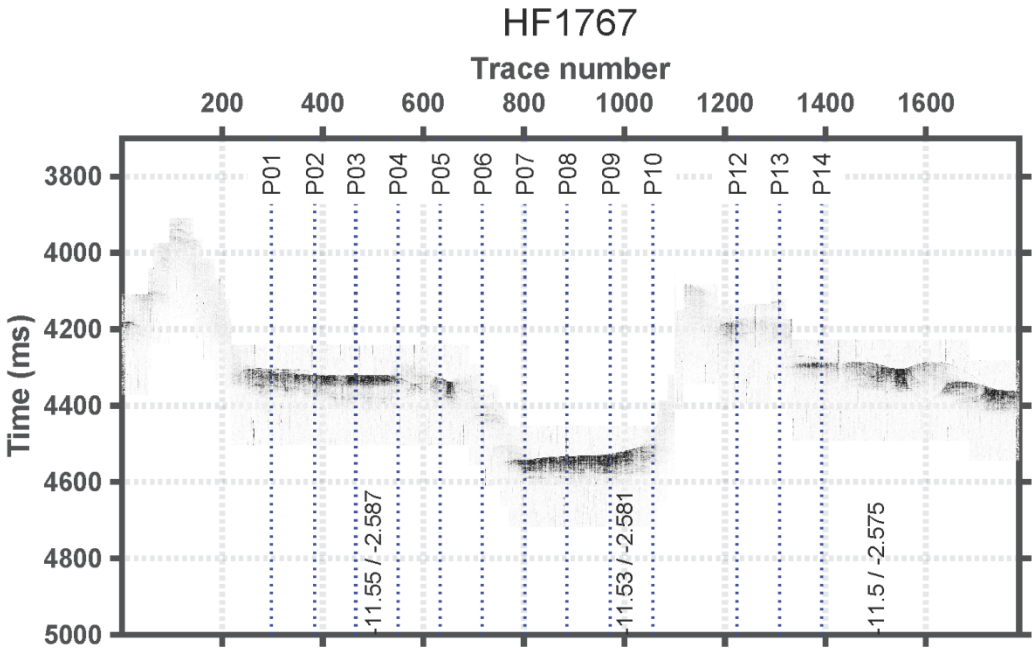

Fig. A7. Bathymetry and Parasound record of HF1767.

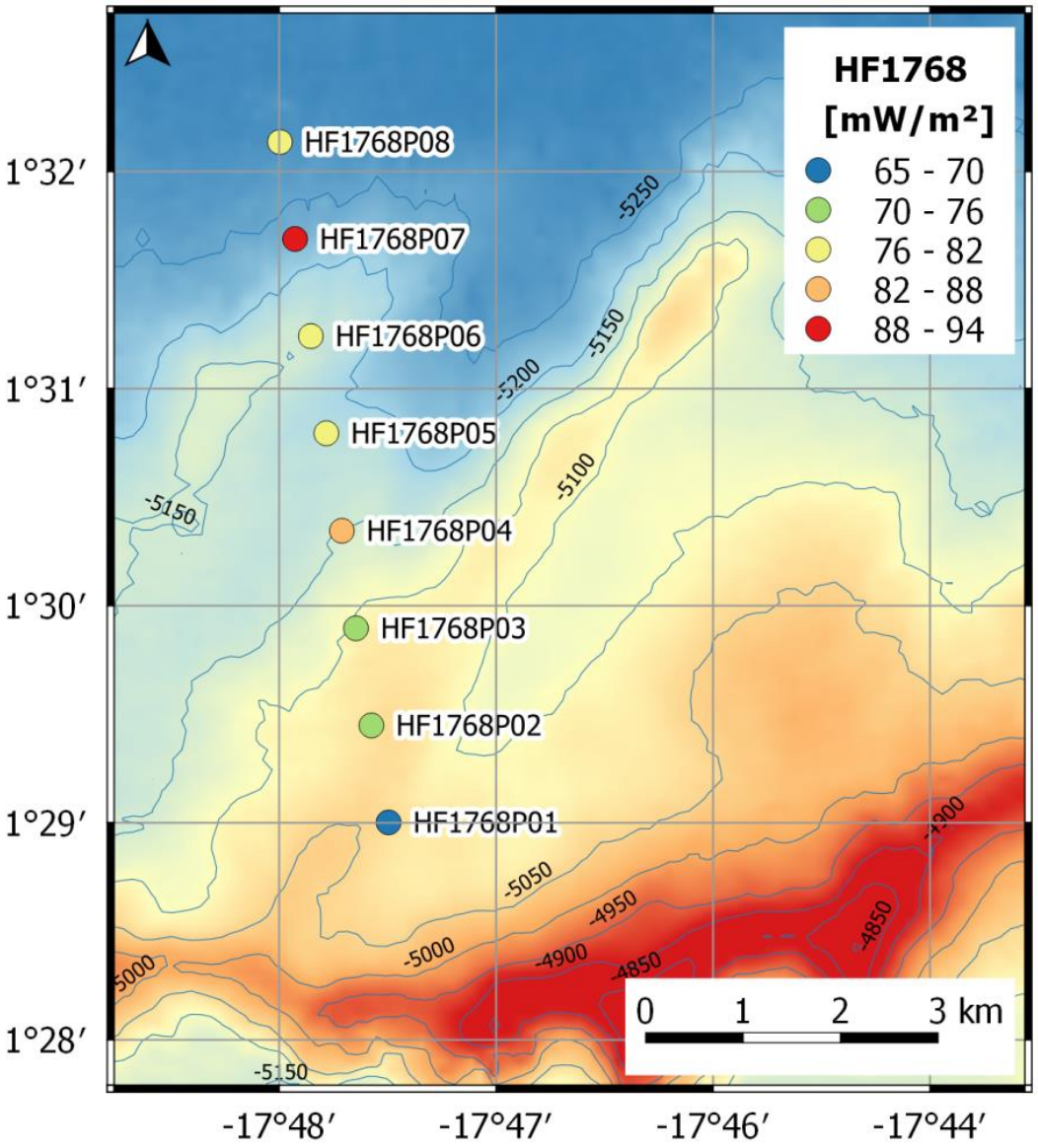

Fig. A8. Heat flow and bathymetry of HF1768.

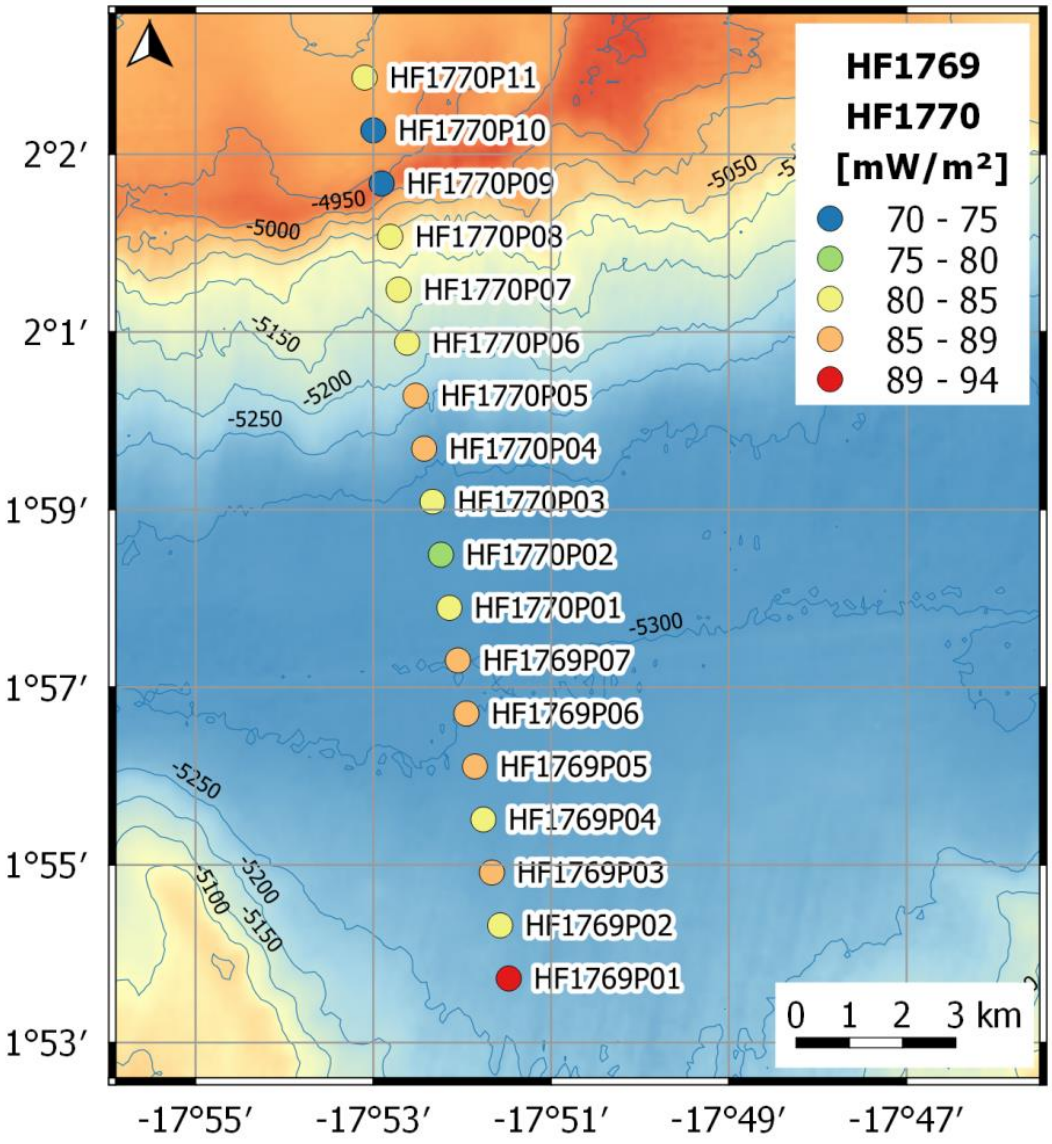

Fig. A9. Heat flow and bathymetry of HF1769 and HF1770.

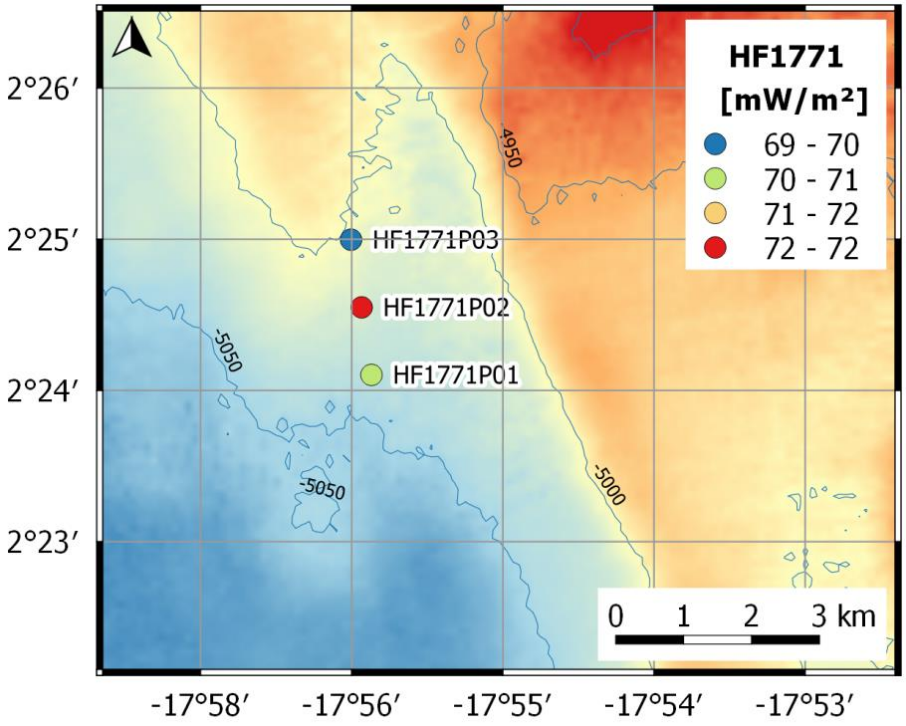

Fig A10. Heat flow and bathymetry of HF1771.

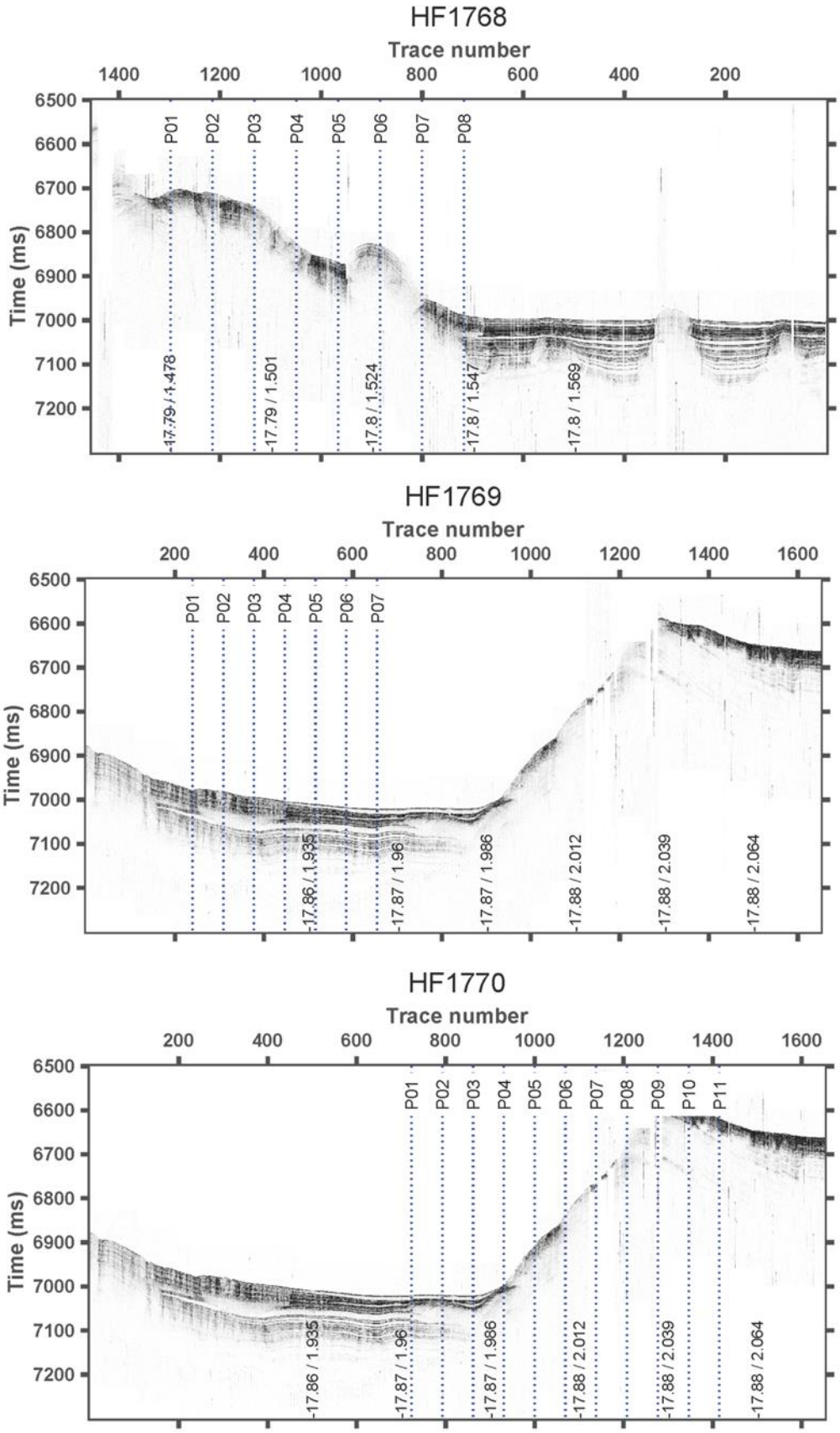

Fig A11. Parasound of HF 1768 to HF1771.